Review

Recent Advances in Layered MX$_2$-Based Materials (M = Mo, W and X = S, Se, Te) for Emerging Optoelectronic and Photo(electro)catalytic Applications

Felipe M. Pinto [1], Mary C. M. D. de Conti [2,3], Wyllamanney S. Pereira [4], Júlio C. Sczancoski [5], Marina Medina [6], Patricia G. Corradini [6,7], Juliana F. de Brito [6,8], André E. Nogueira [9], Márcio S. Góes [10], Odair P. Ferreira [2], Lucia H. Mascaro [6], Fernando Wypych [11,12] and Felipe A. La Porta [2,11,*]

[1] Department of Chemical and Materials Engineering, Federal University of Lavras, Lavras 37203-202, Brazil; felipe.moreira@ufla.br
[2] Post-Graduation Program in Chemistry, State University of Londrina, Rodovia Celso Garcia Cid, 445, Km 380, Londrina 86057-970, Brazil; mary@utfpr.edu.br (M.C.M.D.d.C.); opferreira@uel.br (O.P.F.)
[3] Nature Sciences Academic, Federal University of Technology–Paraná, Avenida Alberto Carazzai, 1640, Cornélio Procópio 86300-000, Brazil
[4] Department of Chemistry, State University of Ponta Grossa, Ponta Grossa 84010-330, Brazil; wyllamanneysp@gmail.com
[5] Department of Physics, State University of Ponta Grossa, Ponta Grossa 84010-330, Brazil; jcsfisica@gmail.com
[6] Department of Chemistry, Federal University of São Carlos, Rod. Washington Luiz, Km 235, São Carlos 13565-905, Brazil; marina.medina@unesp.br (M.M.); patcorradini@gmail.com (P.G.C.); juliana.f.brito@unesp.br (J.F.d.B.); lmascaro@pq.cnpq.br (L.H.M.)
[7] Laboratório de Análises Químicas e Agroambientais, Fluminense Federal Institute of Education, Science and Technology, Campus Itaperuna, BR 356, Km 3, Itaperuna 28300-000, Brazil
[8] Institute of Chemistry and Alternative Technologies of Detection, Toxicological Evaluation and Removal of Micropollutants and Radioactives (INCT-DATREM), São Paulo State University, Rua Francisco Degni, 55, Bairro Quitandinha, Araraquara 14800-900, Brazil
[9] Department of Chemistry, Division of Fundamental Sciences, Aeronautics Institute of Technology—ITA, São José dos Campos 12228-900, Brazil; andre.nogueira@ita.br
[10] Latin American Institute of Life and Nature Sciences, Department of Chemistry, Federal University of Latin American Integration, Av. Tancredo Neves, 6731–Bloco 6, Espaço 3, Sala 10, Foz do Iguaçu 85867-000, Brazil; marcio.goes@unila.edu.br
[11] Post-Graduation Program in Materials Science and Engineering, Federal University of Technology–Paraná, Londrina 86036-700, Brazil; wypych@ufpr.br
[12] Department of Chemistry, Federal University of Paraná, Curitiba 81531-980, Brazil
*   Correspondence: felipelaporta@utfpr.edu.br; Tel.: +55-(43)-3315-9437

Abstract: Transition metal dichalcogenides (TMDCs), represented by MX$_2$ (where M = Mo, W and X = S, Se, and Te), and more recently, their moiré superlattices (i.e., formed by superimposing layers of TMDCs with different rotation angles) have attracted considerable interest due to their excellent physical properties and unique nanoscale functionalities. Compared to graphene, the literature indicates that TMDCs offer a competitive advantage in optoelectronic technologies, primarily owing to their compositionally controlled non-zero bandgap. These two-dimensional (2D) nanostructured single or multiple layers exhibit remarkable properties that differ from their bulk counterparts. Moreover, stacking different TMDC monolayers also forms heterostructures and introduces unique quantum effects and extraordinary electronic properties, which is particularly promising for next-generation optoelectronic devices and photo(electro)catalytic applications. Therefore, in this review, we also highlight the new possibilities in the formation of 2D/2D heterostructures of MX$_2$-based materials with moiré patterns and discuss the main critical challenges related to the synthesis and large-scale applications of layered MX$_2$ and MX$_2$-based composites to spur significant advances in emerging optoelectronic and photo(electro)catalytic applications.

Keywords: 2D materials; MX$_2$; transition metals dichalcogenides; 2D/2D heterostructures

1. Introduction

Semiconductors and the devices leveraging them are indispensable components of modern technology, permeating our daily lives through applications in computing, communication, and beyond [1]. In the pursuit of enhanced functional properties for myriad high-performance applications, the synthesis of novel advanced semiconductors remains an ever-evolving endeavor [2,3]. A compelling avenue in this quest is the exploration of two-dimensional (2D) semiconductors, featuring structures with atomic or a few-atom thicknesses on the sub-nanometer scale [4,5]. This expansive family of materials encompasses mono-, bi-, and multi-elemental compositions [6].

Graphene, historically recognized as the first truly 2D atomic crystal, which was achieved via the groundbreaking feat of isolating single-layer carbon atoms in 2004 [7], covalently bonds through an sp^2 hybridization and one atom of thickness [8]. As we know, this peculiar structure gives graphene remarkable mechanical, optical, and electrical properties, setting it apart from other types of materials [8]. Despite the great interest in this system, it is well known that graphene nonetheless faces limitations as a zero-bandgap material (i.e., due to its massless electrons), hindering its direct applicability in semiconductor-dependent technologies, such as solar cells, light-emitting diodes, and others [7]. Efforts to address this shortfall have led to the exploration of graphene derivatives, including fluorinated graphene and graphane, though challenges persist in achieving high-quality crystals and stability [9].

Black phosphorus, or phosphorene, as the phosphorus monolayer is called, has emerged as another promising semiconductor due to its non-zero bandgap and ease of synthesis through the mechanical exfoliation of a single crystal, which facilitates its use in nanoelectronic applications [10]; however, challenges related to large-scale production hindered its industrial application [11].

All-inorganic 2D materials like silicene and germanene offer tantalizing prospects for the semiconductor industry, boasting high mobility akin to graphene [12] However, both materials are extremely difficult to synthesize, as simply exfoliating a silicon or germanium crystal to obtain a single layer is currently impossible. Furthermore, both materials are known to be prone to oxidation and volatilization post-synthesis [13]. Recently, several oxides have been produced in the form of 2D structures, including single layers of titanium oxide (TiO_2), molybdenum trioxide (MoO_3), tungsten trioxide (WO_3), and perovskite-like crystals [14]. Usually, these 2D oxide structures tend to be less vulnerable to environmental effects, are thermally stable, and exhibit lower dielectric constants and wider bandgaps than 3D crystals [15].

From this perspective, more recently, 2D-layered transition metals dichalcogenide (TMDC) materials have emerged as viable alternatives to two-elemental materials, with applications in the field of semiconductor nanodevices [16]. Moreover, it has been reported that the cytotoxicity of TMDCs is usually lower in relation to other graphene-based materials, such as graphene oxide and halogenated graphene [17]. TMDCs present layered structures in a buckled hexagonal lattice and have a general ideal formula of MX_2. TMDCs single layer are basically formed by three atomic sheets with transition metal tetravalent cations (M^{4+}) belonging to group IV, V, or VI in the periodic table (e.g., Mo, W, Sn, Ti, Re, Nb, Ta, Hf, Zr, and so on) sandwiched by two sheets of divalent chalcogenide anions (X^{2-}) such as S, Se, and Te [18]. The nature of the chemical bonds between the metal cations and the chalcogen anions (M-X) is mainly covalent [19], while the weaker intermolecular bonds between the triple sheets occur through van der Waals (vdW) bonds, i.e., making the X–X junction (Figure 1A) [20]. As we know, this unique structure allows for easy exfoliation into single- or few-layered flakes, offering tunable electronic properties and surface functionalities [21–23]. Additionally, TMDCs even with the same composition can be synthesized in different polymorphs and polytypes. Using MoS_2 as an example, a polymorph denoted as 1T [24], and two polytypes denoted as 2H and 3R are described in Figure 1A. The corresponding letter represents the commonly found trigonal, hexagonal, and rhombohedral crystalline lattices, respectively, while the numbers symbolize

the number of layers in the unit cell [19,25,26]. It is common for many 2D materials to have different polytypes simultaneously, for example, molybdenum disulfide (MoS_2) and tungsten disulfide (WS_2) can occur in both 1T and 2H polymorphs simultaneously [6]. On the other hand, the most researched TMDCs in the literature, including MoS_2 [27], $MoSe_2$ [28], WS_2 [29], and WSe_2 [30], demonstrate typical semiconductor behavior in their most stable 2H polytype.

A detailed understanding of the 2D-layered TMDC structures not only aids in their identification but also enables the characterization of different polymorphs and polytypes, thereby facilitating the tailoring of their properties to meet specific technological demands [31–35]. Zhao et al. [31] have reported a comprehensive review focusing on applying electron microscopy to identify polymorphs and stacking polytypes in both mono- and multilayer MoS_2 films. Thus, the experimental and simulated high-angle annular dark-field scanning transmission electron microscopy (HAADF-STEM) images for monolayer 1T, 1H, 1T′ and bilayer 2H, 3R, and trilayer 3R-stacked MoS_2 are described in Figure 1B.
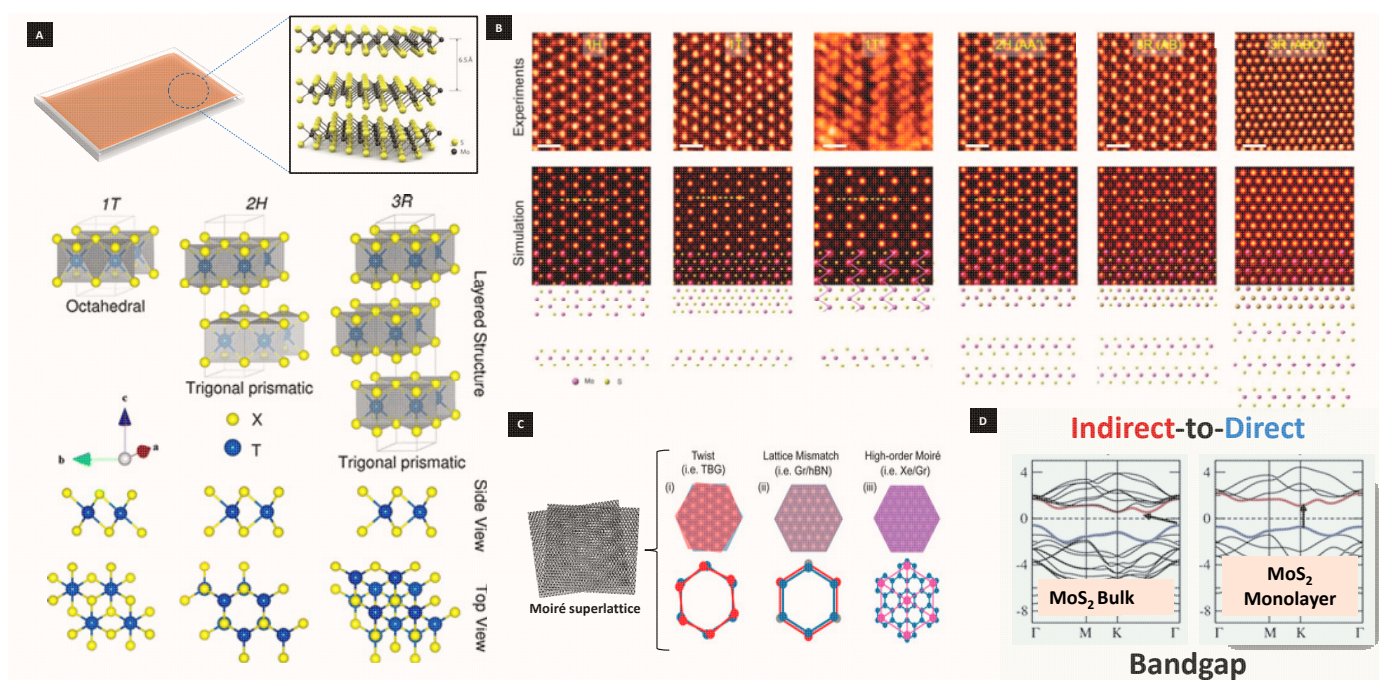
Figure 1. (**A**) Schematic illustration of 2D-layered MX_2 films showing interactions and bonds in stacked monolayers and their different 1T, 2H, and 3R polytypes. Reprinted with permission from Refs. [25,36]. Copyright 2015 The Royal Society of Chemistry (**B**) Atomic-resolution HAADF-STEM images and corresponding simulation results for monolayer 1T, 1H, 1T′ and bilayer 2H, 3R, and trilayer 3R-stacked MoS_2 [31–35]. Reprinted with permission from Ref. [31] Copyright 2018 Wiley. (**C**) Different types of moiré superlattices that emerge from superimposing two or more monolayers of TMDCs with varying angles of rotation: (i) twisted bilayers, (ii) bilayers exhibiting slight lattice mismatch, and (iii) high-order moiré superlattices characterized by small supercell lattice mismatch. Adapted with permission from Ref. [37] Copyright 2023 Wiley. (**D**) Electronic band structure for bulk and monolayer 2H-MoS_2 reveals tunable indirect-to-direct bandgap transition. Reprinted with permission from Ref. [38]. Copyright 2010 American Chemical Society.

Layered material structures can exhibit a wide range of electronic properties, including those of metals [39], semimetals [40], semiconductors [36,41,42], and superconductors [43], depending on the elements involved and the oxidation state of the transition metal. The electronic behavior of TMDCs is influenced by the filling of the *d*-band orbitals, with semiconducting properties emerging when these orbitals are partially occupied and metallic properties when fully filled [26]. However, it is noteworthy that the chalcogen anion exerts less influence compared to the metal cation. This phenomenon can be observed

in the enlargement of the *d*-band, resulting in a reduction of the bandgap, particularly with increasing the atomic number of chalcogen [26,39]. Apart from their semiconductor properties, these materials possess the capability to modulate their bandgap in relation to the thickness of the synthesized particles (i.e., number of packed layers), as illustrated in Figure 1D. As we know, it is possible to change from an indirect bandgap (at about 1.29 eV) in 2H-MoS$_2$ bulk form to a direct bandgap (at about 1.8 eV) in 2D form [26,36,39,44,45].

Recent advancements in the computational modelling of TMDCs have significantly advanced our understanding of their structural, electronic, and optical properties, paving the way for the design of novel materials and devices with tailored functionalities [46]. Particularly, electronic structure calculations have elucidated this indirect-to-direct bandgap of 2H-MoS$_2$ as a function of its number of packed layers, aligning closely with the experimental data [38], as shown in Figure 1D, and making them suitable for optoelectronic devices. As the number of layers diminishes, the indirect transition energy in single-layer 2H-MoS$_2$ rises to such an extent that it transforms into a direct bandgap 2D semiconductor. The unique electronic structure of few-layer 2H-MoS$_2$, as well as its resulting optical properties, arise from *d*-electron orbitals comprising its conduction and valence bands (CB and VB). In particular, the CB states at the *K* point predominantly consist of strongly localized *d* orbitals at Mo^{4+} sites. Conversely, the states found near the Γ point and the point of indirect bandgap arise from a linear combination of *d* orbitals on Mo cations and antibonding p_z orbitals on sulfur anions [38]. These states exhibit strong interlayer coupling, with their energies being highly responsive to changes in layer thickness. Moreover, bonding phenomena in MX$_2$ compounds have traditionally been viewed as a simple notion, leading solid-state chemists to apply these concepts even in cases where substantial covalency exists [17,47]. Hence, the challenge lies in finding a derivation that can explain both the structure and properties of these multifunctional materials in a comprehensive and applicable way. Orbital bands and multiple bonds are crucial factors that determine the properties of matter [48]. Their construction condition is an example of group multiplicities that form the basis of periodic matter investigation. This investigation encompasses the periodic properties, including the structural, optical, vibrational, electronic, electric, magnetic, and energetic configurations of nanostructures [49,50]. Researchers are continuously refining computational methods to account for the complex interplay of electronic interactions, spin–orbit coupling, and lattice dynamics in TMDCs, allowing for more reliable predictions of their behavior under different conditions [51–53]. Moreover, machine learning approaches are increasingly being integrated into computational modeling workflows to accelerate materials discovery and design. By training models on large datasets of experimentally measured TMDC properties, researchers can efficiently screen for promising candidates with desired characteristics, such as specific bandgaps, electronic transport properties, or optical responses [54–60]. By combining theoretical insights with experimental validation, computational studies are accelerating the discovery and development of TMDC-based materials and devices with tailored properties for a wide range of applications.

Band alignment is a fundamental concept in semiconductor physics that describes the alignment of energy bands at the interface between different semiconductor materials or between a semiconductor and another material, such as a metal or an insulator [61]. As we know, the CB minimum and VB maximum energies of MX$_2$ increase with the increasing atomic radius of X anions (from S to Te) [62]. Notably, the VB shift is more significant than the CB shift. Interestingly, semiconductor–metal (2D/2D) junctions exhibit weak Fermi level pinning, which suppresses metal-induced vacancy states [63]. This allows Schottky barriers to be attached to semiconductor-to-metal junctions and enables the barrier to be fully terminated with a suitable 2D metal. As we know, the emergence of moiré superlattices formed by 2D/2D TMDC materials represents a captivating frontier in nanotechnology. These superlattices arise from the stacking of two or more TMDC layers with a slight lattice mismatch or rotational misalignment, leading to the creation of periodic modulations in electronic and optical properties on a nanoscale [64–68]. Hence, depending on the stacking arrangements of two or more layers of transition metal dichalcogenides (TMDCs), the

moiré superlattice is usually classified into three distinct classes [37], as illustrated in Figure 1C. Moiré patterns, commonly observed in various natural and synthetic materials, have sparked intense interest in TMDC research due to their remarkable potential for engineering emergent phenomena and tailoring material properties.

Figure 2 illustrates the historical research trend on MX_2-based materials over the last five years compared to the most studied 2D-layered materials. The visual representation provides valuable insight into the evolution of scholarly publications in this 2D-layered materials field, showcasing the increasing interest and activity surrounding MX_2 research. This trend underscores the relevance and potential of MX_2-based materials in advancing scientific knowledge and technological innovation. Therefore, we can consider such systems to be a hot topic in the field of materials chemistry.
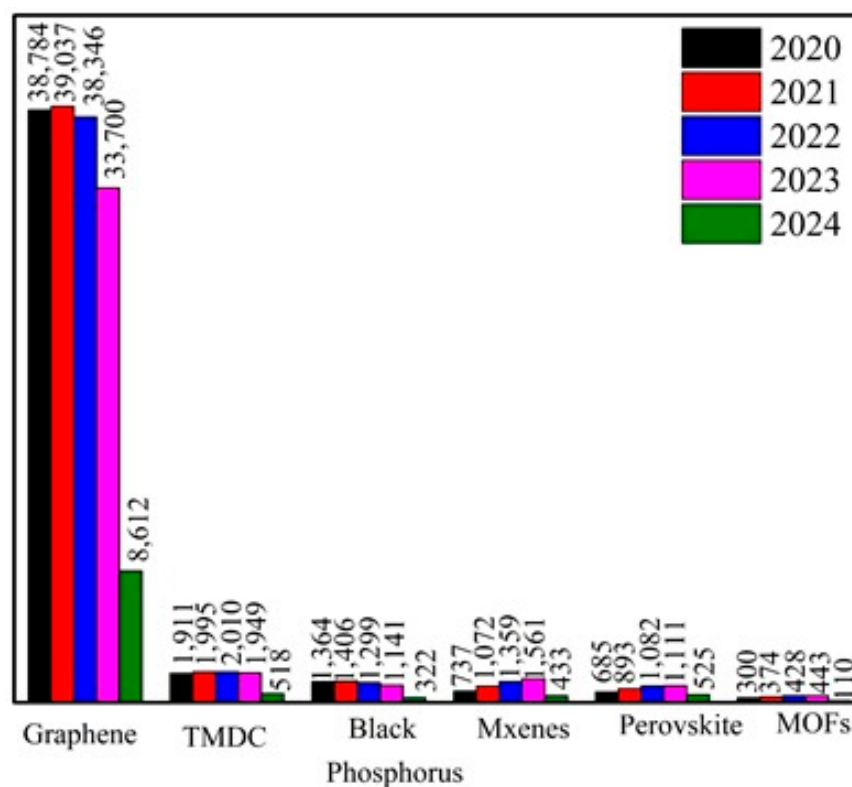
Figure 2. An analysis of the importance of the 2D-layered materials (e.g., TMDCs, graphene, MOFs, and perovskite) from 2020 to 2024 by the Web of Science database (26 April 2024).

Therefore, this review provides an overview of the recent literature on MX_2-based materials (with M = Mo and W and X = S, Se, and Te). In the following sections, we will highlight an overall brief based on the experimental/theoretical approaches and use this combination to thusly provide new guidelines for rationally developing diverse innovative applications based on MX_2-based materials. Notably, these MX_2-based heterostructures feature moiré patterns that have a renowned potential for application across various fields of knowledge, spanning physics [69–73], chemistry [74–81], engineering [82,83], and biology [17,84–91]. We then discuss the moiré superlattices that can particularly promote the appearance of interlayer excitons and thus lead to new nanoscale functionalities, opening up new avenues for many emerging technologies. Lastly, the present review also showed that this analysis of the various synthesis protocols is widely used in obtaining both MX_2 and MX_2-based materials for optoelectronic and photo(electro)catalytic applications.

2. Main Types of Layered TMDCs and Their Characteristics

The chosen scope of this review encompasses the investigation of the MX_2-based materials (with M = Mo and W, and X = S, Se, and Te) into different architectures, and provides a comprehensive overview of their properties, synthesis methods, and emerging optoelectronic and photo(electro)catalytic applications. However, despite the recent advances, these materials are still not thoroughly explored industrially. Through an in-depth exploration of these 2D-layered materials, we seek to contribute to the understanding of MX_2-based materials and their relevance in advancing technological innovations (see Table 1).

Table 1. Bandgap values and the applications of the single-layer MX_2-based materials in the literature.

2D Material	Bandgap	Literature
MoS_2	2.18 eV [92]	most studied
WS_2	2.40 eV [92]	well studied
$MoSe_2$	1.63 eV [93]	well studied
WSe_2	1.66 eV [93]	reasonably studied
$MoTe_2$	1.10 eV [94]	reasonably studied
WTe_2	0.70 eV [95]	few studied

2.1. Molybdenum Disulfide (MoS₂)

In the diverse family of TMDCs, one compound that stands out is MoS_2, where two planes of sulfur anions are sandwiched between a sheet of molybdenum cations [96]. Notably, it is well known that MoS_2 forms a stable 2D structure and presents distinctive electronic, optical, and catalytic properties [97–100]. In the 1970s, researchers discovered that MoS_2-based catalysts exhibited remarkable efficiency in hydrodesulfurization processes, crucial for removing sulfur impurities from petroleum feedstocks to produce cleaner fuels. MoS_2 catalysts doped with Ni and Co became integral to the petroleum refining industry, enabling the production of low-sulfur fuels in compliance with environmental regulations [99–101]. Additionally, MoS_2 is widely used in the automotive, aerospace, and manufacturing industries as a solid lubricant to reduce friction and wear in mechanical devices [101,102].

Due to the ease and robustness of its synthesis, MoS_2 has become the most extensively studied material in the TMDC family [19]. While graphene exhibits a gapless band structure [7], in particular, 2H-MoS_2 can tune its band structure by simply adjusting the number of packed layers along the basal direction [103]. Like other TMDC materials, MoS_2 features inert basal planes and active sulfur edge-sites, and increasing the density of these ligands can enhance both their chemical and electronic properties [104–107]. The intrinsic properties of layered MoS_2 are dependent on its layer number and it could be related to the reduction in vdW interactions, which is one of the main reasons why this dichalcogenide-layered material is of great interest [108]. Despite being a weak interlayer interaction, the weak vdW interactions play an important role in the electronic structure of MoS_2 and, consequently, in its relevance for optoelectronic device applications [109,110]. Also, it is well-known that 1T-MoS_2 is metastable and 3R-MoS_2 is stable, and they undergo a transformation into 2H-MoS_2 after heating [24,111–114].

Certainly, a single layer of 2H-MoS_2 functions as a semiconductor with the ability to absorb both visible and near-infrared regions of the electromagnetic spectrum. This property renders it highly suitable for integration into various optoelectronic technologies (e.g., photodetectors, sensors, solar cells, and so on) [115,116]. Few-layer 2H-MoS_2 exhibits remarkable light-absorption capabilities, capturing between 5 and 10% of all incident light within a mere thickness of about 1 nm, surpassing the GaAs and Si semiconductors by more than an order of magnitude [117]. Ongoing research is exploring its potential

and developing new techniques for its synthesis and integration into advanced high-performance devices.

Another pivotal characteristic of the 2H-MoS$_2$ single layer is its exceptional charge carrier mobility, boasting values around 200 cm^2 Vs^{-1} and having a high on/off current ratio, making them useful for their use in field-effect transistors (FET) and other electronic devices [27,36,41,44,45,118]. Moreover, 2H-MoS$_2$ showcases excellent chemical stability, hence being generally stable in the presence of acid, alkaline, or organic solvents [119]. These discoveries sparked interest in using MoS$_2$ as a potential alternative to traditional semiconductor materials such as silicon. Additionally, understanding the mechanical behavior of 2H-MoS$_2$ in its layered form is crucial for designing robust and reliable devices. The findings in this field contribute to the ongoing development and engineering of MoS$_2$-based devices with enhanced mechanical properties and expanded possibilities for future applications [120–122]. In this field, efforts continue to be directed towards exploring novel synthesis methods, understanding the underlying physics, and unlocking the full potential of MoS$_2$ and its moiré superlattices for future technological advancements.

2.2. Tungsten Disulfide (WS$_2$)

WS$_2$ has gained prominence in the scientific community due to its outstanding performance across various applications, such as catalyst [18,123], sensors [124], and cancer therapy [125], as well as its utilization in aerospace, automotive, textile, and food industries [126]. Its utility extends to medical imaging, where WS$_2$ serves as a contrast agent for tomography, facilitating the non-invasive imaging of biological structures [17]. Studies have shown that WS$_2$ exhibits high catalytic activity in reactions such as hydrogen evolution [127], hydrodesulfurization [128,129], and water splitting [130]. Research has shown that WS$_2$ exhibits strong antibacterial properties, making it a promising candidate for use in medical devices and wound dressings [131,132]. Additionally, WS$_2$ exhibits a potential for drug delivery applications, particularly in cancer therapy and other medical treatments [133,134]. One of the most promising applications of WS$_2$ is in the field of opto-electronics, where it has shown great potential for use in photovoltaic cells, light-emitting diodes (LEDs), and lasers [135–137]. With its high absorbance and photoluminescence efficiency, WS$_2$ offers compelling advantages for such applications.

For single-layer 2H-WS$_2$, the bandgap value is approximately 2.03 eV, making it well suited for absorbing photons in the visible and near-infrared regions of the electromagnetic spectrum [126]. When integrated into photovoltaic devices, WS$_2$ can efficiently convert absorbed light into electrical energy, contributing to improved device performance and overall conversion efficiency. Recent studies on WS$_2$ single layers have yielded an estimated charge carrier mobility of about 44 cm^2 V^{-1} s^{-1} at room temperature [138]. Its unique electronic structure and high luminescence efficiency make it an attractive material for use as an emissive layer in LED devices. By incorporating WS$_2$ as an active material, LEDs can achieve enhanced light emission properties, including higher brightness, better color purity, and improved energy efficiency [139–141]. WS$_2$-based LEDs hold promise for various applications, from display technologies to solid-state lighting solutions, where their superior performance can significantly impact energy consumption and lighting quality.

The crystalline WS$_2$ structure has two primary polymorphs, which are the 1T and 2H phases [142]. The 1T phase, also known as the octahedral phase, possesses a distorted octahedral coordination geometry around the tungsten atoms, resulting in metallic properties with a reduced bandgap [143]. On the other hand, the 2H phase, also called the hexagonal phase, exhibits a hexagonal lattice structure with alternating layers of tungsten and sulfur atoms, leading to semiconducting behavior with a relatively larger bandgap [144]. Within each polymorph, WS$_2$ can exist in different polytypes, denoted by the number of layers in the unit cell and the stacking arrangement of these layers. The 2H polytype of WS$_2$ is the most common form and hence has garnered significant attention for applications in electronics and optoelectronics devices, due to its semiconducting behavior and tunable bandgap. In contrast, the metallic properties of the 1T phase may find applications in

catalysis and energy storage [145,146]. Another polytype of WS_2 is the 3R phase, which features a rhombohedral lattice structure [147]. The 3R phase exhibits unique electronic and optical properties distinct from those of the 2H phase, offering potential opportunities for novel device architectures and functionalities. Hence, WS_2 polymorphs and polytypes offer a rich diversity of structural and electronic properties, making them highly versatile materials for various applications.

Despite the promising properties of 2H-WS_2, it is important to note that it, along with other TMDCs, have a tendency to oxidize at room temperature after being synthesized. This poses a challenge for the large-scale production and practical application of these materials.

2.3. Molybdenum Diselenide (MoSe$_2$)

$MoSe_2$ has garnered considerable attention in recent times for its potential applications in electrochemical, photocatalytic, and optoelectronic systems [148–162]. As a 2D material, 2H-$MoSe_2$ exhibits a layered structure, wherein a single layer comprises one molybdenum cation and two selenium anions arranged in a hexagonal lattice. Similar to MoS_2, in particular, $MoSe_2$ presents two different polymorphs (2H or 1T). The former demonstrates semiconducting behavior, while the latter is metallic. Previous studies have indicated that the electrical conductivity of the metallic 1T phase of MoS_2 is approximately 107 times higher than that of the semiconducting polytype [155]. However, it is well known that the metallic 1T-$MoSe_2$ phase is thermodynamically metastable and gradually transforms into the disordered 2H semiconducting phase over time. Indeed, while the metallic 1T-$MoSe_2$ phase would be preferable for numerous applications, it is not feasible due to its metastability [148].

The 2D-layered $MoSe_2$ structure makes it an attractive option for hosting counter ions in electrochemical energy storage systems, including lithium-ion and sodium-ion batteries. Additionally, the unsaturated Se anions located at the edge, along with those at defective points or altered basal planes, exhibit superior electrocatalytic activity towards hydrogen evolution reaction (HER) [149–151] and similar electrocatalytic reactions (e.g., in lithium-oxygen batteries) [152–154].

One of the most remarkable properties of 2H-$MoSe_2$ is its direct bandgap of about 1.8 eV in a monolayer, rendering it a promising candidate for various optoelectronic applications such as photodetectors, light-emitting diodes, and solar cells [155]. Furthermore, 2H-$MoSe_2$ boasts high carrier mobility as well as excellent thermal stability, which makes it suitable for high-performance electronic devices. Additionally, its tunable bandgap makes the 2H-$MoSe_2$ phase a promising candidate for applications in photocatalysis and photoelectrochemical solar cells.

$MoSe_2$ and MoS_2, which are transition metal dichalcogenides belonging to Group 6, are ideal for use as photoelectrodes in regenerative electrochemical solar cells due to their resistance to photodecomposition. Photogenerated excitons in these materials arise from non-bonding d- orbitals, meaning that photo-initiated reactions resulting from these transitions do not directly lead to bond breaking [148].

The synthesis and processing of $MoSe_2$, including etching techniques, are critical for the development of high-performance devices. Various promising techniques have emerged for precise control over the number of packed layers and surface morphology of 2H-$MoSe_2$. Further research in this area is expected to significantly contribute to the advancement of electronic and optoelectronic devices based on this material [156–162].

2.4. Tungsten Diselenide (WSe$_2$)

WSe_2 has emerged as a promising material across diverse applications owing to its excellent physical properties, easily customizable by adjusting the thickness [163]. As is well known, the WSe_2 has a hexagonal lattice structure and has two polymorphs, the 1T and 2H phases, distinguished by the coordination of chalcogen anions with central metal tetravalent cations. The H phase, which has trigonal prismatic coordination of metal cations, is stable and naturally occurring, while the 1T-WSe_2 is a metastable phase with

octahedral coordination of W atoms, being paramagnetic and metallic [163]. Generally, inducing external energy facilitates the transformation of 1T-WSe$_2$ into the more stable 2H phase [164].

It has a direct bandgap of approximately 1.6 eV, which is ideal for various optoelectronic applications. WSe$_2$-based devices have demonstrated high responsivity, speed, and performance, making them suitable for digital logic applications and solid-state lighting [165]. In addition, 2H-WSe$_2$ also exhibits strong photoluminescence and excellent charge carrier mobility [164]. Also, the dark exciton emission of 2H-WSe$_2$ makes it ideal for optoelectronic devices with bright emissions at room temperature. Furthermore, 2H-WSe$_2$-based LEDs have also been demonstrated to exhibit high efficiency and can potentially be used for solid-state lighting [166,167].

The electronic bandgaps can be controlled by manipulating the lateral dimensions of 2H-WSe$_2$ to form quantum dots (QDs), resulting in a broad range of emission wavelengths and optimized band edge positions crucial for electro/photocatalytic water splitting. However, to propel the advancement of this technology, it is necessary to have a comprehensive understanding of the mechanisms and limitations of different synthesis techniques aimed at effectively controlling the particle size and shape of as-prepared WSe$_2$ QDs [163]. Overall, 2H-WSe$_2$ holds significant promise for a wide range of emerging optoelectronics applications, and ongoing research in this area is likely to lead to further advances in this promising material.

2.5. Molybdenum Ditelluride (MoTe$_2$)

MoTe$_2$ is a material that has recently gained significant attention due to its unique properties such as strong spin–orbit coupling, controllable phase transition, and a narrow bandgap similar to silicon. MoTe$_2$ is highly stable in semiconducting and metallic phases, making it suitable for various applications. These characteristics make it an ideal candidate for applications such as type II Weyl semimetals/quantum spin Hall insulators, in-plane homojunction devices, and high-performance IR detectors [168].

MoTe$_2$ has four possible polymorphs/polytypes, including semiconducting 2H, metallic 1T, semi-metallic 1T′, and non-centrosymmetric 3R phases. In nonlinear optical second-harmonic generation signals in centrally symmetric phases, change with the alternation of odd/even layers has been shown to provide a fast detection technique for identifying crystal symmetry and orientation [169].

In recent years, research on MoTe$_2$ has focused on understanding its electronic and optical properties and developing devices based on this material [170]. MoTe$_2$ has been demonstrated to have excellent photoresponse properties, making it a promising material for fabricating FETs with high on/off ratios and low power consumption, that is, indicating its potential for use in low-power electronics [171].

Also, it has been shown that MoTe$_2$ is a promising material for constructing p-channel metal–oxide–semiconductor field-effect transistors (MOSFETs) and for integration with 2H-MoS$_2$ n-channel MOSFETs, but its broad bandgap limits its applications in near-infrared photodetection. To enhance its performance in optoelectronics, different approaches have been investigated, including the introduction of a BP/MoTe$_2$ junction. However, the photocurrent characteristics of this junction were not as high as expected, with small values of photoresponsivity and external quantum efficiency, possibly due to the critical nature of BP, which is prone to oxidation [172].

In addition, MoTe$_2$ has been investigated for its catalytic properties, particularly in HERs [173,174]. The material has also demonstrated promising catalytic activity for HERs, which is usually attributed to the presence of Te vacancies and edge sites on the surface of the layered material [175]. Overall, MoTe$_2$ is a promising member of the TMDC family with unique electronic, optical, and catalytic properties. Continued research on the material is expected to drive the development of new technologies utilizing this material.

2.6. Tungsten Ditelluride (WTe$_2$)

WTe$_2$ presents topological behavior, exhibiting type II Weyl semimetal behavior in its bulk form and quantum spin Hall insulator behavior in its monolayer form, superconductivity, and magnetoresistance properties [176]. Despite being studied for decades, recent research has provided new insights into its structure and properties [95]. In addition to the aforementioned properties, WTe$_2$ is a material with many interesting electronic properties, including turn-on behavior, multi-Fermi pockets, small Fermi surface anisotropy, and ferroelectricity. However, the evolution of its electronic structure and topological properties as the crystal thickness decreases remains unclear [168].

Under ambient conditions, WTe$_2$ typically exists in the orthorhombic (Td) phase, where tungsten cations are octahedrally coordinated with tellurium anions [177]. The WTe$_2$ properties have been extensively modeled to achieve better performance in their applications as semiconductor materials, primarily based on a 2H structure. However, experimental/theoretical investigations indicate that WTe$_2$ favors a distorted 1T (Td) structure as its lowest energy state [95]. Lee et al. [95] conducted a study on bulk and exfoliated, crystalline WTe$_2$ synthesized under near-equilibrium conditions. Their findings revealed that WTe$_2$ has a distorted 1T structure and displays semi-metallic electronic characteristics, consistent with early theory and experiments dating back to the 1960s [178,179]. This highlights the vital role of experimental studies in elucidating/determining the true properties of TMDC materials and emphasizes the need for a deeper understanding of their chemical nanoscale behavior for emerging optoelectronic applications [95]. Overall, the diverse electronic properties of WTe$_2$ make it a promising material for various electronic applications, and further studies are needed to fully understand its behavior.

3. Controlled Synthesis

The potential applications of MX$_2$-based heterostructures are up-and-coming, and research in this field is progressing rapidly; numerous challenges still need to be overcome before these structures can be used industrially. Foremost among these challenges is synthesizing these structures in a large area with a low density of electrically active defects [180]. Additionally, it is crucial to ensure the absence of contaminants intercalated between the 2D layers.

Overall, in this domain, the study of defects and imperfections in crystals, particularly in 2D TMDCs, presents a unique opportunity to tailor their properties for various applications in optoelectronics, catalysis, energy storage, and more [181]. Understanding the role of complex defects allows researchers to develop new strategies for enhancing 2D material properties and performance [182]. Through synthesis techniques, theoretical modeling, and characterization methods, researchers can fabricate and analyze TMDCs, uncovering structure–function relationships and facilitating the development of TMDC-based devices for electronics, optoelectronics, catalysis, and energy storage applications.

As we know, the top-down and bottom-up approaches are widely used in the literature to obtain the 2D-layered TMDC structures. The top-down method involves synthesizing 2D materials from 3D counterparts by breaking intermolecular bonds, while the bottom-up approach entails building 2D materials from individual atoms and molecule precursors. Figure 3 presents an overview of the synthetic methodologies utilized in acquiring 2D-layered TMDCs, as discussed within the context of this review.
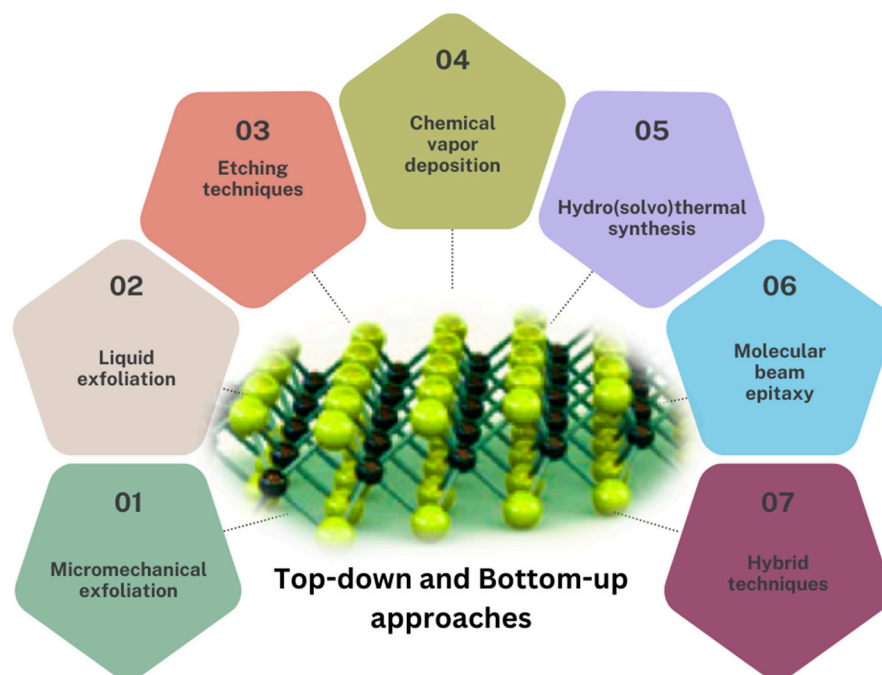
Figure 3. Scope of review toward synthetic approaches adopted to obtain 2D-layered TMDCs.

3.1. Micromechanical Exfoliation

Graphene was originally obtained by the micromechanical exfoliation of natural graphite [7], using a top-down approach. This process involves utilizing adhesive tape to exfoliate high-purity graphite single crystals, which are subsequently affixed to a substrate, usually atomic flat silicon oxide. This strategy has also been applied to many other 2D materials that are found in 3D stacked forms, both from natural minerals (e.g., $2H\text{-}MoS_2$) and artificially synthesized crystals (e.g., black phosphorus) [183]. Typically, this mechanical exfoliation approach produces high-quality material, which is ideal for fundamental studies related to the thickness-dependent properties [109], but is not scalable [184], as the crystal obtained is irregular and the areas obtained are very small (micrometer scale).

By controlling the exfoliation process to obtain predominantly monolayer or few-layer particles, researchers can tailor material properties such as bandgap, carrier mobility, and optical absorption for specific device requirements. In particular, Wang et al. demonstrated that $2H\text{-}MoS_2$ could be exfoliated into monolayers using Scotch tape [185]. In 2011, Coleman et al. [186] used mechanical exfoliation to obtain monolayer and few-layer flakes of a variety of TMDCs, including MoS_2, $MoSe_2$, WS_2, and WSe_2. They demonstrated that the resulting flakes had high crystal quality and were suitable for use in electronic and optoelectronic applications. Since then, micromechanical exfoliation has continued to be a popular technique for obtaining high-quality 2D materials, with researchers using a variety of tools and methods to improve the yield and quality of the resulting flakes.

Ali et al. [187] also reported the successful exfoliation of MoS_2 using micromechanical cleavage, which allowed them to obtain single-layer and few-layer flakes with a lateral size of several micrometers. Other TMDCs, such as $MoTe_2$ [187], WS_2 [188], MoS_2 [188,189], and $MoSe_2$ [190–192], have also been obtained using micromechanical exfoliation, demonstrating the effectiveness of this method for obtaining a wide range of 2D materials.

For WSe_2 synthesis, this method was also used to mechanically cleave bulk WSe_2 using adhesive tape or other similar methods to produce thin flakes. WSe_2 crystals are formed by weakly bonded layers through non-covalent bonds. This weak interlayer bonding in WSe_2 allows for an easy fabrication of single layers through the micromechanical exfoliation method. This approach facilitates the fabrication of high-quality, single-layer WSe_2 flakes, which have been used in various optoelectronic devices [193].

Shackery et al. [194] have developed a back-to-back diode by connecting two α-MoTe$_2$-based Schottky diodes in series for the first time using micromechanical exfoliation. The α-MoTe$_2$ Schottky diodes showed excellent performance with an on/off current ratio of about 103, enabling a low-voltage operation at 5 V. Previous studies have investigated α-MoTe$_2$ FETs, phototransistors, and p-n diodes, but there has been no research on the potential of α-MoTe$_2$ for chemical sensing, either experimentally or theoretically.

Although micromechanical exfoliation remains a widely adopted technique to obtain high-quality single- and few-layers of TMDC, it has several limitations. One of the main limitations is the low yield of the method, which makes it difficult to obtain large amounts of material. Moreover, the method is time-consuming, and the process of exfoliation is often unpredictable, resulting in significant variations in both the size and quality of the obtained flakes. Therefore, there is a need to develop new synthetic methods that can overcome these limitations and provide a reliable and scalable approach to produce TMDCs with high quality and quantity. Continued research in this area will advance our understanding of TMDC synthesis and enable the development of next-generation devices endowed with superior functionality as well as performance.

3.2. Liquid Exfoliation

To tackle the scalability challenges of the micromechanical method, researchers have developed more robust exfoliation techniques utilizing a solution-based chemical separation of 2D crystals [186]. Originally, the intercalation and exfoliation of 2H-MoS$_2$ were described in the eighties and consisted of intercalating Li$^+$ between the layers of 2H-MoS$_2$ using a reducing agent like n-Buthyllithium [195,196]. The exfoliation occurs by dispersing the LiMoS$_2$ in water, using an ultrasound bath. A partial oxidation occurs, releasing H$_2$, and compounds with the composition 1T-Li$_x$(H$_2$O)$_y$MoS$_2$ are obtained and dispersed in solution, which can be fully chemically oxidized in the sequence to obtain metastable 1T polytypes [195,196]. Liquid exfoliation is a well-established method for the synthesis of 2D TMDCs [155–157]. The resulting delaminated/exfoliated flakes are then separated from the dispersion and further processed to remove any residual solvent or surfactants. Liquid exfoliation has proven to be an effective method for synthesizing high-quality 2D materials, with a high degree of control over the size and thickness of the flakes produced [197].

The methods used to separate the layers inside the solution can vary, but they often involve a chemical intercalation or ultrasonic process that yields relatively large volumes of flakes from one or a few layers dispersed in the solution [186]. Nevertheless, it is well known that aggressive interleaving tends to degrade crystal quality as well as introduce impurities/defects unfavorable to many optoelectronic applications.

For stacking the exfoliated materials and forming the heterostructures, a microscope equipped with micromanipulators is crucial in wet and dry transfer methods to properly align the micrometer scale flakes. The first assembly step is the deposition of mechanical exfoliated TMDCs on an existing substrate. A second flake can then be dry-exfoliated or wet-transferred using a polymer. The polymer flake is then transferred to a transparent seal, which is positioned using the micromanipulators in the desired position and orientation (relative to the first flake) under the objective lens and positioned until the two flakes make contact to form the heterostructures [198]. Despite working for fundamental studies of the properties of vdW heterostructures, this transfer method becomes completely unfeasible for industrial application, considering that it is necessary to visually find and analyze the flakes of materials and manually deposit them one on top of the other.

A variation of the technique is grinding-assisted exfoliation, where single- and few-layers are peeled from bulk 2H-MoS$_2$ by shear forces, followed by breaking the detached layers into small pieces through sonication [187]. The impact and friction forces peeled smaller pieces, while shear forces exfoliated single- or few-layer sheets. The developed method successfully produced a few-layer MoS$_2$ with lateral sizes of several hundred nm and good dispersibility [187]. In a study carried out by Yao et al. [199], single-layer and few-layer particles were prepared by a less-energetic shear exfoliation process from bulk MoS$_2$

crystals using N-methyl-2-pyrrolidone (NMP) as a surfactant, which has a high boiling point and good solubility for many TMDCs [200]. The exfoliation process [199] involved the wet grinding of 2H-MoS$_2$ crystals in NMP followed by sonication in a 45 vol% ethanol/water solution. Organic solvents such as dimethylformamide and dimethyl-sulphoxide led to a reduced concentration of exfoliated nanosheets [187].

Other solvents such as isopropanol, ethanol, and water have also been used for TMDC exfoliation with varying degrees of success [197]. The choice of solvent depends on the specific properties of the TMDC being exfoliated, such as its crystal structure, size, and chemical stability.

In another study by Ibrahem et al. [201], MoS$_2$ QDs were exfoliated using a ball-milling-assisted wet grinding process. During the grinding process, in particular, bulk 2H-MoS$_2$ powder was mixed with pure ethylene glycol and zirconia beads in a ball mill, operating at a constant rotating speed for 8 h.

In addition to the choice of solvent, the exfoliation process can also be optimized by controlling the energy input during the exfoliation process [202]. Ultrasonication is a common method for energy input, but the frequency, power, and duration of sonication can all affect the quality of the exfoliated flakes [203,204]. For example, employing higher power and longer sonication times can yield smaller and thinner flakes, whereas lower power and shorter sonication times may produce larger and thicker flakes [205].

While the stacking of the exfoliated materials of 2D materials has been widely used in research for fundamental studies of vdW heterostructures, it may not be practical for industrial applications due to its reliance on manual manipulation and the visual identification of individual flakes. This process can be time-consuming and labor-intensive, making it difficult to scale up for industrial production. However, recent advances [206,207] in transfer methods have shown promise in enabling the large-scale production of heterostructures with controlled layer thickness and orientation, which could potentially overcome the limitations of the possible subsequent restacking [208,209]. These methods offer a more automated and reproducible approach to the fabrication of heterostructures, making them more suitable for industrial applications.

It is important to emphasize that single layers can only be obtained after dispersing the powders into a solvent and after depositing the dispersion into a substrate. Single layers can be only obtained if the concentration of the particles is very low; otherwise, turbostractic disordered packing of the layers will be obtained.

3.3. Etching Techniques

Etching is a versatile top-down approach to removing a specific material from another by chemical or physical methods. In 2D materials, this powerful technique could be used to control the layer number to change the bandgap value. Atomic Layer Etching (ALE) has been widely used to obtain high-quality 2D materials, including TMDCs [210]. ALE is a selective etching technique that can remove a precise number of atomic layers without damaging the substrate, which is essential for thickness control and device fabrication [211].

One of the possible methods is careful top-down layer removal by using sequential Cl-radical or F-radical adsorption and Ar$^+$-ion desorption. This process highlighted the non-contamination and substrate preservation [103]. In another use of the etching technique, Kim et al. described a mechanism to fabricate a single-layer 2H-MoS$_2$ FET from a bulk crystal in which the characterization reveals a similar electrical performance to a pristine 2H-MoS$_2$ FET device [212].

The surface oxidation of MoS$_2$ by O$_2$ plasma is a potential method for the layer thinning process, in which a MoO$_x$ surface layer formed is desorbed by a post-annealing treatment. The surface oxidation is a function of both the time of plasma exposure and the temperature applied to the substrate [211,213]. In some cases, a re-sulfurization process is necessary to recover the remaining substrate in a complete MoS$_2$ film. Chen et al. [214] described this process to obtain MoS$_2$ single layers with an enhanced photoluminescence intensity from a pristine bi-layer MoS$_2$. When the etching is performed by plasma, the

close distance between the MoS_2 sample and the highly energetic species can cause depth lattice etching, resulting in a non-uniform oxidation process [215]. Based on that, Zhu et al. [213] showed a controlled MoS_2 thinning process using a remote O_2 plasma, in which the underlying substrate structure and chemical composition remained unchanged due to the recombination of the ions and electrons before reaching sample surfaces.

Kim et al. [212] used Cl radicals as adsorption species and low-energy Ar^+ ions as desorption species for the ALE of MoS_2. Hence, the ALE technique demonstrated that a single-layer MoS_2 FET fabricated after one cycle of ALE had similar electrical characteristics to a pristine single-layer MoS_2 FET. The ALE technique can also be applied to all layered TMD materials, such as WS_2, $MoSe_2$, and WSe_2 [216]. A MoS_2 ALE mechanism was reported based on experimental and simulation results, where $S_{(top)}$, $Mo_{(mid)}$, and $S_{(bottom)}$ charged species were sequentially removed from the MoS_2 crystal structure due to trapped Cl atoms between the $S_{(top)}$ and the $Mo_{(mid)}$ sheet.

Nipane et al. [217] reported on the development of an ALE process for layer-by-layer removal of WSe_2, which enables control over the layer thickness and pattern of 2D materials. Thus, the ALE process selectively removes the topmost layer of WSe_2 without affecting the physical properties of the underlying layers, enabling the fabrication of high-performance 2D devices. Optically and electrically characterized ALE-treated layers demonstrate a quality equivalent to pristine layers. Using graphene as a standard, the article demonstrates the production of ultra-clean 2D devices employing a sacrificial single layer of WSe_2, which is etched in the final process step, resulting in high-performance field-effect transistors with room-temperature mobilities of up to 200,000 cm^2 V^{-1} s^{-1} [217].

Le Thi et al. [218] have successfully created a lateral p-n junction diode using a combination of edge and surface contacts in WSe_2. High-resolution transmission electron microscopy (TEM) confirmed the presence of amorphous WO_3 at the etched WSe_2 and the formation of a junction near the edge contact. The device showed a high on/off ratio for both the edge and surface contacts, with values of 107 and 108, respectively. Additionally, the diode demonstrated an exceptionally high mobility of up to 168 cm^2 V^{-1} s^{-1} and a rectification ratio of 10^3. Additionally, Lee et al. [219] showcased a self-aligned fabrication process based on self-terminated p-doping and layer-by-layer chemical etching to achieve effective channel control with low contact resistance and high on/off current ratio in ultrathin WSe_2 FETs. This approach is necessary since selective ion implantation is commonly used in Si and III–V semiconductors; however, it cannot be adopted for ultrathin vdW materials.

In addition to ALE, other etching techniques such as reactive ion etching (RIE) and wet etching have also been employed for $MoSe_2$ etching [220]. RIE, a dry etching method, utilizes plasma to remove material from a surface, whereas wet etching involves the use of a chemical solution to dissolve the material [221]. Both techniques have advantages and disadvantages, depending on the specific application and desired etching parameters.

The etching technique is a versatile approach with the possibility to use physical and chemical methods to layer and edge control, in addition to defining special nanostructures for optoelectronic applications [214]. However, the literature pinpoints the investigation of more accurate control of the parameters to improve the uniformity of the etching layers [53,54]. One major limitation is that ALE can only remove materials that can be selectively etched, which means that the material to be removed must have different chemical or physical properties from the substrate. Additionally, ALE is typically a slow and time-consuming process, which can limit its practicality for high-volume manufacturing. Another limitation of ALE is that it requires the use of hazardous gases and high-energy plasmas, which can pose safety risks to operators and require specialized equipment for handling and disposal. Furthermore, ALE can also result in the roughening of the substrate surface and the formation of defects or damage, particularly if the process conditions are not carefully controlled.

3.4. Chemical Vapor Deposition (CVD)

Currently, chemical vapor deposition (CVD) processes have been widely utilized to obtain numerous 2D materials like graphene [222], h-BN [223], and various TMDCs [224]. In CVD, gaseous, liquid, or solid precursors containing the material of interest are exposed to high temperatures, causing vaporization and subsequent deposition onto the heated substrate surface, resulting in the formation of high-quality films.

While CVD enables the production of high-quality single layers over large areas, it needs a transfer step for layer stacking, potentially introducing contaminants between layers [184]. Consequently, a detailed study of the physicochemical properties of the resulting nanomaterials after each growth stage is imperative [225].

CVD is frequently used to prepare TMDCs materials as MoS_2, in which occurs the reaction of sulfur and MoO_3 in the vapor phase. In the CVD method, adjusting parameters such as temperature and reaction time can control the physical properties of the resulting material [226]. Jian et al. showed the efficient approach of heating the S and Mo sources at different times to prepare a MoS_2 nanomaterial with a uniform triangular morphology and a superior single-layer structure, thereby avoiding the MoO_3 formation at low temperatures [227].

Moreover, CVD allows for the precise growth of 2D-layered materials with diverse morphologies and structures. Zhang et al. [228] achieved an asymmetric spiral structure of layered 2H-MoS_2, suggesting its potential application in optoelectronics and device fabrication. The synthesis and processing of 2H-$MoSe_2$ have received significant attention [229,230]. For instance, the direct elemental reaction between Mo and Se is not possible due to the significant difference in their melting points (2623 and 220 °C, respectively). CVD emerges as the most effective method, involving the reaction of MoO_3 and selenium powder at elevated temperatures to produce high-quality $MoSe_2$ films with precise thickness control [230]. However, it is well-known that flat 2D layers are typically formed only at temperatures exceeding 800 °C, which are necessary to overcome the activation barrier.

Liu et al. [231] report the growth of single-layer and few-layer WSe_2 flakes through ambient pressure CVD on silica substrates. The study showed tunable transport properties for the as-prepared WSe_2 single layer. Gong et al. [232] synthesized TMDC heterostructures via two-step CVD with a potential application in electronics and energy harvesting. The heterostructure was produced first by depositing $MoSe_2$ layers and after by the epitaxial growth of WSe_2. This strategy was used due to its advantages: (i) it can control the spatiality and size of each 2D component, (ii) it yields well-defined 2H and 3R stacking in the WSe_2/$MoSe_2$ bilayer regions, and (iii) it results in interfaces within the plane sharper than $MoSe_2$/WSe_2 heterojunctions. The resulting heterostructures exhibit the rectification characteristics of a p-n junction and boast an internal quantum efficiency of about 91% when employed as gas photodetectors. This study detected a photovoltaic effect, indicating incident photon to converted electron (IPCE) efficiencies of approximately 0.12% [232].

Sassi et al. [233] demonstrate the possibility of the low-temperature growth of WSe_2 using moisture-assisted defective WO_3 precursor powders. Through DFT calculations, the mechanism by which moisture promotes defect formation on the precursor crystal structure, leading to the reduction in the growth temperature, is elucidated. The results showcase the high quality of WSe_2 grown at 550 °C, enhancing the understanding of nucleation and growth mechanisms at low temperatures. Additionally, it offers a practical strategy for the growing of TMDC at temperatures conducive to compatibility with current silicon technology for back-end-of-line processes.

Feng et al. [234] introduce a NaCl-assistant method for growing large-size WSe_2 monolayers, achieving domain sizes of up to 0.57 mm on SiO_2/Si substrates. The study investigated the growth behavior of the salt-assisted method and found that the Se_1 and Se_2 vacancy are the main point defects of the materials. The results also show a temperature-dependent evolution of the morphology of single-layer WSe_2, with a screw dislocation growth behavior observed. The article provides a deep understanding of the mechanism underlying the NaCl-assisted growth of large-size WSe_2 monolayers.

It is noted that bottom-up approaches to 2D-layered materials have demonstrated significant success in producing large-area crystals. However, CVD may possess limitations in terms of yielding high-quality 2D-layered materials.

The choice of the synthetic route needs to aim for a pure and uniform TMDC nanomaterial that attends to the desired electronic properties since the lack of nucleation control can create nonuniform domains with different numbers of layers that hinder the control of the band alignment structure [212]. Atomic Layer Deposition (ALD) is a highly specialized technique that allows for the precise growth of thin films to be used in a wide variety of applications [235,236]. Unlike its variant, CVD, ALD employs a unique approach where gaseous precursors are pulsed into the reaction chamber, one at a time, and separated by inert gas purging to avoid gas phase reactions [237,238]. The ALD mechanism is based on the reaction between precursor materials in the gaseous phase, separated into successive surface reactions in a self-limiting process, which enables thickness control by the number of ALD cycles [239]. This self-limiting reaction mechanism ensures perfect conformality and a uniform thickness of the film, even on complex 3D structures [240]. Due to these characteristics, ALD is highly sought after for its ability to deliver superior precision and control in thin film growth [241].

The ALD technique is also a versatile strategy that can be used as a controlling step to prepare pure and uniform MoS_2 nanostructures. Demirtas et al. [127] used this technique to produce a MoO_3 film as a Mo source in a post-CVD/sulfurization step. The authors presented a study of the ALD cycles and annealed temperature to promote uniform nucleation and, consequently, a reproducible growth of MoS_2 with controlled edge length, thickness, and crystal structure [127].

Zhang et al. [242] used a two-step method using CVD and ALD for the preparation of WTe_2 thin films with large size, few defects, and high crystallinity. The method also allowed for precise control over the thickness and large area uniformity. Additionally, they investigated the impact of telluride temperature on the composition of the WTe_2 films, as well as the effects of film oxidation on the composition and magnetic properties.

Martella et al. [243] describe a method for the controlled allotropic phase growth of $MoTe_2$ thin films using CVD from powder precursors. The method involves inducing a concentration gradient of the Te precursor using a physical barrier, which allows for control over flux fluid dynamics, thereby enabling the creation of either a Te-rich or a Te-poor environment. This results in the selective allotropic phase control in the CVD deposition of $MoTe_2$ without the use of growth surfactants. The method also leads to a homogeneous nucleation mode of the $MoTe_2$ crystals, as evidenced by the characteristic shape of the crystallite population as well as their log-normal areal distribution.

Despite the advantages of CVD in the synthesis of TMDCs, there are still some limitations to this technique. One of the main challenges is achieving high quality and uniformity of the thin films over large areas [244]. This is due to the sensitivity of the process to the reaction conditions, which can vary across the substrate surface. Another limitation is the difficulty in controlling the stoichiometry and composition of the TMDC films, which can affect their electronic and optical properties. Moreover, CVD typically requires high temperatures, which can lead to defects, impurities, and even phase changes in the TMDCs. It is well known that the presence of imperfections in TMDC materials can significantly alter their physical properties [245]. In the case of $2H$-MoS_2, for example, it has been reported that the mobility of charge carriers in samples prepared by a standard CVD process is reduced compared to samples produced by mechanical exfoliation [246]. This reduction is due to the presence of structural defects and grain boundaries that scatter the charge carriers. A grain boundary in a two-dimensional material is a linear defect that arises due to the material's growth process, separating two ordered crystalline domains [181]. Hence, the presence of complex defects in such semiconductors can create states in the middle of the gap that are spatially located in the defect and can modify the optical and transport properties of the material [247]. Finally, the scalability of CVD for large-scale production is still a challenge, which makes it difficult to meet the demands of industrial applications.

Therefore, research is needed to optimize the CVD process and overcome these limitations to fully explore the potential of TMDCs in several applications.

3.5. Hydro(solvo)thermal Synthesis

Hydrothermal synthesis consists of a synthesis that involves a bottom-up method that generally uses water (although the use of another solvent is possible, in this case, the method is conveniently called solvothermal) as the solvent to solubilize the constituents and promote recrystallization under controlled conditions of temperature and pressure [248]. The temperatures used generally vary between 100 and 1000 °C, and the pressure is between 1MPa and 1 GPa [249]. As it is a simple method with low apparatus complexity [249], this method is widely used for the study of TMDCs synthesis.

Probably the first hydrothermal synthesis involving TMDCs was performed by Peng et al. [28] in which they varied the temperature between 150 and 180 °C to synthesize single layers of MoS_2 and $MoSe_2$. Zhang et al. [250] synthesized $MoSe_2$ nanoflowers using a hydrothermal route in which sodium molybdate and selenium powder at low temperatures were dissolved in water, added in a single vessel, and treated at 200 °C for 48 h.

Guo et al. [127] used a hydrothermal method involving the reaction between Na_2MoO_4 and L-Cysteine in an acid solution under high pressure and temperature to produce nanoparticles of $2H-MoS_2$. The synthesized MoS_2 nanoparticles were characterized using various techniques, such as TEM, X-ray diffraction (XRD), and Raman spectroscopy, which confirmed the formation of crystalline $2H-MoS_2$. The authors highlight the low cost and simplicity of this method, as well as its potential applications in areas such as energy storage and catalysis. They also suggest that this method can be easily adapted to the synthesis of other TMDCs.

Vattikuti et al. [251] synthesized $2H-WS_2$ using a hydrothermal synthesis technique. The synthesized WS_2 nanoparticles were characterized by various techniques such as XRD, TEM, and Raman spectroscopy. The authors also demonstrated the use of $2H-WS_2$ nanoparticles as a counter electrode in dye-sensitized solar cells.

Hydrothermal synthesis is a simple and inexpensive method for $2H-WSe_2$ synthesis, which involves the reaction of a tungsten and selenium precursor in an aqueous solution at a high temperature and pressure [252]. This method has the advantage of producing WSe_2 in various shapes, such as nanorods [253], nanosheets [254], nanowires [255], and nanoparticles [256].

Chauhan et al. [257] have developed a simple thermo-chemical approach for the synthesis of WTe_2 nanostructures that is more economical and requires lower temperatures compared to other reported methods. The reaction involves the formation of an intermediate compound (H_2Te), and with the help of produced hydrogen, it then reduces WO_3 to WTe_2. A detailed structural and morphological analysis has been presented, and the possible mechanism behind the synthesis process is formulated for better understanding.

From this perspective of renewable energy, $g-C_3N_4$/TMDC heterostructures or hybrids have demonstrated technological viability in the advancement of energy storage systems, including Li-ion batteries. Xu et al. [258] synthesized uniformly anchored WS_2 nanoparticles around the $g-C_3N_4$ nanosheets ($g-C_3N_4@WS_2$) by the solvothermal route. The aim was to investigate this material as a possible lithium-ion battery anode. By adopting a lithium foil as the cathode in electrochemical measurements, the $g-C_3N_4@WS_2$ anode exhibited a large capacity (1136.1 $mAhg^{-1}$ at 0.1C) and superior short-term cycling stability (454.4 $mAhg^{-1}$ after 200 cycles). This excellent result was ascribed to the unique structure achieved through the junction of WS_2 and $g-C_3N_4$, including the formation of a porous structure that beneficiated the contact of active sites with the electrolyte (rich in Li^+ ions).

Despite the numerous advances using hydrothermal synthesis, it is a challenge to produce/manufacture electronic devices in a controlled manner using reactions in an aqueous medium [259]. One of the challenges of hydrothermal synthesis is controlling the particle size and morphology. The particle size and shape can be influenced by various factors, such as the reactant concentration, temperature, pressure, and time of the reaction.

Therefore, it can be difficult to obtain particles with a specific size and shape, which is crucial for some applications.

Another challenge is achieving a homogeneous and reproducible synthesis. The synthesis conditions, such as temperature and pressure, may vary within the reaction vessel, leading to non-uniform synthesis and, therefore, non-reproductive properties for the produced materials. Hydrothermal synthesis also requires specialized equipment, including a high-pressure reactor, which can be expensive and difficult to maintain. Moreover, the high pressure and temperature used in the synthesis can be hazardous and require safety precautions.

Additionally, hydrothermal synthesis can be limited by the solubility of the reactants and products in the water. Some materials may not be soluble in water, or their solubility may be too low to obtain a sufficient yield of the desired material.

3.6. Molecular Beam Epitaxy Growth on Substrate

Another technique that can be used to grow heterostructures is through molecular beam epitaxy (MBE), which is a technique widely used in the semiconductor field to grow high-quality crystalline semiconductor films. Furthermore, MBE can be applied to large areas with a great control over composition and thickness, thus being an extremely suitable technique for the growth of vdW heterostructures. It has already been used to grow graphene [260], h-BN [261], and MoS_2 [262], as well as $MoTe_2/MoS_2$ [263] and h-BN/graphene [264]. The ability to grow each layer in situ (without exposure to atmospheric air) is also very advantageous since it eliminates the presence of impurities between the individual layers.

One of the most important advantages of the MBE method is the high control of growth parameters [265]. However, this ability is often related to the use of specific substrates, generally metallic ones, which are not always compatible with the desired application. To face this problem, it is necessary to develop appropriate and efficient transfer methods from the grown substrate to the appropriate one for device application. Jadriško et al. [266] presented the MoS_2 synthesis by using MBE on a graphene layer and a two-step electrochemical process to promote an efficient transfer of the $MoS_2/graphene$ heterostructure. Using this method, the transfer from an Ir (111) substrate to a Si wafer occurred with a high preservation of the heterostructure, which was ensured by high optical quality and low defects [266].

Roy et al. [267] investigated the growth of $MoTe_2$ and $MoSe_2$ thin films on sapphire substrates by MBE. The films were found to be stoichiometric and layered with atomically smooth surface morphologies. X-ray diffraction confirmed film growth along the [001] direction, and Raman spectroscopy indicated growth in the 2H polytype. Electrical measurements showed an insulating behavior that suggests transport in these films is dominated by localized charge carrier states and can be modeled by a two-dimensional variable-range hopping model [194].

MBE is a versatile thin film growth technique that can be used to synthesize different combinations of TMDCs. By carefully controlling the flux of precursor materials, such as metal and chalcogen atoms, and adjusting the growth conditions, such as temperature and pressure, MBE allows for precise tuning of the chemical composition and crystal structure of the films. This enables the synthesis of various compositions of TMDCs, for example, vanadium-$MoSe_2$ ($V_xMo_{1-x}Se_2$) [268], with controlled stoichiometry and homogeneity. The resulting materials can exhibit unique properties distinct from those of the individual constituent TMDCs, making them promising materials for various applications in electronics, optoelectronics, and catalysis.

While MBE is a powerful technique for synthesizing high-quality films and heterostructures of various materials, including TMDCs, it also has some limitations. One of the main limitations is the complexity and cost of the equipment, which requires a high level of technical expertise to operate. Additionally, the process of MBE is relatively slow and has low throughput, meaning that it may not be suitable for large-scale production. Another

limitation is the limited range of materials that can be grown using MBE, as the technique relies on the evaporation of solid sources in a high vacuum chamber, which may not be suitable for all types of materials. Finally, MBE may also suffer from issues such as poor film adhesion, substrate mismatches, and impurities that can affect the quality and properties of the resulting films.

3.7. Hybrid Techniques

Hybrid techniques involve combining different synthesis methods to achieve specific properties or structures. One such method is the combination of liquid-phase exfoliation and CVD to produce 2D TMDCs with controlled thickness and high quality [269]. In this approach, bulk materials are first exfoliated in a liquid medium to produce multilayer flakes, which are then deposited onto a substrate by CVD. The resulting flakes have a high degree of control over their thickness and excellent crystal quality, making them suitable for various applications [269,270].

Another hybrid technique is the combination of CVD and a plasma-enhanced property, resulting in a plasma-enhanced chemical vapor deposition (PECVD) to synthesize heterostructures of 2D TMDCs and other 2D materials [271]. PECVD involves the use of plasma to enhance the chemical reactions during CVD, resulting in a faster and more uniform growth of the desired structures. This method has been used to synthesize heterostructures of MoS_2/WSe_2, MoS_2/graphene, and other TMDCs with controlled thickness and high quality [272].

A third hybrid technique combines CVD and MBE methods to grow heterostructures of TMDCs and other materials with high precision and quality [19]. By combining CVD and MBE, researchers have been able to grow heterostructures of MoS_2/hBN [273] and MoS_2/graphene with high crystalline quality and well-defined interfaces [274]. Finally, researchers are also exploring the use of TMDCs in combination with other materials to enhance their properties. For example, graphene/TMDCs combined have been shown to have improved mechanical and electrical properties compared to single graphene or TMDC phases [274]. Similarly, TMDCs have been used as fillers in polymer matrices to improve their mechanical and thermal properties [275,276].

4. MX$_2$-Based Heterostructures

In general, the TMDCs properties can be tuned and improved through different approaches to modify the configuration of their structure bands, such as manipulating the thickness of the packed layers [277], incorporating doping species [278], and controlling both density and the nature of defects [279]. Recognizing the relevance of bandgap engineering, the scientific community has successfully employed the concept of heterostructures to improve the multifunctionality of these materials. Heterostructures are created through the combination of two or more layered materials with distinct chemical compositions and different bandgaps. In just a few years, there has been a rapid increase in interest and tremendous progress in the field of vdW heterostructures. The design of a heterostructure involves the appropriate choice and combination of different materials, presenting specific features of *p* and *n*-type semiconductors, optimized band alignments, and suitable arrangement of atomic planes at the interface region (heterojunction) [280]. Such criteria are necessary to minimize the adverse effects of charge carrier recombination through defects (trapping sites), one of the main factors responsible for compromising the effectiveness of optimized multifunctional heterostructures for high-performance applications [281]. The availability of an ever-expanding library of 2D materials with varying electronic properties and the ability to synthesize and stack these crystals into complex heterostructures enables the development of a new generation of electronic and optoelectronic devices with extraordinary performance and unique functionality [184,282–285]. Dong and Kuljanishvili [286] recently reviewed the fabrication process of heterostructures based on TMDC materials.

In the context where only TDMCs are involved, such 2D layered materials are able to produce heterostructures in both vertical and horizontal directions [287]. In vertical

heterostructures, each individual layer of TDMC is stacked on top of one another along the vertical direction. The junction of these layers is held by vdW interactions, and this heterostructure is controlled by the relative orientation and stacking order of 2D sheets. In contrast, the horizontal heterostructures exhibit an organization of layers arranged side by side within the same plane. Hence, in this case, two different TMDC layers are held laterally together due to the covalent/ionic forces [29,288,289]. In general, these heterostructures have been extensively studied in theoretical/experimental studies [290–295], and it has been shown that the band alignment at the interface of semiconductor vdW heterostructures is crucial for their applications.

Among the several possibilities of bandgap alignments, the main categories of hetero-junctions commonly observed for these specific materials are known as type I (straddling gap), II (staggered gap), and III (broken gap) [296,297]. In the type I heterostructure, the CB minimum and VB maximum of the two composite layers (e.g., A and B) obey the following rules: VB-B < VB-A < CB-A < CB-B. Since the VB and CB in the type I heterostructure are in a single layer, in particular, the efficient recombination of the photogenerated electron–hole pairs occurs under illumination. Hence, type I heterostructures are often employed in optoelectronic devices, such as LEDs [295,298]. In contrast, in type II heterostructures, the CB and VB of the two composite layers (A and B) obey the following rules: VB-A < VB-B < CB-A < CB-B. Therefore, VB and CB in type II heterostructures are in different layers. This heterostructure is fundamental in photovoltaic devices because photogenerated electron–hole pairs can be split at the interface, transferring electrons to one layer and holes to the other [295]. As we know, in the case of the heterostructures, the resulting interfaces and the new bandgap alignment promote a substantial enhancement of the electronic properties and enable precise control of the distribution and mobility of electrons and holes [299].

Graphene and $2H$-MoS_2 are 2D materials whose films present extraordinary properties, such as high carrier mobility and tunable bandgap, respectively [300]. However, when applied in optoelectronic devices, some limitations are observed, such as low photoresponsivity owing to the zero-bandgap structure for the graphene, and low carrier mobility for MoS_2 [301]. On the other hand, the combination of these 2D materials to form thin 2D heterostructures has been reported as a strategy to tailor the band structure and improve the carrier mobility to be applied in high-performance optoelectronic devices [98–100,266,302–304]. Kumar et al. [305] demonstrated the successful hydrothermal growth of sulfur vacancy-induced WS_2-rGO heterostructures. For this system, the authors achieved degradation efficiencies and kinetic rate constants of 4-nitrophenol and ciprofloxacin which were 96.95% and 92.30%, and 0.113 min^{-1} and 0.027 min^{-1}, respectively. It is suggested that the rGO acts as an electron mediator, contributing to faster charge separation and lower recombination rates.

To improve the understanding related to the factors that affect physical properties in multilayered systems, Silveira et al. [304] used DFT to study the influence of the stacking order on the electronic and optical properties of vdW heterostructures made of graphene and TMDC. The authors presented that the interlayer binding between TMDC-TMDC is stronger than observed in the graphene–TMDC heterostructure, leading to a greater decrease in the bandgap of the system. Besides that, the optical response was not affected by the stacking order since it is a sum of the individual layers' optical response [304].

The understanding of the electronic properties regarding the charge transfer across the interface between the TMDCs is fundamental to predicting the extending applications of heterostructures in optoelectronic devices [306]. Regarding the type of contact material, it was shown that the graphene/MoS_2 interface presents a ten times larger photocurrent when compared with a Ti/Au/MoS_2 interface, supported by a Schottky barrier two times lower for the graphene/MoS_2 interface [303].

From the synthesis of two-dimensional materials, another field of research has been gaining strength in recent years, which deals with structures and devices made by stacking different 2D crystals [265]. The basic idea behind these structures is to use a 2D material (or with some atomic layers) as a base, MoS_2, for example, and add another 2D material on

top of it, for example, a dielectric such as h-BN. The resulting pile represents an artificial material assembled in a chosen sequence, as in a structure with Lego® [307], with the blocks being precisely defined in an atomic plane. The strong covalent bonds provide in-plane stability of the 2D crystals, while the relatively weak vdW forces are sufficient to hold the stack together. These stacked materials are called vdW heterostructures, and the possibility of producing them has been experimentally demonstrated recently [307].

Another possibility is the use of graphene on the top, in a semiconducting 2D materials class [107]. The issue, in this case, is the control and preservation of a high-quality interface during the graphene transfer [300]. Besides that, these dissimilar 2D structures between graphene and MoS_2 need to be carefully analyzed, since as shown by Diaz et al., the vdW interaction between graphene and $2H-MoS_2$ can decrease the surface bandgap and, consequently, hinder the desired opening of the $2H-MoS_2$ electronic structure [110].

The creation of stacked heterojunction structures between different TMDCs is a useful strategy to tune the physical properties for application in optoelectronic devices. However, heterostructure interactions can promote a narrow indirect bandgap, which can hinder the efficient generation of electron–hole pairs. To address this problem, the strategy of creating a periodically arrayed nanopore structure in a WSe/MoS_2 heterojunction is used to create new defect states, promoting an indirect-to-direct bandgap transition [308]. In addition, the WSe_2/MoS_2 vertical heterojunction device showed excellent diode behavior owing to the atomically sharp hetero-junction p-n diode and an external quantum efficiency of about 12% under an intensity power of 0.5 lW [309]. Graphene electrodes were introduced at both the top and bottom of the vertical MoS_2/WSe_2 p-n junction with the specific aim of mitigating interlayer recombination of majority carriers and accelerating the collection of photogenerated carriers; hence, this strategy achieved an improved external quantum efficiency of about 34% at the MoS_2/WSe_2 multilayer junction p-n [310].

The structural, electronic, and optical properties of MoS_2/ZnO, WS_2/ZnO, $MoSe_2/ZnO$, and WSe_2/ZnO heterostructures were investigated from a computational perspective [293]. These results revealed that vdW forces dominate all these interactions at the TMDC/ZnO interface. Indirect bandgap semiconductor heterostructures MoS_2/ZnO (1.60 eV) and WS_2/ZnO (2.05 eV) were found to be a type II heterostructure, which facilitates the separation of photogenerated electron–hole pairs. These materials showed considerable built-in electric field stabilization. Conversely, direct bandgap semiconductor heterostructures $MoSe_2/ZnO$ (1.96 eV) and WSe_2/ZnO (2.08 eV) were confirmed to be of type I. Hence, these heterostructures serve as efficient solar flux collectors, offering great potential for many optoelectronic applications [295].

Despite all the potential and considerable progress to date, the challenge of turning these prototypes into practical technologies is still huge. Not only are improvements needed in the integration of 2D materials, but also control of their individual synthesis, processability, and performance [311]. For the advancement of this technology, it is essential to develop scalable approaches for the growth of 2D materials and their heterostructures with very well-controlled chemical composition, physical dimensions, relative orientation, and interfacial quality.

For the large-scale application of these structures, the scale-up process of existing technologies should be remarkable. Efforts are already being made to grow 2D structures on top of each other [312–314]. However, achieving this level of perfection on a macro scale is not easy, since as the interactions between the layers are weak vdW, islands appear to the detriment of continuous layers free of contaminants. For the large-scale application of these structures, the scale-up process of existing technologies should be remarkable. Attempts are already being made to grow two-dimensional structures on top of each other [312–314].

Moiré superlattices, arising from the interplay between atomic structure and electron correlations in vdW heterostructures, have exhibited remarkable emergent electronic phenomena. These phenomena, such as superconductivity, magnetism, topological edge states, and exciton trapping, as well as correlated insulator phases, manifest in electron behavior within these structures, surpassing the intrinsic properties of individual layers [315].

Twisted bilayer graphene (tBLG) serves as the prototypical example of vdW heterostructures, characterized by atomically thin layers with unrestricted relative rotational arrangements and the absence of directional bonding between them. The manipulation of the twist angle, denoted as θ, between neighboring crystal lattices leads to the formation of moiré superlattices [316]. These superlattices can be visually observed through scanning probe techniques, showcasing spatial modulation of interlayer coupling. This fascinating property enables the engineering of stack properties by precisely tuning the stacking geometry, as demonstrated by the observation of Hofstadter's butterfly and interfacial polarons in graphene/hexagonal boron nitride heterostructures, along with interlayer excitons in TMDC bilayers [317–325].

The manifestation of strong correlation effects in these systems lies in the heightened Coulomb-type interaction within the 2D environment and the significant reduction in kinetic energy within the flat moiré minibands. In the case of moiré superlattices based on TMDCs, the synergy of large effective mass and strong moiré coupling facilitates the creation of flat bands and engenders stronger electronic correlations, distinguishing them from graphene moiré superlattices [326]. Notably, the WSe_2/WS_2 heterojunction aligned at 0 or 60 degrees exhibits Mott insulating states with transition temperatures surpassing 150 K, which is the highest among all studied 2D moiré systems. Moreover, this system hosts various correlated insulating states at fractional fillings of the moiré lattice, indicative of robust and long-range electron interactions [316].

Furthermore, the significant Coulomb-type interaction in 2D-layered TMDC systems also gives rise to tightly bound excitons with large binding energies. Particularly, the moiré coupling in TMDC superlattices is anticipated to generate excitonic flat minibands, extending beyond the single-particle electronic flat bands in the CB and VB. In recent findings, moiré excitons were identified within angle-aligned WSe_2/WS_2 heterojunctions, which also exhibit correlated insulating states in these structures [324,326]. The existence of excitonic flat bands holds promise for the exploration of topological exciton states and the development of correlated exciton Hubbard models, opening up exciting opportunities for the engineering of intricate quantum states through correlation effects for further research and technological advancements.

Chen et al. [326] studied the impact of adding different layers of WSe_2 in the WSe_2/WS_2 moiré superlattice. They observe changes in the optical spectra of moiré excitons, confirming the moiré coupling interfacial nature at the WSe_2/WS_2 interface. The energy resonances of moiré excitons are, in turn, modified, exhibiting enhanced separation in the WSe_2/WS_2 moiré superlattice. Additionally, the presence of additional WSe_2 layers affects the strength of electronic correlations, as evidenced by a reduced Mott transition temperature. Their findings provide insights into tuning electronic correlations and moiré exciton bands within moiré superlattices based on TMDCs, offering a platform for engineering quantum phenomena arising from strong correlations and Coulomb-type interactions.

When viewed from the perspective of environmental remediation, such 2D/2D heterostructures have offered a sustainable solution in combating pollution through efficient degradation of different hazardous contaminants. For example, the removal process of mercury in gas phase is a very challenging task because of its insolubility in water, high volatility, and non-reactive nature [327,328]. For instance, Xie et al. [329] reported a detailed study on the photocatalytic performance of $g-C_3N_4/MoS_2$ heterostructures in removing gaseous elemental mercury species (H^0). According to these authors, the resulting heterostructure was able to facilitate the light absorption process, increase the specific surface area, and promote an effective separation of photogenerated electron–hole pairs with a low recombination rate. Despite exploring different MoS_2 concentrations in the resulting heterostructure, the most effective photocatalytic activity was achieved for those containing up to 10 wt % MoS_2. In this sample, a notable enhancement in the removal efficiency of H^0 was detected after five recycling runs, reaching 90% and 65.5% under ultraviolet and visible lights, respectively.

Other emerging pollutants found in water bodies through improper disposal are pharmaceuticals [330]. In an effort to remove tetracycline (TC) and sulfamethoxazole (SMX) pharmaceuticals from aqueous solutions, Gnanaguru et al. [331] explored the photocatalytic performance under visible light irradiation of g-C_3N_4/WS_2 heterostructures synthesized by using a facile one-step calcination approach. In principle, the as-synthesized heterostructures were able to remove up to 84% and 96% of TC and SMX, respectively. The obtained values were higher than the individual counterparts of g-C_3N_4 and WS_2. Thus, the remarkably enhanced photocatalytic response was ascribed to the optimized bandgap and the reduced recombination of charge carriers. Another favorable aspect was the absence of non-toxic substances in the final products of photocatalytic tests.

Two-dimensional material heterostructures can also be directly grown chemically just by mixing the components and using high temperatures, normally using quartz ampoules. These obtained materials are called misfit layered compounds (MLCs) and are very abundant in terms of composition, and chemical and physical properties [332–341].

MLCs combine different VdW layers with complex stacking and can be represented by the general ideal formula $[(MX)_{1+y}]_m[TX_2]_n$ where M = Sn, Pb, Bi, Sb, Y, and rare earth elements; T = Sn, Nb, Ta, Ti, V, Cr; and X = S, Se, Te; TX_2 represents the TMD layer and MX is a rocksalt monochalcogenide layer [333–337]. The right combination of both stacked subunits forms a superstructure and layered or even tubular morphologies can be obtained. Other complex compositions involving different metals can also be obtained in the form of single crystals, which are "ideal" heterostructures with a regular combination of different materials in a perfectly regular packed layer along the basal direction. As subunits of different compositions and repetitive patterns are obtained, electronic and physical properties can be tuned. In this sense, several studies have been published investigating the properties of this class of materials and have suggested industrial applications [333–337].

When larger single crystals of MLCs are needed, the chemical vapor transportation technique can be used to obtain millimeter- or centimeter-long single crystals. The process consists of sealing the stoichiometric amount of chemicals in the presence of iodine as a chemical transportation agent and positioning the quartz ampoule in a gradient of temperature. With these single crystals and using the same composition, even in different research groups, reproducible results can be obtained which is uncommon when results need to be reproduced from published results [333–337].

5. Optoelectronics Applications of MX_2 and MX_2-Based Composites

Semiconductor TMDCs are of special interest because it is possible to manage the gap by varying the layer composition, which is an excellent feature for the fabrication of new optoelectronic devices [342]. Despite the structure being quite similar to graphene, concerning a hexagonal lattice, TMDCs cover a wide spectrum of properties, ranging from insulators to metals. These different properties are due to the existence of the non-binding band (when the conduction band is not completely filled). It is noteworthy that one of the first articles on TMDCs was published in the mid-1980s [195]. An advantage that a TMDC model has, like MoS_2, for example, is that its bandgap varies between 1.3 eV and 1.5 eV, which was experimentally confirmed by photoluminescence absorption measurements [343]. This value is favorable for optical absorption when exposed to UV radiation (or solar light).

Research in the manufacture of optoelectronic devices based on TMDC is focused on achieving a controlled growth of samples with large grain sizes. In recent years, grains of the order of 100 μm have been reached [246,344]. After obtaining the samples, it is possible to employ microscopic observation techniques to identify the type of defects that occur, followed by grain boundary models and first-principles calculations to study the stability of the structures and the modifications introduced by the defect in the band structure, which have been observed at the grain boundaries of TMDCs [345,346]. Figure 4A–Q illustrate the main optoelectronic applications of 2D-layered TMDC materials. Using different combinations of 2D-layered materials, we can achieve innovative physical properties.

Even more interesting are the many different devices that can be built, such as capacitors, tunneling junctions, LEDs, solar cells, optoelectronic devices, and field-effect transistors.
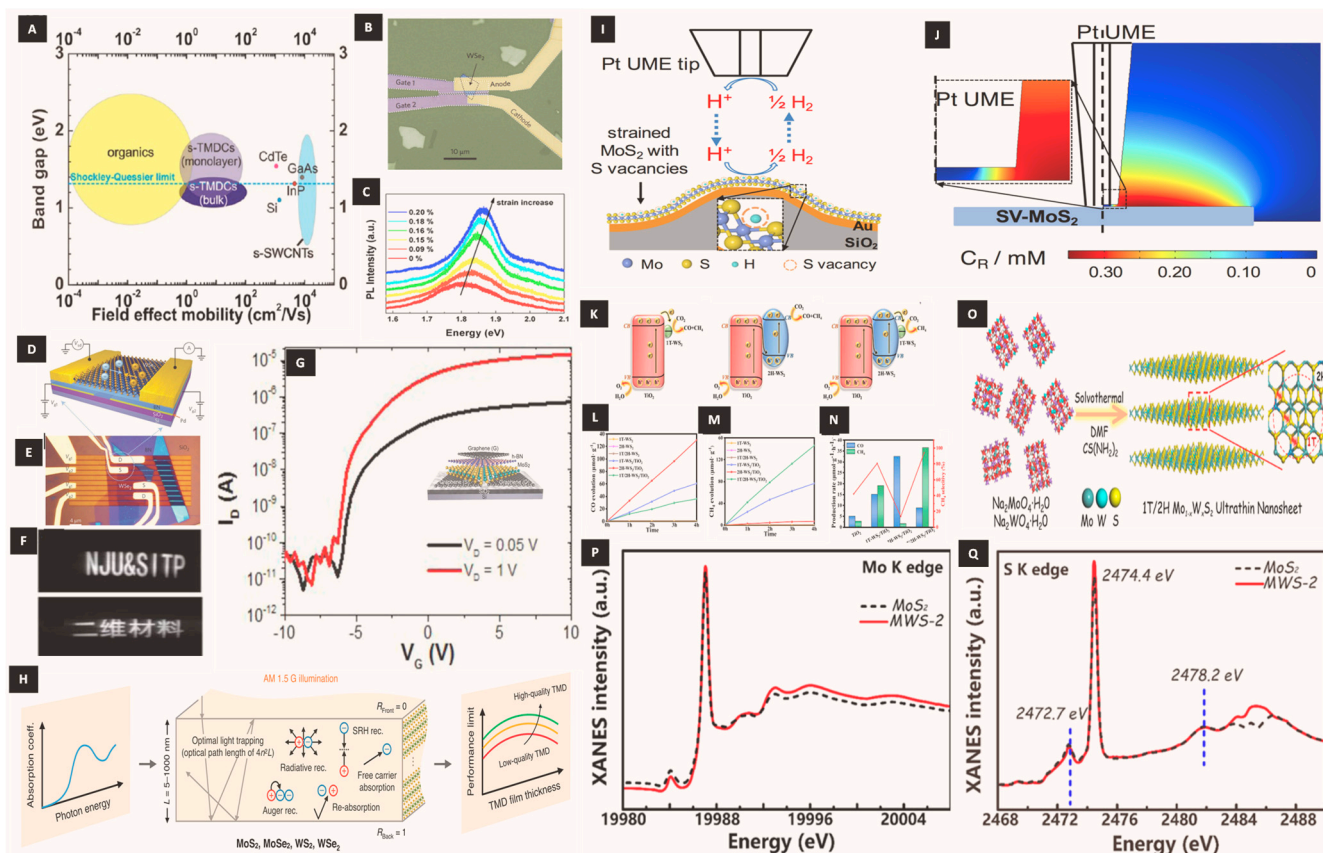

Figure 4. (**A**) Bandgap versus field-effect mobility for important semiconductors in today's high-efficiency photovoltaic devices. Reprinted with permission from Ref. [16]. Copyright 2014 American Chemical Society (**B**) A microscope image of the WSe_2 solar cell device. Reprinted with permission from Ref. [347]. Copyright 2014 Springer Nature. (**C**) PL spectra of an in-field-effect single-layer MoS_2 transistor under the variable amount of strain. Reprinted with permission from Ref. [348]. Copyright 2013 American Chemical Society. (**D**) A schematic drawing and (**E**) real microscopy of a WSe_2 stacked monolayer (2D/2D) device and source and drain contacts. Reprinted with permission from Ref. [349] Copyright 2014 Springer Nature. (**F**) Obtained images of MoS_2–graphene–WSe_2 printed objects ("NJU and SITP" and "two-dimensional material" in Chinese). Reprinted with permission from Ref. [350]. Copyright 2016 American Chemical Society. (**G**) Field-effect transistors constructed with 2D materials and their characteristics with I_{ON}/I_{OFF}. Reprinted with permission from Ref. [351]. Copyright 2014 American Chemical Society. (**H**) The schematic of a multilayer TMDC-based solar cell. Reprinted with permission from Ref. [352]. Copyright 2023 Springer Nature. (**I**) The schematic of the SECM measurement setup operating in the SG-TC mode. The top trapezoid represents a Pt UME tip, and the bottom represents a strained MoS_2 monolayer with sulfur vacancies (SV-MoS_2) serving as the working electrode. (**J**) A schematic of the complementary COMSOL simulation depicting the spatial distribution of hydrogen concentration (CR/mM). The left side illustrates the 2D configuration of the tip and substrate used in the simulation. The tip consists of a 25 μm diameter Pt wire within a glass shell (with a ratio of glass to metal radius RG = 2). The substrate, composed of strained SV-MoS_2, has a diameter of approximately 0.5 mm. The right side exhibits a representative calculated CR distribution (under the condition: SV-MoS_2 potential at −0.6 V and Pt UME tip potential at 0 V in 0.1 M $HClO_4$) [353]. A schematic representation of the proposed charge transfer mechanisms: (**K**) 1 T-WS_2/TiO_2, 2H-WS_2/TiO_2, and 1 T/2H-WS_2/TiO_2, and the time-dependent production of (**L**) CO and (**M**) CH_4 by TiO_2, 1 T-WS_2, 2H-WS_2, 1T/2H-WS_2, 1T-WS_2/TiO_2, 2H-WS_2/TiO_2, and 1 T/2H-WS_2/TiO_2. (**N**) Photocatalytic activity and photocatalytic CH_4 selectivity of the as-prepared

samples. Reprinted with permission from Ref. [354]. Copyright 2022 Elsevier. (**O**) A schematic representation of the synthesis process of ultrafine $Mo_{1-x}W_xS_2$ nanosheets; (**P**) the Mo and (**Q**) S K-edge XANES spectrum of MWS-2 and MoS_2. Reprinted with permission from Ref. [355] Copyright 2021 American Chemical Society.

5.1. Transistors

Radisavljevic et al. [36] were able to successfully produce a transistor composed of a 2H-MoS_2 single layer. Since then, TMDCs have been considered very promising for use in 2D vdW heterostructures. For example, the semiconductor/semiconductor vdW heterojunction is composed of layers of $MoSe_2/WSe_2$ [356] and MoS_2/WS_2 [29]. It is thus possible to control electronic properties of interest, such as the energy gap, through an adequate choice of the number and type of stacked 2D materials. This is of great interest to the engineering development of new semiconductor materials.

A charge transfer accompanies the formation of a heterostructure between the materials used. The meaning of this transfer is important for describing the electronic properties of the system. This sense can be obtained through the alignment of bands (band offsets). Based on first-principles calculations, Kang and collaborators performed an extensive study of the band alignment of TMDCs comparing the ionization potential which is the minimum energy to take an electron from the last VB, and the energy gap of the stacked 2D components [62]. Thus, they show that the $MoSe_2/WSe_2$, MoS_2/WS_2, and MoS_2/WSe_2 heterojunctions show type II band alignment. In fact, this type II alignment was verified in a recent experimental realization of the p-n MoS_2/WSe_2 heterojunction [310].

Combining metal/semiconductor in heterostructures has also been successfully synthesized using 2D (semi)metal over layers of TMDCs, for example, graphene on TMDCs [357,358], or 2D metals, 2H-NbS_2 type, on TMDCs semiconductors [63]. In this type of heterostructure, it is essential to consider the height of the Schottky barrier (ΦB). In general, ΦB can be estimated by comparing the metal work function (Wm) and the electron affinity (ΦB for n-type semiconductors) or the ionization potential (ΦB for p-type semiconductors) of the semiconductor. Like what happens in 3D structures, the height of the Schottky barrier can be adjusted by an external electric field, as seen in FETs. However, the injection of holes in FETs based on TMDC (semiconductors) was limited by the larger values of p-type ΦB. There are some proposals aiming to provide better efficiency in the injection of holes in TMDCs, for example, by using oxidized graphene at source/drain contacts [359,360], and the inclusion of a monolayer of boron nitride BN at the metal/semiconductor interface [361]. On the other hand, the control of p-type ΦB, to obtain an efficient injection of holes in the metal/TMDCs heterojunctions, remains a challenge. Therefore, we are facing intense research on new materials, which allows us to make a series of combinations of materials to obtain a certain electronic property. Lee et al. [360] detailed the production of phototransistors employing 2D MoS_2, with graphene as a source and drain electrodes. It was shown a photoresponse within the 400–700 nm range, boasting an impressive responsivity value of 1×10^4 A/W. In addition to its versatility in more advanced optoelectronic applications, the authors have shown the MoS_2 photoinverter being used as imaging pixels, leading to the fabrication of a prototype visible imager effectively operating under a green light [362].

5.2. Photodetectors

PN junction photodetectors operate in two primary modes: photoconductive mode, where an external bias voltage enhances light sensitivity, and photovoltaic mode, which generates a voltage upon illumination without an external bias. Thus, when a photon with energy greater than the bandgap of the material hits the surface, an electron–hole pair is created, which, when ejected from the material, generates an electric current. The band alignment conditions present in TMDCs allow them to be applied as photodetectors [363,364]. The bandgap potential of 2D-layered TMDC materials ranges from 0 eV found for graphene to ~6 eV for hBN [365].

Specifically, there are photodetectors based on homojunction, which offer three methods for modulating the carrier type of TMDCs: altering surface properties through chemical treatment, modifying single-crystalline TMDC properties via elemental doping, and carrier modulation through electrostatic gating, excluding doping [366]. Additionally, heterojunctions formed at the interface between two dissimilar materials with unequal bandgaps are usually utilized in TMDC-based photodetectors [366].

Although presenting appropriate and, in some cases, tunable bandgap electronic structures, the photodetectors based on TMDC materials suffer from long photoresponse time, low visible light absorption capacity, and low carrier mobility [365]. Pulikodan et al. [367] conducted an analysis of the underlying factors contributing to the anomalous transient photocurrent phenomena observed in self-powered photodetectors constructed from solution-processed WS_2 nanosheet. They demonstrated a high on/off ratio of about 2.4×10^5 under illumination from an LED with a wavelength of about 625 nm and an intensity of 100 mW/cm^2. The device exhibits peaks in photoresponsivity at wavelengths of approximately 630 nm and 523 nm, which in turn correspond to the absorption peaks observed for the WS_2 nanosheets. This behavior is partly attributed to the modification of WS_2 electronic bands at the interface due to defect states present on the surface of nanosheets, including sulfur vacancy defects [367].

One strategy to face these issues was described by Li et al. [368] with a photodetector composed of a sandwich Au-MoS_2-Au structure, in which the authors claimed a high light response speed due to an enhanced local surface plasmon resonance coupling between the double-layered Au modifications. The combination of few-layer MoS_2 and PbS quantum dots (QDs), in a hybrid nanostructure form, was described as a strategy to improve the performance of the MoS_2-based photodetector. The formation of vertically-few-layer MoS_2 promoted a large specific surface area and improved light absorption capacity, while the QD expanded the response range from visible light to near-infrared [301]. The strategy of preparing a MoS_2-based photodetector using a graphene fiber type is an option to obtain better performance since this structure presents a relatively larger surface area in comparison with sheet-type devices [369].

Maity et al. [370] published a study on MoS_2/$MoSe_2$ nanoflakes deposited on gallium nitride (GaN) substrates for photodetection. Besides investigating each material individually, the study included an analysis of the deposition order of MoS_2 and $MoSe_2$ layers on the GaN substrate. The experimental results demonstrate that the photodetectors, designed by depositing MoS_2 on the $MoSe_2$ layer previously grown on the GaN substrate, exhibited superior performance in photodetection. The main measurements demonstrated a high photoresponsivity of 82 A/W, a specific detectivity of 1.791×10^{14} Jones, and an external quantum efficiency of around 28%. Based on the theoretical calculations performed by these authors, the superior performance of this heterostructure in the vertical configuration (GaN/$MoSe_2$/MoS_2) is related to the two consecutive staggered type II band alignments. In this case, the electron transport from MoS_2 to $MoSe_2$ is facilitated by the inherent potential at the junction, allowing it to overcome the developed potential barrier and reach GaN. On the other hand, the holes can be transported from GaN to $MoSe_2$ and subsequently from $MoSe_2$ to MoS_2 without any potential barrier.

Wu et al. [371] developed MoS_2 photodetectors by coupling semi-metallic WO_{3-x} nanoparticles underneath for ultrafast and near-infrared spectrum detection. The photodetection performance (1.8×10^4 A/W) was 100 times higher than pure MoS_2. Hence, the high performance of this photodetector can in principle be attributed to the synergistic effect of both the semi-metallic nature of the lower WO_{3-x} nanoparticles and the intact nature of the upper MoS_2 layer [371].

5.3. Solar Cells

The use of TMDCs in photovoltaic cells is one of the possible applications using a PN junction. Based on Shockley–Quessier calculations [372], a bandgap close to 1.3 eV would be desired to obtain a good photovoltaic efficiency [16]. On the other hand, TMDC-based

solar cells do not have the stability issues of organic photovoltaics or perovskites, although they are not yet comparable in terms of efficiency [373]. In addition to the wide range of bands and possible combinations, TMDCs also have good field-effect mobility values, as seen in Figure 4A. However, the bandgap condition is only satisfied when these materials are in the order of monolayers. Figure 4B shows an optical microscopy showing a solar cell constructed from superimposed layers based on WSe_2.

Several studies have been conducted [347,374] testing different combinations of TMDCs. For the stacking of MoS_2 single layers, a maximum energy conversion efficiency (PCE) of ~1% was obtained, while the heterojunction between WS_2/MoS_2 was 1.5% [117]. The TMDC heterostructures such as CuS/WS_2 and CuS/MoS_2 are also found as an alternative material for Pt employed as a counter electrode in dye-sensitized solar cells, resulting in a system that exhibited a PCE of 8.21% and 7.12%, respectively [375].

Nazif et al. [352] achieved groundbreaking results with flexible TMDC solar cells, achieving a record PCE of about 5.1% and a record specific power of 4.4 W g^{-1} using multilayer (~200 nm) WSe_2 absorbers. In another study, the efficiency limits of multilayer TMDC solar cells, including MoS_2, $MoSe_2$, WS_2, and WSe_2, were investigated as a function of thickness and material quality [352]. They looked beyond existing models (as Tiedje Yablonovitch and Shockley–Queisser) to include real-world measurements of light absorption and different ways the solar cell could lose efficiency (Figure 4H). Their results suggest that these ultrathin solar cells, as thin as 50 nanometers, could achieve up to 25% efficiency even with current material quality [352].

Although the solar cells produced using TMDCs have shown promising results, the limitation of absorption [16] due to the thickness of the packed layers (in the order of nanometers) makes these devices have low PCE values when compared to crystalline silicon cells, multijunction devices cells, thin films, perovskite cells [376] and dye-sensitized solar cells [377]. In the attempt to increase light capture and minimize this low conversion limitation, efforts have been made to use plasmon absorption [378,379], for example, through higher layer stacking [380] and increased strain [381] (see Figure 4C).

5.4. Light-Emitting Diodes (LEDs)

TMDCs are generally n-type semiconductors, but by introducing a dopant with p-type characteristics, these materials have applicability as LEDs [365]. Among TMDCs, $2H-WSe_2$ is often used as a p-type element together with good conductive metals such as Pt, Pd [382], and Au [383]. For instance, Najafidehaghani et al. [384] produced lateral $MoSe_2/WSe_2$ heterostructures grown by a one-pot CVD process. The photoluminescence at room temperature was analyzed using a laser with an excitation wavelength of 532 nm. For this particular heterostructure, the PL intensity from *p*-type WSe_2 was on average 10 times higher than that of *n*-type $MoSe_2$. The maximum emission peaks were detected at 790 nm (1.568 eV) and 748 nm (1.656 eV) for $MoSe_2$ and WSe_2, respectively. The synergic emission detected in the PL spectrum was attributed to the presence of well-separated areas in the laterally oriented heterostructure. The physicochemical features of these distinct areas are equivalent to those exhibited in the individual materials when grown separately. By employing various electronic and optoelectronic measurements, the authors proved its effectiveness.

Figure 4D,E show the assemblies of two devices made from the combination of layers of 2D TMDCs. In Figure 4D,E, we see an LED device capable of varying the intensity of the current, oscillating the intensity of the emitted light [349]. In Figure 4F, devices capable of being printed with good resolution and contrast are shown, and it is even possible to inscribe perfectly legible letters, opening up many possibilities for their application [350]. The stacking of these layers provides these devices with unique properties, which, as discussed in Section 4, confers properties that would not be possible without the combination of different materials.

The use of these 2D materials in vdW structures not only offers unique properties but can also extend conventional electronics applications to other branches, such as flexible and

transparent electronics [115]. Considering the excellent optical and mechanical properties of MoS_2 (semiconductor), h-BN (dielectric), and graphene (conductor), these materials can be stacked in a metal–oxide–semiconductor (MOS) structure, which is the heart of transistors like the metal–oxide–semiconductor field-effect transistors type.

Field-effect transistors using 2D materials stacked with all components, including the semiconductor, insulator, and metal layers, have been demonstrated [351] (see Figure 4G). Specifically, MoS_2 was used as the active channel material (semiconductor), h-BN as the dielectric, and graphene as the source and drain and gate electrode contacts. This transistor exhibited n-type behavior with an I_{ON}/I_{OFF} current ratio of $>10^6$ and electron mobility of ~33 cm^2 $V^{-1}s^{-1}$. Furthermore, mobility did not degrade with high voltages at the gate electrode, presenting an important advantage over conventional Si transistors, where surface roughness scattering severely reduces the mobility of charge carriers [351].

The thermal stability of a two-dimensional material is also a very important criterion for future applications, as the heating of devices through current flow and other adverse environmental conditions is generally unavoidable. It was observed that the MoS_2 monolayer has a lower thermal stability than its 3D analog, and its degradation temperature drops to 700 °C in a high vacuum when it is grown on SiO_2 [385]. Regarding large-scale synthesis, controlling the thermal stability of MoS_2 is essential to allow its integration with other 2D materials, such as hexagonal boron nitride (h-BN). Due to its wide bandgap, h-BN has emerged as a promising 2D material to be used as a dielectric layer in nanoelectronic devices with MoS_2 [386]. In addition, the h-BN/MoS_2 junction becomes an advantageous heterostructure because, among 2D materials, h-BN is one of the most resistant to oxidation [387], which could act as a protective layer for sensors based on MoS_2, mitigating the degradation caused by surface contamination [388]. It has also been seen that using one or two layers of h-BN as a tunneling layer can considerably reduce the Schottky barrier in MoS_2-based devices using h-BN/MoS_2 instead of just MoS_2 in contact with the metal [389]. However, for the application of h-BN in these devices, it is necessary to use large-area growth techniques that generate low defect density, such as MBE [390]. MoS_2 must be stable under these conditions because the growth of h-BN by MBE requires relatively high temperatures (>600 °C) [261].

Daus et al. [391] successfully fabricated flexible transistors utilizing single-layer MoS_2 and achieved impressive currents reaching nearly 470 microamps per micrometer at a drain-source voltage of 1 volt. The authors conducted a performance comparison with flexible graphene and crystalline silicon FETs. These transistors featured channel lengths of less than 100 nanometers and were fabricated by transferring the MoS_2 material and pre-defined metal contacts onto flexible substrates [391].

5.5. Photocatalytic Activity

Since the Industrial Revolution, fossil fuels have been essential for the development of society. However, with technological advancements and the change in society's lifestyle, there are predictions of energy consumption of about 25–27 TW until 2050 [392]. This represents more than 80% of the energy available from the remaining fossil fuel reserves. Associating this energy demand with the large volume of greenhouse gases released into the atmosphere and their impacts on the climate, there is an increasing need for the development of technologies to generate cleaner and renewable energy. Within this context are photocatalytic processes such as the water splitting process for hydrogen generation and the CO_2 photoreduction process, which can provide raw materials for industry [393].

Therefore, the search for suitable photocatalysts with broad solar absorption and efficient separation of charge carriers has become one of the most important tasks for the implementation of these technologies.

5.5.1. CO_2 Photoreduction

Photocatalysts based on transition metal chalcogenides are being widely explored owing to their excellent mechanical, thermal, electrical, and optical properties. However,

although TMDCs are used for the adsorption and photoreduction of CO_2, their use is still very low due to limited photoabsorption in the visible region and the positions of the VB and CB, which leads to rapid recombination of electrons/holes photogenerated [394]. Thus, different research groups are using some TMDCs modification strategies, such as heterostructures formation and TMDCs stacking, to improve visible light absorption and promote efficient electron–hole separation, along with adequate charge transport to the surface [395,396].

Meier et al. [397] analyzed the influence of the controlled introduction of crystalline defects and the thickness of the flake through variations in CVD synthesis to obtain nanoflowers of MoS_2 and demonstrated the tunable nature of flake edge morphology, nanoflower size, stacked-sheet thickness, and optical bandgap energy (E_g), as well as the impact of these variables on photocatalytic activity. These modifications facilitated the tuning of the E_g from 1.38 to 1.83 eV and induced the manifestation of the 3R phase, resulting in enhanced photocatalytic performance. During photoreduction tests, the ideal characteristics of the materials were observed in samples exhibiting high nanoflower density as well as thick-edge site abundance. In this way, the authors showed a facile synthesis method yielding controllable nanoflower formations, showing repeatability and providing insights into synthetic parameters for the regulation of defect-laden, well-defined edge-site-rich and photocatalytically active systems in the CO_2 photoreduction [397].

Zhou et al. [354] showed that WS_2 (1T-WS_2 and 2H-WS_2) is thermodynamically stable and suitable for forming heterojunctions with other semiconductors for use in the CO_2 photoreduction process. The authors designed and constructed a novel heterojunction photocatalyst (Figure 4K) by integrating multiphase 1 T/2H-WS_2 homojunction combined with TiO_2. This configuration ensured a cascading, multi-step transfer path of photogenerated electrons, which facilitated charge separation and electron accumulation in 1T-WS_2, which served as a co-catalyst for the photocatalytic reduction of CO_2, showing an improvement in both activity and selectivity (94.2%) when compared to TiO_2 (41.9%) in the conversion of CO_2 to CH_4 [354].

5.5.2. Hydrogen Evolution

In addition to the incessant search for the development of technologies for the abatement of CO_2, the growing demand for clean renewable energies has attracted more and more focus, mainly on hydrogen (H_2) generation processes, such as the water splitting process via electrocatalytic, catalytic, and photoelectrocatalytic processes [398,399]. Hence, there is a strategic interest in finding multifunctional materials with superior performance for their production.

The catalytic and photocatalytic properties of 2D-TMDCs for hydrogen evolution are promising and have gained significant interest due to their narrow bandgap, the atomically thin nature of 2D-TMDCs, which leaves the catalytically active sites more exposed, and their metallic nature, which leads to greater electrical conductivity, and which is more favorable to hydrogen evolution reactions [400,401].

In 2007, Jaramillo et al. [105] identified the active site responsible for H_2 evolution in a reaction catalyzed by nanoparticulate MoS_2 on Au(111). In their study, Li et al. [353] applied the combined approach of scanning electrochemical microscopy measurements and multiphysics modeling (Figure 4I,J) to delve into the HER kinetics of newly discovered active sites consisting of S-vacancies situated on the basal plane of MoS_2. The authors show that tensile elastic strain enhances the HER kinetics owing to the presence of S-vacancies in MoS_2.

Using DFT calculations, Tsai and his co-workers [402] investigated the activity and stability of 26 different TMDC catalysts for the HER. Their findings revealed a strong correlation between HER activity and catalyst stability, in which systematic enhancements in activity are significantly constrained by a decrease in stability [403]. However, at the edges, the relationships between activity and stability remain consistent regardless of

the structure or chalcogen. This suggests that it is possible to achieve optimal hydrogen bonding with a stable surface.

In general, both vertical and horizontal heterostructures have presented exceptional performance for different technological purposes. In the scope of this context, Vikraman et al. [404] investigated the effectiveness of MoS_2/WS_2 heterostructures, grown on fluorine-doped tin oxide-covered glass substrates, as an electrocatalyst for HER. These films were obtained by using a combination of chemical bath deposition and radio frequency sputtering techniques, which yield a surface consisting of a cauliflower-structured array of grains with spherical structures without the presence of pinholes or cracks. Both the vertical orientation of MoS_2/WS_2 heterostructures and their morphological aspects resulted in a high catalytic performance for HER. The electrochemical data confirmed an overpotential of about 129 mV at 10 mA/cm^{-2}, a high exchange current density of 4.36×10^{-1} mA/cm^2, and a small Tafel slope of 72 mV/decade. Another key aspect to highlight was the prolonged stability exhibited by the heterostructured electrodes, which remained functional even after 20 h of uninterrupted H_2 production [404]. Lin et al. [405] reported the formation of an atomic double-layer heterostructured photocatalyst formed by WS_2 and Nb_2O_5 (WS_2/Nb_2O_5) and found that the average lifetime of charge carriers for WS_2/Nb_2O_5 (~180.97 ps) is considerably reduced compared to that of pure Nb_2O_5 (~230.50 ps). This substantial reduction strongly suggests that the shell/core interface allows the WS_2/Nb_2O_5 to achieve an ultra-fast charge transfer from Nb_2O_5 to the atomic double-layer WS_2. Consequently, this photocatalyst exhibited a remarkable H_2 evolution rate of about 237.6 mmol/h, which is 10.8 times higher than that of pure Nb_2O_5 nanosheets.

Huang et al. [406] described the photocatalytic performance for H_2 production of WS_2 nanoflakes grown on g-C_3N_4 by a simple colloidal route. This synthetic approach was able to promote the coexistence of both 1T (metallic) and 2H (semiconducting) phases in WS_2. However, the authors explained that the presence of the 1T phase served as a co-catalyst, playing a key role in enhancing the electronic conductivity and providing additional active sites for H^+ reduction over both basal and edge sites. Other advantageous aspects responsible for enhanced H_2 production (350.75 μmolg^{-1}h^{-1}) were the suitable positioning of energy levels and the layered vertical connecting structures of g-C_3N_4/WS_2.

Geng et al. [407] present a novel approach to enhance the HER of MoS_2 by activating interfacial sulfur sites through the integration of ruthenium (Ru) nanoparticles onto the inert basal plane of MoS_2 nanosheets. Both DFT calculations and experimental findings confirm the modulation of the interfacial S electronic structure and optimized hydrogen adsorption on MoS_2. Notably, the Ru-MoS_2 catalyst exhibits remarkable performance, requiring only overpotentials of 110 mV and 98 mV to achieve a current density of 10 mA·cm^{-2} in 0.5 M H_2SO_4 and 1 M KOH solutions, respectively. This innovative strategy opens avenues for activating the basal plane of other TMDC electrocatalysts, promising significant advancements in HER performance.

Lu et al. [408] studied a vacuum thermal evaporation system designed for production in large quantities of uniform polycrystalline MoS_2 thin films. Leveraging K_2MoS_4 as the precursor, this system enables a reliable deposition of high-quality MoS_2 films with controllable thickness (0.8 to 2.4 nm) and dimensions up to 50 mm × 50 mm. This method facilitates patterned deposition of MoS_2 through the use of shadow masks and sequential deposition of MoS_2 and WS_2, akin to conventional thermal evaporation techniques.

5.5.3. N_2 Reduction Reaction

In the context of the N_2 reduction reaction (N_2RR), certain transition metals such as Mo display a pivotal role in enhancing the bonding interaction between N_2 and the catalyst surface due to their unique d orbital configuration [409–411]. The use of DFT calculations in theoretical investigations has identified Mo and Fe as highly promising candidates for NH_3 synthesis through associative mechanisms [412]. Experimental studies conducted by Zhao and colleagues support the thermodynamic perspective by revealing that the initial hydrogenation step of N_2 spontaneously and preferentially occurs on the Mo(111)

surface [413]. The particular presence of the Mo and S elements in nitrogenases has drawn attention to their catalytic activity in N_2RR [409]. Inspired by the enzymatic studies of natural NH_3 synthesis, there has been a growing interest in TMDC sulfides like MoS_2 [414] owing to their large structural similarity to the active site of nitrogenases [415].

Computational studies have also suggested the possibility of NH_3 electrosynthesis occurring on sites where Mo atoms are exposed to the electrolyte, further supporting the plausibility in mechanistic terms [416]. Building upon this knowledge, Zhang et al. [417] successfully prepared MoS_2 nanosheets through hydrothermal methods on carbon cloth and utilized them as catalysts for NH_3 electrosynthesis under ambient conditions, achieving notable results with a faradaic efficiency of about 1.17% and an NH_3 yield of 8.08×10^{-11} mol s^{-1} cm^{-2} at -0.5 V vs. RHE in 0.1 M Na_2SO_4 [417].

Research based on DFT also indicates that the efficiency of MoS_2 catalysts in NH_3 synthesis can be enhanced through the introduction of defects and additional elements into their structure [416]. This improvement is attributed to the catalyst's high selectivity for N_2 on its surface [418]. In this sense, the doping of the MoS_2 microsphere surface with nitrogen (N-MoS_2) performed in situ by a hydrothermal method improved N_2 fixation ability (101.2 μ mol/g(cat)h) compared to MoS_2 undoped under the visible light irradiation, once the presence of nitrogen reduces the bandgap, while the hierarchical surface structure enhances light adsorption by promoting reflection and scattering effects [419]. The controlled W-doping of MoS_2 (Figure 4O), in a controlled ratio of a 2H-to-1T phase ($Mo_{1-x}W_xS_2$), results in an increased electron density state within the W 5d orbitals, enabling the polarization of adsorbed N_2 molecules (Figure 4P,Q), and facilitating their adsorption, activation and, consequently, leading to improved NH_3 formation yield compared to pristine MoS_2 or WS_2 [355].

Another strategy to boost the NH_3 synthesis using MX_2-based composites is utilizing heterostructure design in interface engineering; it presents a viable method for enhancing the kinetics of N_2RR and elevating catalytic performance. This approach leverages the robust interfacial interactions between two material catalysts, enhancing not only electron transfer but also optimizing the free energies for the intermediates of the reaction [420]. DFT studies offer additional insights, revealing that the heterostructure strategy reduces the energy barrier for stabilizing intermediates and promotes favorable H adsorption on sulfur (S) edge sites of MoS_2, resulting in high faradaic efficiency [421]. In this sense, the combination of MX_2 with other 2D semiconductors has been investigated for the photochemical generation of NH_3, as in the case of the hybrid $MoSe_2@g$-C_3N_4 [422] and p-MoS_2/n-$MgIn_2S_4$ marigold flower-like heterojunction composites [423] where improving the rate of NH_3 production has been a good strategy to promote photochemical N_2RR.

5.6. Electrocatalytic Activity

Electrocatalysis using 2D-layered materials such as MX_2 has been an area of intense research owing to their unique properties that are beneficial for electrochemical reactions. In particular, the 1T phase of TMDCs, like MoS_2, has shown great promise due to its electronic structure that facilitates electron transfer and reactant activation. For instance, theoretical/experimental investigations have demonstrated that 1T-MoS_2 exhibits high efficacy in the HER (which is discussed in detail in Section 5.5.2), one of the most fundamental electrocatalytic reactions.

Xue et al. [424] reported the synthesis of heterostructures formed from 2D-1T′-MoS_2 with g-C_3N_4 with nanocage structures. Additionally, the inclusion of the co-catalyst 1T′-MoS_2 effectively suppresses photoinduced carrier recombination. Consequently, the 1T′-MoS_2/g-C_3N_4 heterostructure exhibits excellent cycle stability and has a hydrogen evolution rate of 1949 molh^{-1}, surpassing that of g-C_3N_4 nanocage structures by 162.4 times (12 molh^{-1}) [424]. Compared to both pristine g-C_3N_4 nanocage and g-C_3N_4 nanosheets, DFT calculations and experimental analyses show that the 1T′-MoS_2/g-C_3N_4 heterostructure exhibits significantly enhanced light-absorption capability and possesses a larger specific surface area [110].

Another important application of electrocatalysis with MX_2 is in the oxygen reduction reaction (ORR), which is crucial for energy conversion devices like fuel cells [425,426]. The 1T-MoS_2 phase, with its high electronic state density and metallic properties, offers an efficient active site for ORR [427]. The ability to adjust the composition and phase of MoS_2 through doping or thermal treatments paves the way for developing tailor-made catalysts with enhanced electrocatalytic activity [428].

Moreover, electrocatalysis using MX_2 is not limited to HER and ORR. The 1T-MoS_2 phase has also been explored for other electrocatalytic reactions, such as the oxygen evolution reaction (OER) [426,429–431] and the carbon dioxide reduction reaction (CO_2RR) [432,433]. A recent study [434] highlighted that the 1T-MoS_2 phase exhibits superior OER activity when compared to the semiconducting 2H phase, owing to its higher conductivity and increased abundance of active sites.

In summary, the 1T-MoS_2 phase and other MX_2 materials offer a versatile platform for electrocatalysis, with the potential to revolutionize clean and sustainable energy production. Ongoing research in the synthesis and functionalization of these 2D-layered materials based on TMDCs will continue to unveil new avenues for designing advanced electrochemical catalysts.

6. Perspective and Outlook

TMDCs have attracted the scientific community's attention due to their diversity of dimensionalities, offering a wide array of optical, electronic, and mechanical properties with vast application potential. Their 2D structures provide significant surface area, allowing for effective interaction with various compounds. Furthermore, the ability of TMDCs to modulate their electronic and chemical properties through the control of composition and morphology opens new possibilities for the rational design of highly efficient and selective catalysts. As highlighted in this review, TMDC-based materials have the potential to catalyze a wide range of reactions, including CO_2 photoreduction, water splitting, and N_2 reduction, among others. However, the translation of this knowledge into practical technologies faces significant challenges, particularly in the scalable fabrication of vdW heterostructures and the detailed understanding of reaction mechanisms at the molecular level. Therefore, the fabrication of devices based on these structures still needs to be revised, and scalable and reproducible preparation procedures must be developed. On the other hand, as with other challenges humanity faces, if a goal attracts enough interest, researchers worldwide will test different approaches, and eventually, this creative process will find its way. Furthermore, exploring the potential of layered TMDCs in quantum information processing, spintronics, and optoelectronic technologies holds promise for future technological advancements. Novel phenomena such as superconductivity and topological insulating behavior further underscore the transformative potential of TMDC-based technologies across various industries. In summary, while there has been significant research on a few select TMDCs, several others have also shown promise for a range of applications in optoelectronics, photo(electro)catalysis, and beyond [435–451]. Further research on these materials, extended to thousands of natural and synthetic layered materials, will help uncover their full potential and enable the emergence of new technologies in the future, contributing to more efficient and sustainable solutions to global challenges.

Author Contributions: Conceptualization, F.M.P., M.C.M.D.d.C., W.S.P., J.C.S., M.M., P.G.C., J.F.d.B., A.E.N., M.S.G., O.P.F., L.H.M., F.W. and F.A.L.P.; formal analysis, F.M.P., M.C.M.D.d.C., W.S.P., J.C.S., M.M., P.G.C., J.F.d.B., A.E.N., M.S.G., O.P.F., L.H.M., F.W. and F.A.L.P.; investigation, F.M.P., M.C.M.D.d.C., W.S.P., J.C.S., M.M., P.G.C., J.F.d.B., A.E.N., M.S.G., O.P.F., L.H.M., F.W. and F.A.L.P.; resources, F.M.P., M.C.M.D.d.C., W.S.P., J.C.S., M.M., P.G.C., J.F.d.B., A.E.N., M.S.G., O.P.F., L.H.M., F.W. and F.A.L.P.; data curation, F.M.P., M.C.M.D.d.C., W.S.P., J.C.S., M.M., P.G.C., J.F.d.B., A.E.N., M.S.G., O.P.F., L.H.M., F.W. and F.A.L.P.; writing—original draft preparation, F.M.P., M.C.M.D.d.C., W.S.P., J.C.S., M.M., P.G.C., J.F.d.B., A.E.N., M.S.G., O.P.F., L.H.M., F.W. and F.A.L.P.; writing—review and editing, F.M.P., M.C.M.D.d.C., W.S.P., J.C.S., M.M., P.G.C., J.F.d.B., A.E.N., M.S.G., O.P.F., L.H.M., F.W. and F.A.L.P. All authors have read and agreed to the published version of the manuscript.

Data Availability Statement: Not applicable.

Conflicts of Interest: The authors declare no conflicts of interest.

References

1. Singh, J. *Electronic and Optoelectronic Properties of Semiconductor Structures*; Cambridge University Press: Cambridge, UK, 2007; ISBN 1139440578.
2. Longo, E.; La Porta, F.d.A. *Recent Advances in Complex Functional Materials: From Design to Application*; Springer International Publishing: Berlin/Heidelberg, Germany, 2017; ISBN 9783319538983.
3. De La Porta, F.A.; Taft, C.A. *Emerging Research in Science and Engineering Based on Advanced Experimental and Computational Strategies*; Engineering Materials; de La Porta, F.A., Taft, C.A., Eds.; Springer International Publishing: Cham, Switzerland, 2020; ISBN 978-3-030-31402-6.
4. De Brito, J.F.; Corradini, P.G.; Silva, A.B.; Mascaro, L.H. Reduction of CO_2 by Photoelectrochemical Process Using Non-Oxide Two-Dimensional Nanomaterials—A Review. *ChemElectroChem* **2021**, *8*, 4305–4320. [CrossRef]
5. Zhao, Y.; Waterhouse, G.I.N.; Chen, G.; Xiong, X.; Wu, L.-Z.; Tung, C.-H.; Zhang, T. Two-Dimensional-Related Catalytic Materials for Solar-Driven Conversion of CO_x into Valuable Chemical Feedstocks. *Chem. Soc. Rev.* **2019**, *48*, 1972–2010. [CrossRef] [PubMed]
6. He, J.; Tao, L.; Zhang, H.; Zhou, B.; Li, J. Emerging 2D Materials beyond Graphene for Ultrashort Pulse Generation in Fiber Lasers. *Nanoscale* **2019**, *11*, 2577–2593. [CrossRef] [PubMed]
7. Novoselov, K.S.; Geim, A.K.; Morozov, S.V.; Jiang, D.; Zhang, Y.; Dubonos, S.V.; Grigorieva, I.V.; Firsov, A.A. Electric Field in Atomically Thin Carbon Films. *Science* **2004**, *306*, 666–669. [CrossRef] [PubMed]
8. Geim, A.K.; Novoselov, K.S. The Rise of Graphene. *Nat. Mater.* **2007**, *6*, 183–191. [CrossRef] [PubMed]
9. Nair, R.R.; Ren, W.; Jalil, R.; Riaz, I.; Kravets, V.G.; Britnell, L.; Blake, P.; Schedin, F.; Mayorov, A.S.; Yuan, S.; et al. Fluorographene: A Two-Dimensional Counterpart of Teflon. *Small* **2010**, *6*, 2877–2884. [CrossRef] [PubMed]
10. Zeng, Y.; Guo, Z. Synthesis and Stabilization of Black Phosphorus and Phosphorene: Recent Progress and Perspectives. *iScience* **2021**, *24*, 103116. [CrossRef] [PubMed]
11. Yi, Y.; Yu, X.F.; Zhou, W.; Wang, J.; Chu, P.K. Two-Dimensional Black Phosphorus: Synthesis, Modification, Properties, and Applications. *Mater. Sci. Eng. R Rep.* **2017**, *120*, 1–33. [CrossRef]
12. Dimoulas, A. Silicene and Germanene: Silicon and Germanium in the "Flatland". *Microelectron. Eng.* **2015**, *131*, 68–78. [CrossRef]
13. Wang, G.; Pandey, R.; Karna, S.P. Physics and Chemistry of Oxidation of Two-Dimensional Nanomaterials by Molecular Oxygen. *Wiley Interdiscip. Rev. Comput. Mol. Sci.* **2017**, *7*, e1280. [CrossRef]
14. Osada, M.; Sasaki, T. Two-Dimensional Dielectric Nanosheets: Novel Nanoelectronics from Nanocrystal Building Blocks. *Adv. Mater.* **2012**, *24*, 210–228. [CrossRef] [PubMed]
15. Butler, S.Z.; Hollen, S.M.; Cao, L.; Cui, Y.; Gupta, J.A.; Gutiérrez, H.R.; Heinz, T.F.; Hong, S.S.; Huang, J.; Ismach, A.F.; et al. Progress, Challenges, and Opportunities in Two-Dimensional Materials beyond Graphene. *ACS Nano* **2013**, *7*, 2898–2926. [CrossRef] [PubMed]
16. Jariwala, D.; Sangwan, V.K.; Lauhon, L.J.; Marks, T.J.; Hersam, M.C. Emerging Device Applications for Semiconducting Two-Dimensional Transition Metal Dichalcogenides. *ACS Nano* **2014**, *8*, 1102–1120. [CrossRef] [PubMed]
17. Meng, S.; Zhang, Y.; Wang, H.; Wang, L.; Kong, T.; Zhang, H.; Meng, S. Recent Advances on TMDCs for Medical Diagnosis. *Biomaterials* **2021**, *269*, 120471. [CrossRef] [PubMed]
18. He, Z.; Xu, W.; Zhou, Y.; Wang, X.; Sheng, Y.; Rong, Y.; Guo, S.; Zhang, J.; Smith, J.M.; Warner, J.H. Biexciton Formation in Bilayer Tungsten Disulfide. *ACS Nano* **2016**, *10*, 2176–2183. [CrossRef] [PubMed]
19. Manzeli, S.; Ovchinnikov, D.; Pasquier, D.; Yazyev, O.V.; Kis, A. 2D Transition Metal Dichalcogenides. *Nat. Rev. Mater.* **2017**, *2*, 17033. [CrossRef]
20. Gibney, E. The Super Materials That Could Trump Graphene. *Nature* **2015**, *522*, 274–276. [CrossRef] [PubMed]
21. Xu, H.; Xue, Y.; Liu, Z.; Tang, Q.; Wang, T.; Gao, X.; Qi, Y.; Chen, Y.P.; Ma, C.; Jiang, Y. Van Der Waals Heterostructures for Photoelectric, Memory, and Neural Network Applications. *Small Sci.* **2024**, *4*, 2300213. [CrossRef]
22. Liu, F. Mechanical Exfoliation of Large Area 2D Materials from VdW Crystals. *Prog. Surf. Sci.* **2021**, *96*, 100626. [CrossRef]
23. Busch, R.T.; Sun, L.; Austin, D.; Jiang, J.; Miesle, P.; Susner, M.A.; Conner, B.S.; Jawaid, A.; Becks, S.T.; Mahalingam, K.; et al. Exfoliation Procedure-Dependent Optical Properties of Solution Deposited MoS_2 Films. *npj 2D Mater. Appl.* **2023**, *7*, 12. [CrossRef]
24. Wypych, F.; Schöllhorn, R. 1T-MoS_2, a New Metallic Modification of Molybdenum Disulfide. *J. Chem. Soc. Chem. Commun.* **1992**, *19*, 1386–1388. [CrossRef]
25. Kuc, A. Low-Dimensional Transition-Metal Dichalcogenides. In *SPR Chemical Modelling*; Royal Society of Chemistry: London, UK, 2014; Volume 11, pp. 1–29. [CrossRef]
26. Chhowalla, M.; Shin, H.S.; Eda, G.; Li, L.J.; Loh, K.P.; Zhang, H. The Chemistry of Two-Dimensional Layered Transition Metal Dichalcogenide Nanosheets. *Nat. Chem.* **2013**, *5*, 263–275. [CrossRef] [PubMed]

27. Mak, K.F.; Lee, C.; Hone, J.; Shan, J.; Heinz, T.F. Atomically Thin MoS$_2$: A New Direct-Gap Semiconductor. *Phys. Rev. Lett.* **2010**, *105*, 136805. [CrossRef] [PubMed]

28. Peng, Y.; Meng, Z.; Zhong, C.; Lu, J.; Yu, W.; Jia, Y.B.; Qian, Y. Hydrothermal Synthesis and Characterization of Single-Molecular-Layer MoS$_2$ and MoSe$_2$. *Chem. Lett.* **2003**, *30*, 772–773. [CrossRef]

29. Gong, Y.; Lin, J.; Wang, X.; Shi, G.; Lei, S.; Lin, Z.; Zou, X.; Ye, G.; Vajtai, R.; Yakobson, B.I.; et al. Vertical and In-Plane Heterostructures from WS$_2$/MoS$_2$ Monolayers. *Nat. Mater.* **2014**, *13*, 1135–1142. [CrossRef] [PubMed]

30. Wang, T.; Zheng, F.; Tang, G.; Cao, J.; You, P.; Zhao, J.; Yan, F. 2D WSe$_2$ Flakes for Synergistic Modulation of Grain Growth and Charge Transfer in Tin-Based Perovskite Solar Cells. *Adv. Sci.* **2021**, *8*, 2004315. [CrossRef]

31. Zhao, X.; Ning, S.; Fu, W.; Pennycook, S.J.; Loh, K.P. Differentiating Polymorphs in Molybdenum Disulfide via Electron Microscopy. *Adv. Mater.* **2018**, *30*, 1802397. [CrossRef]

32. Chen, J.; Tang, W.; Tian, B.; Liu, B.; Zhao, X.; Liu, Y.; Ren, T.; Liu, W.; Geng, D.; Jeong, H.Y.; et al. Chemical Vapor Deposition of High-Quality Large-Sized MoS$_2$ Crystals on Silicon Dioxide Substrates. *Adv. Sci.* **2016**, *3*, 1500033. [CrossRef]

33. Wang, Z.; Ning, S.; Fujita, T.; Hirata, A.; Chen, M. Unveiling Three-Dimensional Stacking Sequences of 1T Phase MoS$_2$ Monolayers by Electron Diffraction. *ACS Nano* **2016**, *10*, 10308–10316. [CrossRef]

34. Chen, J.; Zhao, X.; Grinblat, G.; Chen, Z.; Tan, S.J.R.; Fu, W.; Ding, Z.; Abdelwahab, I.; Li, Y.; Geng, D.; et al. Homoepitaxial Growth of Large-Scale Highly Organized Transition Metal Dichalcogenide Patterns. *Adv. Mater.* **2018**, *30*, 1704674. [CrossRef]

35. Leng, K.; Chen, Z.; Zhao, X.; Tang, W.; Tian, B.; Nai, C.T.; Zhou, W.; Loh, K.P. Phase Restructuring in Transition Metal Dichalcogenides for Highly Stable Energy Storage. *ACS Nano* **2016**, *10*, 9208–9215. [CrossRef]

36. Radisavljevic, B.; Radenovic, A.; Brivio, J.; Giacometti, V.; Kis, A. Single-Layer MoS$_2$ Transistors. *Nat. Nanotechnol.* **2011**, *6*, 147–150. [CrossRef]

37. Li, Y.; Wan, Q.; Xu, N. Recent Advances in Moiré Superlattice Systems by Angle-Resolved Photoemission Spectroscopy. *Adv. Mater.* **2023**, 2305175. [CrossRef] [PubMed]

38. Splendiani, A.; Sun, L.; Zhang, Y.; Li, T.; Kim, J.; Chim, C.Y.; Galli, G.; Wang, F. Emerging Photoluminescence in Monolayer MoS$_2$. *Nano Lett.* **2010**, *10*, 1271–1275. [CrossRef]

39. Wilson, J.A.; Yoffe, A.D. The Transition Metal Dichalcogenides Discussion and Interpretation of the Observed Optical, Electrical and Structural Properties. *Adv. Phys.* **1969**, *18*, 193–335. [CrossRef]

40. Shishidou, T.; Freeman, A.J.; Asahi, R. Effect of GGA on the Half-Metallicity of the Itinerant Ferromagnet CoS$_2$. *Phys. Rev. B Condens. Matter Mater. Phys.* **2001**, *64*, 180401. [CrossRef]

41. Fivaz, R.; Mooser, E. Mobility of Charge Carriers in Semiconducting Layer Structures. *Phys. Rev.* **1967**, *163*, 743–755. [CrossRef]

42. Fivaz, R.; Mooser, E. Electron-Phonon Interaction in Semiconducting Layer Structures. *Phys. Rev.* **1964**, *136*, A833. [CrossRef]

43. Ye, J.T.; Zhang, Y.J.; Akashi, R.; Bahramy, M.S.; Arita, R.; Iwasa, Y. Superconducting Dome in a Gate-Tuned Band Insulator. *Science* **2012**, *338*, 1193–1196. [CrossRef]

44. Ghatak, S.; Pal, A.N.; Ghosh, A. Nature of Electronic States in Atomically Thin MoS$_2$ Field-Effect Transistors. *ACS Nano* **2011**, *5*, 7707–7712. [CrossRef]

45. Yoon, Y.; Ganapathi, K.; Salahuddin, S. How Good Can Monolayer MoS$_2$ Transistors Be? *Nano Lett.* **2011**, *11*, 3768–3773. [CrossRef] [PubMed]

46. Ceulemans, A.J. *Group Theory Applied to Chemistry*; Springer: Dordrecht, The Netherlands, 2013; ISBN 940076863X.

47. Dilshod, N.; Kholmirzo, K.; Aliona, S.; Kahramon, F.; Viktoriya, G.; Tamerlan, K.; Potential, B.-J. A DFT Study of Structure, Electronic and Optical Properties of Se-Doped Kesterite Cu2ZnSnS4 (CZTSSe). *Lett. Appl. NanoBioScience* **2022**, *12*, 67. [CrossRef]

48. Silvi, B.; Gillespie, R.J.; Gatti, C. Electron Density Analysis. In *Comprehensive Inorganic Chemistry II*, 2nd ed.; Elsevier: Amsterdam, The Netherlands, 2013.

49. Deringer, V.L.; Dronskowski, R. Computational Methods for Solids. In *Comprehensive Inorganic Chemistry II*, 2nd ed.; Elsevier: Amsterdam, The Netherlands, 2013; Volume 9, pp. 59–87. [CrossRef]

50. Bermudez, V.M. Computational Study of the Adsorption of NO$_2$ on Monolayer MoS$_2$. *J. Phys. Chem. C* **2020**, *124*, 15275–15284. [CrossRef]

51. Carr, S.; Fang, S.; Kaxiras, E. Electronic-Structure Methods for Twisted Moiré Layers. *Nat. Rev. Mater.* **2020**, *5*, 748–763. [CrossRef]

52. Reidy, K.; Varnavides, G.; Thomsen, J.D.; Kumar, A.; Pham, T.; Blackburn, A.M.; Anikeeva, P.; Narang, P.; LeBeau, J.M.; Ross, F.M. Direct Imaging and Electronic Structure Modulation of Moiré Superlattices at the 2D/3D Interface. *Nat. Commun.* **2021**, *12*, 1290. [CrossRef] [PubMed]

53. Ciccarino, C.J.; Christensen, T.; Sundararaman, R.; Narang, P. Dynamics and Spin-Valley Locking Effects in Monolayer Transition Metal Dichalcogenides. *Nano Lett.* **2018**, *18*, 5709–5715. [CrossRef]

54. Sen, P. Computational Screening of Layered Metal Chalcogenide Materials for HER Electrocatalysts, and Its Synergy with Experiments. *J. Phys. Condens. Matter* **2024**, *36*, 223002. [CrossRef]

55. Han, X.; Niu, M.; Luo, Y.; Li, R.; Dan, J.; Hong, Y.; Wu, X.; Trukhanov, A.V.; Ji, W.; Wang, Y.; et al. Atomically Engineering Metal Vacancies in Monolayer Transition Metal Dichalcogenides. *Nat. Synth.* **2024**, *3*, 586–594. [CrossRef]

56. Bassman, L.; Rajak, P.; Kalia, R.K.; Nakano, A.; Sha, F.; Sun, J.; Singh, D.J.; Aykol, M.; Huck, P.; Persson, K.; et al. Active Learning for Accelerated Design of Layered Materials. *npj Comput. Mater.* **2018**, *4*, 74. [CrossRef]

57. Mao, Y.; Wang, L.; Chen, C.; Yang, Z.; Wang, J. Thickness Determination of Ultrathin 2D Materials Empowered by Machine Learning Algorithms. *Laser Photon Rev.* **2023**, *17*, 2200357. [CrossRef]

58. Schleder, G.R.; Focassio, B.; Fazzio, A. Machine Learning for Materials Discovery: Two-Dimensional Topological Insulators. *Appl. Phys. Rev.* **2021**, *8*, 031409. [CrossRef]

59. Zhao, H.; Ezeh, C.I.; Ren, W.; Li, W.; Pang, C.H.; Zheng, C.; Gao, X.; Wu, T. Integration of Machine Learning Approaches for Accelerated Discovery of Transition-Metal Dichalcogenides as Hg0 Sensing Materials. *Appl. Energy* **2019**, *254*, 113651. [CrossRef]

60. Sattari Baboukani, B.; Ye, Z.; Reyes, G.K.; Nalam, P.C. Prediction of Nanoscale Friction for Two-Dimensional Materials Using a Machine Learning Approach. *Tribol. Lett.* **2020**, *68*, 57. [CrossRef]

61. Underwood, T.M.; Robinson, R.S. Adducing Knowledge Capabilities of Instrumental Techniques Through the Exploration of Heterostructures' Modification Methods. *ChemPhysChem* **2022**, *23*, e202200241. [CrossRef]

62. Kang, J.; Tongay, S.; Zhou, J.; Li, J.; Wu, J. Band Offsets and Heterostructures of Two-Dimensional Semiconductors. *Appl. Phys. Lett.* **2013**, *102*, 012111. [CrossRef]

63. Liu, Y.; Stradins, P.; Wei, S.-H. Van Der Waals Metal-Semiconductor Junction: Weak Fermi Level Pinning Enables Effective Tuning of Schottky Barrier. *Sci. Adv.* **2016**, *2*, e1600069. [CrossRef]

64. He, F.; Zhou, Y.; Ye, Z.; Cho, S.H.; Jeong, J.; Meng, X.; Wang, Y. Moiré Patterns in 2D Materials: A Review. *ACS Nano* **2021**, *15*, 5944–5958. [CrossRef]

65. Du, L.; Molas, M.R.; Huang, Z.; Zhang, G.; Wang, F.; Sun, Z. Moiré Photonics and Optoelectronics. *Science* **2023**, *379*, eadg0014. [CrossRef]

66. Abbas, G.; Li, Y.; Wang, H.; Zhang, W.X.; Wang, C.; Zhang, H. Recent Advances in Twisted Structures of Flatland Materials and Crafting Moiré Superlattices. *Adv. Funct. Mater.* **2020**, *30*, 2000878. [CrossRef]

67. Jin, C.; Ma, E.Y.; Karni, O.; Regan, E.C.; Wang, F.; Heinz, T.F. Ultrafast Dynamics in van Der Waals Heterostructures. *Nat. Nanotechnol.* **2018**, *13*, 994–1003. [CrossRef]

68. Zhao, W.M.; Zhu, L.; Nie, Z.; Li, Q.Y.; Wang, Q.W.; Dou, L.G.; Hu, J.G.; Xian, L.; Meng, S.; Li, S.C. Moiré Enhanced Charge Density Wave State in Twisted 1T-TiTe$_2$/1T-TiSe$_2$ Heterostructures. *Nat. Mater.* **2021**, *21*, 284–289. [CrossRef] [PubMed]

69. Xie, C.; Wang, Y.; Zhang, Z.X.; Wang, D.; Luo, L.B. Graphene/Semiconductor Hybrid Heterostructures for Optoelectronic Device Applications. *Nano Today* **2018**, *19*, 41–83. [CrossRef]

70. Pai, Y.Y.; Tylan-Tyler, A.; Irvin, P.; Levy, J. Physics of SrTiO$_3$-Based Heterostructures and Nanostructures: A Review. *Rep. Prog. Phys.* **2018**, *81*, 036503. [CrossRef] [PubMed]

71. Gupta, S.; Johnston, A.; Khondaker, S. Optoelectronic Properties of MoS$_2$/Graphene Heterostructures Prepared by Dry Transfer for Light-Induced Energy Applications. *J. Electron. Mater.* **2022**, *51*, 4257–4269. [CrossRef]

72. Suganthi, N.; Kannan, K.; Thangavel, S. Nanostructured Metal Oxide and Hybrid Photocatalyst for Water Treatment and Hydrogen Generation. In *Heterojunction Photocatalytic Materials*; Jenny Stanford Publishing: Dubai, United Arab Emirates, 2022; pp. 395–414. [CrossRef]

73. Bhattacharya, P.; Fornari, R.; Kamimura, H. *Comprehensive Semiconductor Science and Technology*; Elsevier: Amsterdam, The Netherlands, 2011; ISBN 0080932282.

74. Bag, A.; Lee, N.E. Gas Sensing with Heterostructures Based on Two-Dimensional Nanostructured Materials: A Review. *J. Mater. Chem. C Mater.* **2019**, *7*, 13367–13383. [CrossRef]

75. Tian, J.; Zhao, Z.; Kumar, A.; Boughton, R.I.; Liu, H. Recent Progress in Design, Synthesis, and Applications of One-Dimensional TiO$_2$ Nanostructured Surface Heterostructures: A Review. *Chem. Soc. Rev.* **2014**, *43*, 6920–6937. [CrossRef] [PubMed]

76. Pan, S.; Li, J.; Wen, Z.; Lu, R.; Zhang, Q.; Jin, H.; Zhang, L.; Chen, Y.; Wang, S.; Pan, S.; et al. Halide Perovskite Materials for Photo(Electro)Chemical Applications: Dimensionality, Heterojunction, and Performance. *Adv. Energy Mater.* **2022**, *12*, 2004002. [CrossRef]

77. Nandi, P.; Das, D. ZnO/CdS/CuS Heterostructure: A Suitable Candidate for Applications in Visible-Light Photocatalysis. *J. Phys. Chem. Solids* **2022**, *160*, 110344. [CrossRef]

78. Pham, P.V.; Bodepudi, S.C.; Shehzad, K.; Liu, Y.; Xu, Y.; Yu, B.; Duan, X. 2D Heterostructures for Ubiquitous Electronics and Optoelectronics: Principles, Opportunities, and Challenges. *Chem. Rev.* **2022**, *122*, 6514–6613. [CrossRef] [PubMed]

79. Kumari, P.; Bahadur, N.; Kong, L.; O'Dell, L.A.; Merenda, A.; Dumée, L.F. Engineering Schottky-like and Heterojunction Materials for Enhanced Photocatalysis Performance—A Review. *Mater. Adv.* **2022**, *3*, 2309–2323. [CrossRef]

80. Li, S.; Zhao, Z.; Liu, M.; Liu, X.; Huang, W.; Sun, S.; Jiang, Y.; Liu, Y.; Zhang, J.; Zhang, Z. Remarkably Enhanced Photocatalytic Performance of Au/AgNbO$_3$ Heterostructures by Coupling Piezotronic with Plasmonic Effects. *Nano Energy* **2022**, *95*, 107031. [CrossRef]

81. Zhao, Y.; Linghu, X.; Shu, Y.; Zhang, J.; Chen, Z.; Wu, Y.; Shan, D.; Wang, B. Classification and Catalytic Mechanisms of Heterojunction Photocatalysts and the Application of Titanium Dioxide (TiO$_2$)-Based Heterojunctions in Environmental Remediation. *J. Environ. Chem. Eng.* **2022**, *10*, 108077. [CrossRef]

82. Ehrenreich, H.; Turnbull, D. *Advances in Research and Applications: Semiconductor Heterostructures and Nanostructures*; Elsevier: Amsterdam, The Netherlands, 1991.

83. Liu, Y.; Fang, Y.; Yang, D.; Pi, X.; Wang, P. Recent Progress of Heterostructures Based on Two Dimensional Materials and Wide Bandgap Semiconductors. *J. Phys. Condens. Matter* **2022**, *34*, 183001. [CrossRef]

84. Jabbar, Z.H.; Esmail Ebrahim, S. Recent Advances in Nano-Semiconductors Photocatalysis for Degrading Organic Contaminants and Microbial Disinfection in Wastewater: A Comprehensive Review. *Environ. Nanotechnol. Monit. Manag.* **2022**, *17*, 100666. [CrossRef]

85. Ostroff, E.; Parekh, K.; Prominski, A.; Tian, B. Biocompatible and Nanoenabled Technologies for Biological Modulation. *Adv. Mater. Technol.* **2022**, *7*, 2100216. [CrossRef]

86. Chen, Z.; Zhang, J.; Lyu, Q.; Wang, H.; Ji, X.; Yan, Z.; Chen, F.; Dahlgren, R.A.; Zhang, M. Modular Configurations of Living Biomaterials Incorporating Nano-Based Artificial Mediators and Synthetic Biology to Improve Bioelectrocatalytic Performance: A Review. *Sci. Total Environ.* **2022**, *824*, 153857. [CrossRef] [PubMed]

87. Lin, H.; Li, T.; Janani, B.J.; Fakhri, A. Fabrication of Cu_2MoS_4 Decorated WO_3 Nano Heterojunction Embedded on Chitosan: Robust Photocatalytic Efficiency, Antibacterial Performance, and Bacteria Detection by Peroxidase Activity. *J. Photochem. Photobiol. B* **2022**, *226*, 112354. [CrossRef]

88. Adolfsson, K.; Persson, H.; Wallentin, J.; Oredsson, S.; Samuelson, L.; Tegenfeldt, J.O.; Borgström, M.T.; Prinz, C.N. Fluorescent Nanowire Heterostructures as a Versatile Tool for Biology Applications. *Nano Lett.* **2013**, *13*, 4728–4732. [CrossRef]

89. Jiang, Z.; Wang, B.; Yu, J.C.; Wang, J.; An, T.; Zhao, H.; Li, H.; Yuan, S.; Wong, P.K. $AgInS_2/In_2S_3$ Heterostructure Sensitization of Escherichia Coli for Sustainable Hydrogen Production. *Nano Energy* **2018**, *46*, 234–240. [CrossRef]

90. Huang, M.; Zhang, R.; Yang, Z.; Chen, J.; Deng, J.; Fakhri, A.; Gupta, V.K. Synthesis of Co_3S_4-SnO_2/Polyvinylpyrrolidone-Cellulose Heterojunction as Highly Performance Catalyst for Photocatalytic and Antimicrobial Properties under Ultra-Violet Irradiation. *Int. J. Biol. Macromol.* **2020**, *162*, 220–228. [CrossRef]

91. Ayodhya, D.; Veerabhadram, G. A Review on Recent Advances in Photodegradation of Dyes Using Doped and Heterojunction Based Semiconductor Metal Sulfide Nanostructures for Environmental Protection. *Mater. Today Energy* **2018**, *9*, 83–113. [CrossRef]

92. Hill, H.M.; Rigosi, A.F.; Rim, K.T.; Flynn, G.W.; Heinz, T.F. Band Alignment in MoS_2/WS_2 Transition Metal Dichalcogenide Heterostructures Probed by Scanning Tunneling Microscopy and Spectroscopy. *Nano Lett.* **2016**, *16*, 4831–4837. [CrossRef] [PubMed]

93. Lv, R.; Terrones, H.; Elías, A.L.; Perea-López, N.; Gutiérrez, H.R.; Cruz-Silva, E.; Rajukumar, L.P.; Dresselhaus, M.S.; Terrones, M. Two-Dimensional Transition Metal Dichalcogenides: Clusters, Ribbons, Sheets and More. *Nano Today* **2015**, *10*, 559–592. [CrossRef]

94. Froehlicher, G.; Lorchat, E.; Berciaud, S. Direct versus Indirect Band Gap Emission and Exciton-Exciton Annihilation in Atomically Thin Molybdenum Ditelluride ($MoTe_2$). *Phys. Rev. B* **2016**, *94*, 085429. [CrossRef]

95. Lee, C.H.; Silva, E.C.; Calderin, L.; Nguyen, M.A.T.; Hollander, M.J.; Bersch, B.; Mallouk, T.E.; Robinson, J.A. Tungsten Ditelluride: A Layered Semimetal. *Sci. Rep.* **2015**, *5*, 10013. [CrossRef] [PubMed]

96. Schmidt, A.; Zarbin, A.J.G. Molybdenum-Based Two-Dimensional Materials: Synthesis, Dispersion, Exfoliation and Thin Film Deposition. *J. Colloid. Interface Sci.* **2019**, *554*, 80–90. [CrossRef] [PubMed]

97. Costa, M.B.; Lucas, F.W.S.; Medina, M.; Mascaro, L.H. All-Electrochemically Grown Sb_2Se_3/a-MoSx Photocathodes for Hydrogen Production: The Effect of the MoSx Layer on the Surface Recombination and Photocorrosion of Sb_2Se_3 Films. *ACS Appl. Energy Mater.* **2020**, *3*, 9799–9808. [CrossRef]

98. Zang, Y.; Lei, J.; Hao, Q.; Ju, H. CdS/MoS_2 heterojunction-Based Photoelectrochemical DNA Biosensor via Enhanced Chemiluminescence Excitation. *Biosens. Bioelectron.* **2016**, *77*, 557–564. [CrossRef] [PubMed]

99. Li, W.; Liu, G.; Li, J.; Wang, Y.; Ricardez-Sandoval, L.; Zhang, Y.; Zhang, Z. Hydrogen Evolution Reaction Mechanism on $2H$-MoS_2 Electrocatalyst. *Appl. Surf. Sci.* **2019**, *498*, 143869. [CrossRef]

100. Lembke, D.; Bertolazzi, S.; Kis, A. Single-Layer MoS_2 Electronics. *Acc. Chem. Res.* **2015**, *48*, 100–110. [CrossRef]

101. Vazirisereshk, M.R.; Martini, A.; Strubbe, D.A.; Baykara, M.Z. Solid Lubrication with MoS_2: A Review. *Lubricants* **2019**, *7*, 57. [CrossRef]

102. Lu, Z.; Lin, Q.; Cao, Z.; Li, W.; Gong, J.; Wang, Y.; Hu, K.; Hu, X. MoS_2 Nanomaterials as Lubricant Additives: A Review. *Lubricants* **2023**, *11*, 527. [CrossRef]

103. Lin, T.Z.; Kang, B.T.; Jeon, M.H.; Huffman, C.; Jeon, J.H.; Lee, S.J.; Han, W.; Lee, J.Y.; Lee, S.H.; Yeom, G.Y.; et al. Controlled Layer-by-Layer Etching of MoS_2. *ACS Appl. Mater. Interfaces* **2015**, *7*, 15892–15897. [CrossRef] [PubMed]

104. Medina, M.; Corradini, P.G.; de Brito, J.F.; Sousa Santos, H.L.; Mascaro, L.H. The Substrate Morphology Effect for Sulfur-Rich Amorphous Molybdenum Sulfide for Electrochemical Hydrogen Evolution Reaction. *J. Electrochem. Soc.* **2022**, *169*, 026519. [CrossRef]

105. Jaramillo, T.F.; Jørgensen, K.P.; Bonde, J.; Nielsen, J.H.; Horch, S.; Chorkendorff, I. Identification of Active Edge Sites for Electrochemical H_2 evolution from MoS_2 nanocatalysts. *Science* **2007**, *317*, 100–102. [CrossRef] [PubMed]

106. Karunadasa, H.I.; Montalvo, E.; Sun, Y.; Majda, M.; Long, J.R.; Chang, C.J. A Molecular MoS_2 Edge Site Mimic for Catalytic Hydrogen Generation. *Science* **2012**, *335*, 698–702. [CrossRef] [PubMed]

107. Sygellou, L.; Tzanidis, I.; Tasis, D. Investigation of Electronic Properties and Chemical Interactions of Graphene-MoSx Composites. *Appl. Surf. Sci.* **2020**, *517*, 146188. [CrossRef]

108. Kallatt, S.; Umesh, G.; Bhat, N.; Majumdar, K. Photoresponse of Atomically Thin MoS_2 Layers and Their Planar Heterojunctions. *Nanoscale* **2016**, *8*, 15213–15222. [CrossRef] [PubMed]

109. Li, H.; Wu, J.; Yin, Z.; Zhang, H. Preparation and Applications of Mechanically Exfoliated Single-Layer and Multilayer MoS_2 and WSe_2 Nanosheets. *Acc. Chem. Res.* **2014**, *47*, 1067–1075. [CrossRef] [PubMed]

110. Coy Diaz, H.; Addou, R.; Batzill, M. Interface Properties of CVD Grown Graphene Transferred onto MoS_2 (0001). *Nanoscale* **2014**, *6*, 1071–1078. [CrossRef]

111. Furimsky, E. Role of MoS_2 and WS_2 in Hydrodesulfuritation. *Catal. Rev. Sci. Eng.* **1980**, *22*, 371–400. [CrossRef]

112. Mom, R.V.; Louwen, J.N.; Frenken, J.W.M.; Groot, I.M.N. In Situ Observations of an Active MoS$_2$ Model Hydrodesulfurization Catalyst. *Nat. Commun.* **2019**, *10*, 2546. [CrossRef]

113. Zhang, X.; Chen, B.; Wang, J.; Zhou, Y.; Huang, X.; Huang, H.; Wang, X.; Li, K. Review of Molybdenum Disulfide Research in Slurry Bed Heavy Oil Hydrogenation. *ACS Omega* **2023**, *8*, 18400–18407. [CrossRef] [PubMed]

114. Samy, O.; El Moutaouakil, A.; Mutta, K.; Ray, S.J. A Review on MoS$_2$ Energy Applications: Recent Developments and Challenges. *Energies* **2021**, *14*, 4586. [CrossRef]

115. Lee, G.H.; Yu, Y.J.; Cui, X.; Petrone, N.; Lee, C.H.; Choi, M.S.; Lee, D.Y.; Lee, C.; Yoo, W.J.; Watanabe, K.; et al. Flexible and Transparent MoS$_2$ Field-Effect Transistors on Hexagonal Boron Nitride-Graphene Heterostructures. *ACS Nano* **2013**, *7*, 7931–7936. [CrossRef]

116. Bertolazzi, S.; Krasnozhon, D.; Kis, A. Nonvolatile Memory Cells Based on MoS$_2$/Graphene Heterostructures. *ACS Nano* **2013**, *7*, 3246–3252. [CrossRef] [PubMed]

117. Bernardi, M.; Palummo, M.; Grossman, J.C. Extraordinary Sunlight Absorption and One Nanometer Thick Photovoltaics Using Two-Dimensional Monolayer Materials. *Nano Lett.* **2013**, *13*, 3664–3670. [CrossRef]

118. Eda, G.; Yamaguchi, H.; Voiry, D.; Fujita, T.; Chen, M.; Chhowalla, M. Photoluminescence from Chemically Exfoliated MoS$_2$. *Nano Lett.* **2011**, *11*, 5111–5116. [CrossRef]

119. Jha, R.K.; Guha, P.K. Humidity Sensing Properties of Coexfoliated Heterogeneous WS$_2$/WSe$_2$ Nanohybrids. *IEEE Trans. Nanotechnol.* **2018**, *17*, 582–589. [CrossRef]

120. Zhao, P.; Wang, J.; Wang, Z.; Nie, M. Mechanical Behavior of Monolayer MoS$_2$ Films with Arrayed Dislocation Defects. *Results Phys.* **2023**, *49*, 106514. [CrossRef]

121. Yu, Q.; Jauregui, L.A.; Wu, W.; Colby, R.; Tian, J.; Su, Z.; Cao, H.; Liu, Z.; Pandey, D.; Wei, D.; et al. Control and Characterization of Individual Grains and Grain Boundaries in Graphene Grown by Chemical Vapour Deposition. *Nat. Mater.* **2011**, *10*, 443–449. [CrossRef] [PubMed]

122. Lee, C.; Yan, H.; Brus, L.E.; Heinz, T.F.; Hone, J.; Ryu, S. Anomalous Lattice Vibrations of Single- and Few-Layer MoS$_2$. *ACS Nano* **2010**, *4*, 2695–2700. [CrossRef]

123. Jones, A.M.; Yu, H.; Ghimire, N.J.; Wu, S.; Aivazian, G.; Ross, J.S.; Zhao, B.; Yan, J.; Mandrus, D.G.; Xiao, D.; et al. Optical Generation of Excitonic Valley Coherence in Monolayer WSe$_2$. *Nat. Nanotechnol.* **2013**, *8*, 634–638. [CrossRef] [PubMed]

124. Niazi, S.; Khan, I.M.; Yu, Y.; Pasha, I.; Shoaib, M.; Mohsin, A.; Mushtaq, B.S.; Akhtar, W.; Wang, Z. A "Turnon" Aptasensor for Simultaneous and Time-Resolved Fluorometric Determination of Zearalenone, Trichothecenes A and Aflatoxin B1 Using WS$_2$ as a Quencher. *Microchim. Acta* **2019**, *186*, 575. [CrossRef]

125. Zhou, J.; Wang, Q.; Geng, S.; Lou, R.; Yin, Q.; Ye, W. Construction and Evaluation of Tumor Nucleus-Targeting Nanocomposite for Cancer Dual-Mode Imaging—Guiding Photodynamic Therapy/Photothermal Therapy. *Mater. Sci. Eng. C* **2019**, *102*, 541–551. [CrossRef] [PubMed]

126. Jo, S.; Ubrig, N.; Berger, H.; Kuzmenko, A.B.; Morpurgo, A.F. Mono- and Bilayer WS$_2$ Light-Emitting Transistors. *Nano Lett.* **2014**, *14*, 2019–2025. [CrossRef]

127. Demirtaş, M.; Odacı, C.; Shehu, Y.; Perkgöz, N.K.; Ay, F. Layer and Size Distribution Control of CVD-Grown 2D MoS$_2$ Using ALD-Deposited MoO$_3$ Structures as the Precursor. *Mater. Sci. Semicond. Process* **2020**, *108*, 104880. [CrossRef]

128. Brorson, M.; Carlsson, A.; Topsøe, H. The Morphology of MoS$_2$, WS$_2$, Co–Mo–S, Ni–Mo–S and Ni–W–S Nanoclusters in Hydrodesulfurization Catalysts Revealed by HAADF-STEM. *Catal. Today* **2007**, *123*, 31–36. [CrossRef]

129. Tsverin, Y.; Popovitz-Biro, R.; Feldman, Y.; Tenne, R.; Komarneni, M.R.; Yu, Z.; Chakradhar, A.; Sand, A.; Burghaus, U. Synthesis and Characterization of WS$_2$ Nanotube Supported Cobalt Catalyst for Hydrodesulfurization. *Mater. Res. Bull.* **2012**, *47*, 1653–1660. [CrossRef]

130. Chen, T.Y.; Chang, Y.H.; Hsu, C.L.; Wei, K.H.; Chiang, C.Y.; Li, L.J. Comparative Study on MoS$_2$ and WS$_2$ for Electrocatalytic Water Splitting. *Int. J. Hydrog. Energy* **2013**, *38*, 12302–12309. [CrossRef]

131. Kumar, P.; Kataria, S.; Roy, S.; Jaiswal, A.; Balakrishnan, V. Photocatalytic Water Disinfection of CVD Grown WS$_2$ Monolayer Decorated with Ag Nanoparticles. *ChemistrySelect* **2018**, *3*, 7648–7655. [CrossRef]

132. Cheng, P.; Chen, Y.; Yan, X.; Wang, Y.; Lang, W.Z. Highly Stable and Antibacterial Two-Dimensional Tungsten Disulfide Lamellar Membrane for Water Filtration. *ChemSusChem* **2019**, *12*, 275–282. [CrossRef]

133. Liu, Y.; Liu, J. Hybrid Nanomaterials of WS$_2$ or MoS$_2$ Nanosheets with Liposomes: Biointerfaces and Multiplexed Drug Delivery. *Nanoscale* **2017**, *9*, 13187–13194. [CrossRef] [PubMed]

134. Liu, N.; Fan, F.; Xu, W.; Zhang, H.; Zhou, Q.; Li, X. Synthesis of Functional Hollow WS$_2$ Particles with Large Surface Area for Near-Infrared (NIR) Triggered Drug Delivery. *J. Alloys Compd.* **2021**, *875*, 160034. [CrossRef]

135. Cong, C.; Shang, J.; Wang, Y.; Yu, T. Optical Properties of 2D Semiconductor WS$_2$. *Adv. Opt. Mater.* **2018**, *6*, 1700767. [CrossRef]

136. Chen, J.; Shao, K.; Yang, W.; Tang, W.; Zhou, J.; He, Q.; Wu, Y.; Zhang, C.; Li, X.; Yang, X.; et al. Synthesis of Wafer-Scale Monolayer WS$_2$ Crystals toward the Application in Integrated Electronic Devices. *ACS Appl. Mater. Interfaces* **2019**, *11*, 19381–19387. [CrossRef]

137. Lan, C.; Li, C.; Ho, J.C.; Liu, Y. 2D WS$_2$: From Vapor Phase Synthesis to Device Applications. *Adv. Electron. Mater.* **2021**, *7*, 2000688. [CrossRef]

138. Gusakova, J.; Wang, X.; Shiau, L.L.; Krivosheeva, A.; Shaposhnikov, V.; Borisenko, V.; Gusakov, V.; Tay, B.K. Electronic Properties of Bulk and Monolayer TMDs: Theoretical Study Within DFT Framework (GVJ-2e Method). *Phys. Status Solidi* **2017**, *214*, 1700218. [CrossRef]

139. Myja, H.; Yang, Z.; Goldthorpe, I.A.; Jones, A.J.B.; Musselman, K.P.; Grundmann, A.; Kalisch, H.; Vescan, A.; Heuken, M.; Kümmell, T.; et al. Silver Nanowire Electrodes for Transparent Light Emitting Devices Based on WS$_2$ Monolayers. *Nanotechnology* **2023**, *34*, 285201. [CrossRef]

140. Yang, W.; Shang, J.; Wang, J.; Shen, X.; Cao, B.; Peimyoo, N.; Zou, C.; Chen, Y.; Wang, Y.; Cong, C.; et al. Electrically Tunable Valley-Light Emitting Diode (VLED) Based on CVD-Grown Monolayer WS$_2$. *Nano Lett.* **2016**, *16*, 1560–1567. [CrossRef]

141. Ghorai, A.; Bayan, S.; Gogurla, N.; Midya, A.; Ray, S.K. Highly Luminescent WS$_2$ Quantum Dots/ZnO Heterojunctions for Light Emitting Devices. *ACS Appl. Mater. Interfaces* **2017**, *9*, 558–565. [CrossRef] [PubMed]

142. Kosmala, T.; Palczynski, P.; Amati, M.; Gregoratti, L.; Sezen, H.; Mattevi, C.; Agnoli, S.; Granozzi, G. Strain Induced Phase Transition of WS$_2$ by Local Dewetting of Au/Mica Film upon Annealing. *Surfaces* **2020**, *4*, 1. [CrossRef]

143. Khalil, A.; Liu, Q.; He, Q.; Xiang, T.; Liu, D.; Wang, C.; Fang, Q.; Song, L. Metallic 1T-WS$_2$ Nanoribbons as Highly Conductive Electrodes for Supercapacitors. *RSC Adv.* **2016**, *6*, 48788–48791. [CrossRef]

144. Anto Jeffery, A.; Nethravathi, C.; Rajamathi, M. Two-Dimensional Nanosheets and Layered Hybrids of MoS$_2$ and WS$_2$ through Exfoliation of Ammoniated MS2 (M = Mo, W). *J. Phys. Chem. C* **2014**, *118*, 1386–1396. [CrossRef]

145. Liang, Z.; Yang, S.; Wang, X.; Cui, H.; Wang, X.; Tian, J. The Metallic 1T-Phase WS$_2$ Nanosheets as Cocatalysts for Enhancing the Photocatalytic Hydrogen Evolution of g-C3N4 Nanotubes. *Appl. Catal. B* **2020**, *274*, 119114. [CrossRef]

146. Srinivaas, M.; Wu, C.Y.; Duh, J.G.; Wu, J.M. Highly Rich 1T Metallic Phase of Few-Layered WS$_2$ Nanoflowers for Enhanced Storage of Lithium-Ion Batteries. *ACS Sustain. Chem. Eng.* **2019**, *7*, 10363–10370. [CrossRef]

147. Toh, R.J.; Sofer, Z.; Luxa, J.; Sedmidubský, D.; Pumera, M. 3R Phase of MoS$_2$ and WS$_2$ Outperforms the Corresponding 2H Phase for Hydrogen Evolution. *Chem. Commun.* **2017**, *53*, 3054–3057. [CrossRef]

148. Tributsch, H. Hole Reactions from D-Energy Bands of Layer Type Group VI Transition Metal Dichalcogenides: New Perspectives for Electrochemical Solar Energy Conversion. *J. Electrochem. Soc.* **1978**, *125*, 1086–1093. [CrossRef]

149. Salarvand, V.; Abedini Mohammadi, M.; Yousefifar, A.; Yazdi, M.S.; Mostafaei, A. Facile Hydrothermal Synthesis of Combined MoSe$_2$PS Nanostructures on Nickel Foam with Superior Electrocatalytic Properties for Hydrogen Evolution Reaction. *Int. J. Hydrog. Energy* **2023**, *48*, 10038–10050. [CrossRef]

150. Shu, H.; Zhou, D.; Li, F.; Cao, D.; Chen, X. Defect Engineering in MoSe$_2$ for the Hydrogen Evolution Reaction: From Point Defects to Edges. *ACS Appl. Mater. Interfaces* **2017**, *9*, 42688–42698. [CrossRef]

151. Tang, H.; Dou, K.; Kaun, C.C.; Kuang, Q.; Yang, S. MoSe$_2$ Nanosheets and Their Graphene Hybrids: Synthesis, Characterization and Hydrogen Evolution Reaction Studies. *J. Mater. Chem. A Mater.* **2013**, *2*, 360–364. [CrossRef]

152. He, B.; Li, G.; Li, J.; Wang, J.; Tong, H.; Fan, Y.; Wang, W.; Sun, S.; Dang, F. MoSe$_2$@CNT Core–Shell Nanostructures as Grain Promoters Featuring a Direct Li$_2$O$_2$ Formation/Decomposition Catalytic Capability in Lithium-Oxygen Batteries. *Adv. Energy Mater.* **2021**, *11*, 2003263. [CrossRef]

153. Zhou, Z.; Zhao, L.; Liu, Y.; Li, D.; Xia, Q.; Wang, J.; Zhang, Z.; Han, X.; Long, Y.; Zhang, Y.; et al. 2H-MoS$_2$ Modified Nitrogen-Doped Hollow Mesoporous Carbon Spheres as the Efficient Catalytic Cathode Catalyst for Aprotic Lithium-Oxygen Batteries. *Renewables* **2023**, *1*, 100–111. [CrossRef]

154. Sun, Q.; Wen, Y.; Jiang, S.; Li, X.; Yao, Z.; Liu, T.; Shen, S.; Yang, Y. Coupling of NiSe$_2$ with MoSe$_2$ Confined in Nitrogen-Doped Carbon Spheres as Anodes for Fast and Durable Sodium Storage. *J. Alloys Compd.* **2023**, *944*, 169157. [CrossRef]

155. Eftekhari, A. Molybdenum Diselenide (MoSe$_2$) for Energy Storage, Catalysis, and Optoelectronics. *Appl. Mater. Today* **2017**, *8*, 1–17. [CrossRef]

156. Wang, H.; Xu, M.; Ji, H.; He, T.; Li, W.; Zheng, L.; Wang, X. Laser-Assisted Synthesis of Two-Dimensional Transition Metal Dichalcogenides: A Mini Review. *Front. Chem.* **2023**, *11*, 1195640. [CrossRef]

157. Bhavani, P.; Praveen Kumar, D.; Hussain, M.; Chen, W.H.; Lam, S.S.; Park, Y.K. Surface Ligand Functionalized Few-Layered MoSe$_2$ Nanosheets Decorated CdS Nanorods for Spectacular Rate of H2 Production. *Fuel* **2023**, *334*, 126551. [CrossRef]

158. Wang, L.; Zhao, J.; Tang, X.; Kuang, S.; Qin, L.; Lin, H.; Li, Q. Green Synthesis of MoSe$_2$ Nanosheets Based on Hydrogen Bond with High Photodegradation Performance. *Surf. Interfaces* **2023**, *39*, 102956. [CrossRef]

159. Dai, T.J.; Liu, Y.C.; Fan, X.D.; Liu, X.Z.; Xie, D.; Li, Y.R. Synthesis of Few-Layer 2H-MoSe$_2$ Thin Films with Wafer-Level Homogeneity for High-Performance Photodetector. *Nanophotonics* **2018**, *7*, 1959–1969. [CrossRef]

160. Shaw, J.C.; Zhou, H.; Chen, Y.; Weiss, N.O.; Liu, Y.; Huang, Y.; Duan, X. Chemical Vapor Deposition Growth of Monolayer MoSe$_2$ Nanosheets. *Nano Res.* **2014**, *7*, 511–517. [CrossRef]

161. Krbal, M.; Prikryl, J.; Zazpe, R.; Dvorak, F.; Bures, F.; Macak, J.M. 2D MoSe$_2$ Structures Prepared by Atomic Layer Deposition. *Phys. Status Solidi Rapid Res. Lett.* **2018**, *12*, 1800023. [CrossRef]

162. Sharma, R.; Dawar, A.; Ojha, S.; Laishram, R.; Sathe, V.G.; Srivastava, R.; Sinha, O.P. A Thrifty Liquid-Phase Exfoliation (LPE) of MoSe$_2$ and WSe$_2$ Nanosheets as Channel Materials for FET Application. *J. Electron. Mater.* **2023**, *52*, 2819–2830. [CrossRef]

163. Azam, A.; Yang, J.; Li, W.; Huang, J.K.; Li, S. Tungsten Diselenides (WSe$_2$) Quantum Dots: Fundamental, Properties, Synthesis and Applications. *Prog. Mater. Sci.* **2023**, *132*, 101042. [CrossRef]

164. Ugeda, M.M.; Pulkin, A.; Tang, S.; Ryu, H.; Wu, Q.; Zhang, Y.; Wong, D.; Pedramrazi, Z.; Martín-Recio, A.; Chen, Y.; et al. Observation of Topologically Protected States at Crystalline Phase Boundaries in Single-Layer WSe$_2$. *Nat. Commun.* **2018**, *9*, 3401. [CrossRef] [PubMed]

165. Kim, J.K.; Cho, K.; Jang, J.; Baek, K.Y.; Kim, J.; Seo, J.; Song, M.; Shin, J.; Kim, J.; Parkin, S.S.P.; et al. Molecular Dopant-Dependent Charge Transport in Surface-Charge-Transfer-Doped Tungsten Diselenide Field Effect Transistors. *Adv. Mater.* **2021**, *33*, 2101598. [CrossRef]

166. Del Pozo-Zamudio, O.; Genco, A.; Schwarz, S.; Withers, F.; Walker, P.M.; Godde, T.; Schofield, R.C.; Rooney, A.P.; Prestat, E.; Watanabe, K.; et al. Electrically Pumped WSe$_2$-Based Light-Emitting van Der Waals Heterostructures Embedded in Monolithic Dielectric Microcavities. *2D Mater.* **2020**, *7*, 031006. [CrossRef]

167. Li, Y.; Xiao, J.; Cao, X.; Gu, Z.; Zhang, W.; Li, Y.; Xiao, J.; Cao, X.; Gu, Z.; Zhang, W. Lateral WSe$_2$ Homojunction through Metal Contact Doping: Excellent Self-Powered Photovoltaic Photodetector. *Adv. Funct. Mater.* **2023**, *33*, 2213385. [CrossRef]

168. Zhang, X.; Kakani, V.; Woods, J.M.; Cha, J.J.; Shi, X. Thickness Dependence of Magnetotransport Properties of Tungsten Ditelluride. *Phys. Rev. B* **2021**, *104*, 165126. [CrossRef]

169. Yang, D.; Hu, X.; Zhuang, M.; Ding, Y.; Zhou, S.; Li, A.; Yu, Y.; Li, H.; Luo, Z.; Gan, L.; et al. Inversion Symmetry Broken 2D 3R-MoTe$_2$. *Adv. Funct. Mater.* **2018**, *28*, 1800785. [CrossRef]

170. Hussain, S.; Patil, S.A.; Vikraman, D.; Mengal, N.; Liu, H.; Song, W.; An, K.S.; Jeong, S.H.; Kim, H.S.; Jung, J. Large Area Growth of MoTe$_2$ Films as High Performance Counter Electrodes for Dye-Sensitized Solar Cells. *Sci. Rep.* **2018**, *8*, 29. [CrossRef]

171. Chen, J.; Feng, Z.; Fan, S.; Shi, S.; Yue, Y.; Shen, W.; Xie, Y.; Wu, E.; Sun, C.; Liu, J.; et al. Contact Engineering of Molybdenum Ditelluride Field Effect Transistors through Rapid Thermal Annealing. *ACS Appl. Mater. Interfaces* **2017**, *9*, 30107–30114. [CrossRef] [PubMed]

172. Afzal, A.M.; Iqbal, M.Z.; Dastgeer, G.; ul Ahmad, A.; Park, B. Highly Sensitive, Ultrafast, and Broadband Photo-Detecting Field-Effect Transistor with Transition-Metal Dichalcogenide van Der Waals Heterostructures of MoTe$_2$ and PdSe$_2$. *Adv. Sci.* **2021**, *8*, 2003713. [CrossRef] [PubMed]

173. Bhat, K.S.; Nagaraja, H.S. Performance Evaluation of Molybdenum Dichalcogenide (MoX$_2$; X = S, Se, Te) Nanostructures for Hydrogen Evolution Reaction. *Int. J. Hydrog. Energy* **2019**, *44*, 17878–17886. [CrossRef]

174. Sarwar, S.; Ali, A.; Liu, Z.; Li, J.; Uprety, S.; Lee, H.; Wang, R.; Park, M.; Bozack, M.J.; Adamczyk, A.J.; et al. Towards Thermoneutral Hydrogen Evolution Reaction Using Noble Metal Free Molybdenum Ditelluride/Graphene Nanocomposites. *J. Colloid. Interface Sci.* **2021**, *581*, 847–859. [CrossRef]

175. McGlynn, J.C.; Dankwort, T.; Kienle, L.; Bandeira, N.A.G.; Fraser, J.P.; Gibson, E.K.; Cascallana-Matías, I.; Kamarás, K.; Symes, M.D.; Miras, H.N.; et al. The Rapid Electrochemical Activation of MoTe$_2$ for the Hydrogen Evolution Reaction. *Nat. Commun.* **2019**, *10*, 4916. [CrossRef]

176. Ali, M.N.; Xiong, J.; Flynn, S.; Tao, J.; Gibson, Q.D.; Schoop, L.M.; Liang, T.; Haldolaarachchige, N.; Hirschberger, M.; Ong, N.P.; et al. Large, Non-Saturating Magnetoresistance in WTe$_2$. *Nature* **2014**, *514*, 205–208. [CrossRef]

177. Sharma, P.; Xiang, F.X.; Shao, D.F.; Zhang, D.; Tsymbal, E.Y.; Hamilton, A.R.; Seidel, J. A Room-Temperature Ferroelectric Semimetal. *Sci. Adv.* **2019**, *5*, eaax5080. [CrossRef]

178. Wilson, J.A.; Di Salvo, F.J.; Mahajan, S. Charge-Density Waves and Superlattices in the Metallic Layered Transition Metal Dichalcogenides. *Adv. Phys.* **1975**, *24*, 117–201. [CrossRef]

179. Revolinsky, E.; Beerntsen, D. Electrical Properties of the MoTe$_2$−WTe$_2$ and MoSe$_2$−WSe$_2$ Systems. *J. Appl. Phys.* **1964**, *35*, 2086–2089. [CrossRef]

180. Qi, H.; Wang, L.; Sun, J.; Long, Y.; Hu, P.; Liu, F.; He, X. Production Methods of Van Der Waals Heterostructures Based on Transition Metal Dichalcogenides. *Crystals* **2018**, *8*, 35. [CrossRef]

181. Rooney, A.P.; Kozikov, A.; Rudenko, A.N.; Prestat, E.; Hamer, M.J.; Withers, F.; Cao, Y.; Novoselov, K.S.; Katsnelson, M.I.; Gorbachev, R.; et al. Observing Imperfection in Atomic Interfaces for van Der Waals Heterostructures. *Nano Lett.* **2017**, *17*, 5222–5228. [CrossRef] [PubMed]

182. Kim, J.Y.; Ju, X.; Ang, K.W.; Chi, D. Van Der Waals Layer Transfer of 2D Materials for Monolithic 3D Electronic System Integration: Review and Outlook. *ACS Nano* **2022**, *17*, 1831–1844. [CrossRef] [PubMed]

183. Lu, C.; Yu, S.; Novoselov, K.S.; Castro Neto, A.H. Two-Dimensional Crystals-Based Heterostructures: Materials with Tailored Properties. *Phys. Scr.* **2012**, *2012*, 014006. [CrossRef]

184. Gupta, A.; Sakthivel, T.; Seal, S. Recent Development in 2D Materials beyond Graphene. *Prog. Mater. Sci.* **2015**, *73*, 44–126. [CrossRef]

185. Wang, Q.H.; Kalantar-Zadeh, K.; Kis, A.; Coleman, J.N.; Strano, M.S. Electronics and Optoelectronics of Two-Dimensional Transition Metal Dichalcogenides. *Nat. Nanotechnol.* **2012**, *7*, 699–712. [CrossRef] [PubMed]

186. Coleman, J.N.; Lotya, M.; O'Neill, A.; Bergin, S.D.; King, P.J.; Khan, U.; Young, K.; Gaucher, A.; De, S.; Smith, R.J.; et al. Two-Dimensional Nanosheets Produced by Liquid Exfoliation of Layered Materials. *Science* **2011**, *331*, 568–571. [CrossRef] [PubMed]

187. Ali, L.; Subhan, F.; Ayaz, M.; ul Hassan, S.S.; Byeon, C.C.; Kim, J.S.; Bungau, S. Exfoliation of MoS$_2$ Quantum Dots: Recent Progress and Challenges. *Nanomaterials* **2022**, *12*, 3465. [CrossRef] [PubMed]

188. Xu, D.; Xu, P.; Zhu, Y.; Peng, W.; Li, Y.; Zhang, G. High Yield Exfoliation of WS$_2$ Crystals into 1−2 Layer Semiconducting Nanosheets and Efficient Photocatalytic Hydrogen Evolution from WS$_2$/CdS Nanorod Composites. *ACS Appl. Mater. Interfaces* **2018**, *10*, 2810–2818. [CrossRef] [PubMed]

189. Munkhbayar, G.; Palleschi, S.; Perrozzi, F.; Nardone, M.; Davaasambuu, J.; Ottaviano, L. A Study of Exfoliated Molybdenum Disulfide (MoS$_2$) Based on Raman and Photoluminescence Spectroscopy. *Solid. State Phenom.* **2018**, *271*, 40–46. [CrossRef]

190. Lei, Z.; Xu, S.; Wu, P. Ultra-Thin and Porous MoSe$_2$ Nanosheets: Facile Preparation and Enhanced Electrocatalytic Activity towards the Hydrogen Evolution Reaction. *Phys. Chem. Chem. Phys.* **2015**, *18*, 70–74. [CrossRef]

191. Hong, S.; Kim, S.M.; Song, W.G.; Hong, Y.; Kim, S. High-Mobility 2D Layered Semiconducting Transistors Based on Large-Area and Highly Crystalline CVD-Grown MoSe$_2$ for Flexible Electronics. In Proceedings of the 2016 IEEE Silicon Nanoelectronics Workshop, SNW 2016, Honolulu, HI, USA, 12–13 June 2016; pp. 56–57. [CrossRef]

192. Truong, Q.D.; Kempaiah Devaraju, M.; Nakayasu, Y.; Tamura, N.; Sasaki, Y.; Tomai, T.; Honma, I. Exfoliated MoS$_2$ and MoSe$_2$ Nanosheets by a Supercritical Fluid Process for a Hybrid Mg-Li-Ion Battery. *ACS Omega* **2017**, *2*, 2360–2367. [CrossRef] [PubMed]

193. Xu, K.; Wang, Z.; Du, X.; Safdar, M.; Jiang, C.; He, J. Atomic-Layer Triangular WSe$_2$ Sheets: Synthesis and Layer-Dependent Photoluminescence Property. *Nanotechnology* **2013**, *24*, 465705. [CrossRef] [PubMed]

194. Shackery, I.; Pezeshki, A.; Park, J.Y.; Palanivel, U.; Kwon, H.J.; Yoon, H.S.; Im, S.; Cho, J.S.; Jun, S.C. Few-Layered α-MoTe$_2$ Schottky Junction for a High Sensitivity Chemical-Vapour Sensor. *J. Mater. Chem. C Mater.* **2018**, *6*, 10714–10722. [CrossRef]

195. Joensen, P.; Frindt, R.F.; Morrison, S.R. Single-Layer MoS$_2$. *Mater. Res. Bull.* **1986**, *21*, 457–461. [CrossRef]

196. Gee, M.A.; Frindt, R.F.; Joensen, P.; Morrison, S.R. Inclusion Compounds of MoS$_2$. *Mater. Res. Bull.* **1986**, *21*, 543–549. [CrossRef]

197. Smith, R.J.; King, P.J.; Lotya, M.; Wirtz, C.; Khan, U.; De, S.; O'Neill, A.; Duesberg, G.S.; Grunlan, J.C.; Moriarty, G.; et al. Large-Scale Exfoliation of Inorganic Layered Compounds in Aqueous Surfactant Solutions. *Adv. Mater.* **2011**, *23*, 3944–3948. [CrossRef] [PubMed]

198. Frisenda, R.; Navarro-Moratalla, E.; Gant, P.; Pérez De Lara, D.; Jarillo-Herrero, P.; Gorbachev, R.V.; Castellanos-Gomez, A. Recent Progress in the Assembly of Nanodevices and van Der Waals Heterostructures by Deterministic Placement of 2D Materials. *Chem. Soc. Rev.* **2018**, *47*, 53–68. [CrossRef]

199. Yao, Y.; Tolentino, L.; Yang, Z.; Song, X.; Zhang, W.; Chen, Y.; Wong, C.P. High-Concentration Aqueous Dispersions of MoS$_2$. *Adv. Funct. Mater.* **2013**, *23*, 3577–3583. [CrossRef]

200. Zhu, S.; Gong, L.; Xie, J.; Gu, Z.; Zhao, Y.; Zhu, S.; Gong, L.J.; Xie, J.N.; Gu, Z.J.; Zhao, Y.L. Design, Synthesis, and Surface Modification of Materials Based on Transition-Metal Dichalcogenides for Biomedical Applications. *Small Methods* **2017**, *1*, 1700220. [CrossRef]

201. Ibrahem, M.A.; Lan, T.; Huang, J.K.; Chen, Y.; Wei, K.; Li, L.; Chu, C.W. High Quantity and Quality Few-Layers Transition Metal Disulfide Nanosheets from Wet-Milling Exfoliation. *RSC Adv.* **2013**, *3*, 13193–13202. [CrossRef]

202. Cunningham, G.; Lotya, M.; Cucinotta, C.S.; Sanvito, S.; Bergin, S.D.; Menzel, R.; Shaffer, M.S.P.; Coleman, J.N. Solvent Exfoliation of Transition Metal Dichalcogenides: Dispersibility of Exfoliated Nanosheets Varies Only Weakly between Compounds. *ACS Nano* **2012**, *6*, 3468–3480. [CrossRef] [PubMed]

203. Li, H.; Shi, Y.; Chiu, M.H.; Li, L.J. Emerging Energy Applications of Two-Dimensional Layered Transition Metal Dichalcogenides. *Nano Energy* **2015**, *18*, 293–305. [CrossRef]

204. Yuwen, L.; Yu, H.; Yang, X.; Zhou, J.; Zhang, Q.; Zhang, Y.; Luo, Z.; Su, S.; Wang, L. Rapid Preparation of Single-Layer Transition Metal Dichalcogenide Nanosheets via Ultrasonication Enhanced Lithium Intercalation. *Chem. Commun.* **2015**, *52*, 529–532. [CrossRef] [PubMed]

205. Nicolosi, V.; Chhowalla, M.; Kanatzidis, M.G.; Strano, M.S.; Coleman, J.N. Liquid Exfoliation of Layered Materials. *Science* **2013**, *340*, 1226419. [CrossRef]

206. Sharma, R.; Laishram, R.; Gupta, B.K. A Review on MX$_2$ (M = Mo, W and X = S, Se) Layered Material for Opto-Electronic Devices. *Adv. Nat. Sci. Nanosci. Nanotechnol. Rev.* **2022**, *4*, 023001. [CrossRef]

207. Sun, J.; Li, X.; Guo, W.; Zhao, M.; Fan, X.; Dong, Y.; Xu, C.; Deng, J.; Fu, Y. Synthesis Methods of Two-Dimensional MoS$_2$: A Brief Review. *Crystals* **2017**, *7*, 198. [CrossRef]

208. Tsai, H.; Heising, J.; Schindler, J.L.; Kannewurf, C.R.; Kanatzidis, M.G. Exfoliated—Restacked Phase of WS$_2$ as Pyridine, Ammonia, etc. This Intercalative Inertness Originates from the Prismatic Coordination Environment of Mo and W Centers (d 2 Configuration) Which Results in a Fully Occupied Valence Band Composed of d z. *Chem. Mater.* **1997**, *4756*, 879–882. [CrossRef]

209. Heising, J.; Kanatzidis, M.G.; State, M.; Uni, V.; Lansing, E.; May, R. V Exfoliated and Restacked MoS$_2$ and WS$_2$: Ionic or Neutral Species? Encapsulation and Ordering of Hard Electropositive Cations. *J. Am. Chem. Soc.* **1999**, *121*, 11720–11732. [CrossRef]

210. Oehrlein, G.S.; Metzler, D.; Li, C. Atomic Layer Etching at the Tipping Point: An Overview. *ECS J. Solid State Sci. Technol.* **2015**, *4*, N5041–N5053. [CrossRef]

211. He, T.; Wang, Z.; Zhong, F.; Fang, H.; Wang, P.; Hu, W. Etching Techniques in 2D Materials. *Adv. Mater. Technol.* **2019**, *4*, 1900064. [CrossRef]

212. Kim, K.S.; Kim, K.H.; Nam, Y.; Jeon, J.; Yim, S.; Singh, E.; Lee, J.Y.; Lee, S.J.; Jung, Y.S.; Yeom, G.Y.; et al. Atomic Layer Etching Mechanism of MoS$_2$ for Nanodevices. *ACS Appl. Mater. Interfaces* **2017**, *9*, 11967–11976. [CrossRef] [PubMed]

213. Zhu, H.; Qin, X.; Cheng, L.; Azcatl, A.; Kim, J.; Wallace, R.M. Remote Plasma Oxidation and Atomic Layer Etching of MoS$_2$. *ACS Appl. Mater. Interfaces* **2016**, *8*, 19119–19126. [CrossRef] [PubMed]

214. Chen, K.C.; Chu, T.W.; Wu, C.R.; Lee, S.C.; Lin, S.Y. Atomic Layer Etchings of Transition Metal Dichalcogenides with Post Healing Procedures: Equivalent Selective Etching of 2D Crystal Hetero-Structures. *2D Mater.* **2017**, *4*, 034001. [CrossRef]

215. Tagawa, M.; Yokota, K.; Matsumoto, K.; Suzuki, M.; Teraoka, Y.; Kitamura, A.; Belin, M.; Fontaine, J.; Martin, J.M. Space Environmental Effects on MoS$_2$ and Diamond-like Carbon Lubricating Films: Atomic Oxygen-Induced Erosion and Its Effect on Tribological Properties. *Surf. Coat. Technol.* **2007**, *202*, 1003–1010. [CrossRef]

216. Sha, Y.; Xiao, S.; Zhang, X.; Qin, F.; Gu, X. Layer-by-Layer Thinning of MoSe$_2$ by Soft and Reactive Plasma Etching Applied Surface Science Layer-by-Layer Thinning of MoSe$_2$ by Soft and Reactive Plasma Etching. *Appl. Surf. Sci. J.* **2017**, *411*, 182–188. [CrossRef]

217. Nipane, A.; Choi, M.S.; Sebastian, P.J.; Yao, K.; Borah, A.; Deshmukh, P.; Jung, Y.; Kim, B.; Rajendran, A.; Kwock, K.W.C.; et al. Damage-Free Atomic Layer Etch of WSe$_2$: A Platform for Fabricating Clean Two-Dimensional Devices. *ACS Appl. Mater. Interfaces* **2021**, *13*, 1930–1942. [CrossRef] [PubMed]

218. Le Thi, H.Y.; Dat Ngo, T.; Anh, N.; Phan, N.; Yoo, J.; Watanabe, K.; Taniguchi, T.; Aoki, N.; Bird, J.P.; Kim, G.-H.; et al. Self-Forming p–n Junction Diode Realized with WSe$_2$ Surface and Edge Dual Contacts. *Small* **2022**, *18*, 2204547. [CrossRef] [PubMed]

219. Lee, D.; Choi, Y.; Kim, J.; Kim, J. Recessed-Channel WSe$_2$ Field-Effect Transistor via Self-Terminated Doping and Layer-by-Layer Etching. *ACS Nano* **2022**, *16*, 8484–8492. [CrossRef]

220. Guo, S.; Yang, D.; Zhang, S.; Dong, Q.; Li, B.; Tran, N.; Li, Z.; Xiong, Y.; Zaghloul, M.E.; Guo, S.; et al. Development of a Cloud-Based Epidermal MoSe$_2$ Device for Hazardous Gas Sensing. *Adv. Funct. Mater.* **2019**, *29*, 1900138. [CrossRef]

221. Hemanjaneyulu, K.; Meersha, A.; Kumar, J.; Shrivastava, M. Unveiling Unintentional Fluorine Doping in TMDs During the Reactive Ion Etching: Root Cause Analysis, Physical Insights, and Solution. *IEEE Trans. Electron. Devices* **2022**, *69*, 1956–1963. [CrossRef]

222. Chen, X.; Zhang, L.; Chen, S. Large Area CVD Growth of Graphene. *Synth. Met.* **2015**, *210*, 95–108. [CrossRef]

223. Song, X.; Gao, J.; Nie, Y.; Gao, T.; Sun, J.; Ma, D.; Li, Q.; Chen, Y.; Jin, C.; Bachmatiuk, A.; et al. Chemical Vapor Deposition Growth of Large-Scale Hexagonal Boron Nitride with Controllable Orientation. *Nano Res.* **2015**, *8*, 3164–3176. [CrossRef]

224. Lin, Y.C.; Ghosh, R.K.; Addou, R.; Lu, N.; Eichfeld, S.M.; Zhu, H.; Li, M.Y.; Peng, X.; Kim, M.J.; Li, L.J.; et al. Atomically Thin Resonant Tunnel Diodes Built from Synthetic van Der Waals Heterostructures. *Nat. Commun.* **2015**, *6*, 7311. [CrossRef] [PubMed]

225. Liu, J.; Zeng, M.; Wang, L.; Chen, Y.; Xing, Z.; Zhang, T.; Liu, Z.; Zuo, J.; Nan, F.; Mendes, R.G.; et al. Ultrafast Self-Limited Growth of Strictly Monolayer WSe$_2$ Crystals. *Small* **2016**, *12*, 5741–5749. [CrossRef] [PubMed]

226. Aras, F.G.; Yilmaz, A.; Tasdelen, H.G.; Ozden, A.; Ay, F.; Perkgoz, N.K.; Yeltik, A. A Review on Recent Advances of Chemical Vapor Deposition Technique for Monolayer Transition Metal Dichalcogenides (MX$_2$: Mo, W, S, Se, Te). *Mater. Sci. Semicond. Process* **2022**, *148*, 106829. [CrossRef]

227. Jian, J.; Chang, H.; Xu, T. Structure and Properties of Single-Layer MoS$_2$ for Nano-Photoelectric Devices. *Materials* **2019**, *12*, 198. [CrossRef] [PubMed]

228. Zhang, L.; Liu, K.; Wong, A.B.; Kim, J.; Hong, X.; Liu, C.; Cao, T.; Louie, S.G.; Wang, F.; Yang, P. Three-Dimensional Spirals of Atomic Layered MoS$_2$. *Nano Lett.* **2014**, *14*, 6418–6423. [CrossRef] [PubMed]

229. Vikraman, D.; Hussain, S.; Akbar, K.; Adaikalam, K.; Lee, S.H.; Chun, S.H.; Jung, J.; Kim, H.S.; Park, H.J. Facile Synthesis of Molybdenum Diselenide Layers for High-Performance Hydrogen Evolution Electrocatalysts. *ACS Omega* **2018**, *3*, 5799–5807. [CrossRef] [PubMed]

230. Tsang, C.F.; Ledina, M.A.; Stickney, J.L. Molybdenum Diselenide Formation Using Electrochemical Atomic Layer Deposition (E-ALD). *J. Electroanal. Chem.* **2017**, *793*, 242–249. [CrossRef]

231. Liu, B.; Fathi, M.; Chen, L.; Abbas, A.; Ma, Y.; Zhou, C. Chemical Vapor Deposition Growth of Monolayer WSe$_2$ with Tunable Device Characteristics and Growth Mechanism Study. *ACS Nano* **2015**, *9*, 6119–6127. [CrossRef]

232. Gong, Y.; Lei, S.; Ye, G.; Li, B.; He, Y.; Keyshar, K.; Zhang, X.; Wang, Q.; Lou, J.; Liu, Z.; et al. Two-Step Growth of Two-Dimensional WSe$_2$/MoSe$_2$ Heterostructures. *Nano Lett.* **2015**, *15*, 6135–6141. [CrossRef]

233. Sassi, L.M.; Krishnamoorthy, A.; Hachtel, J.A.; Susarla, S.; Apte, A.; Castro-Pardo, S.; Ajnsztajn, A.; Vajtai, R.; Vashishta, P.; Tiwary, C.S.; et al. Low Temperature CVD Growth of WSe$_2$ Enabled by Moisture-Assisted Defects in the Precursor Powder. *2D Mater.* **2022**, *9*, 045026. [CrossRef]

234. Feng, Q.; Zhu, M.; Zhao, Y.; Liu, H.; Li, M.; Zheng, J.; Xu, H.; Jiang, Y. Chemical Vapor Deposition Growth of Sub-Centimeter Single Crystal WSe$_2$ Monolayer by NaCl-Assistant. *Nanotechnology* **2019**, *30*, 034001. [CrossRef]

235. Bishop, C.A. Atomic Layer Deposition. In *Vacuum Deposition onto Webs, Films and Foils*; William Andrew: Norwich, NY, USA, 2011; pp. 331–336. [CrossRef]

236. Hynek, D.J.; Onder, E.; Hart, J.L.; Jin, G.; Wang, M.; Singhania, R.M.; Davis, B.; Strandwitz, N.C.; Cha, J.J.; Hynek, D.J.; et al. Substrate Effects on Growth Dynamics of WTe$_2$ Thin Films. *Adv. Mater. Interfaces* **2023**, *10*, 2202397. [CrossRef]

237. Cho, S.J.; Uddin, M.J.; Alaboina, P. Review of Nanotechnology for Cathode Materials in Batteries. In *Emerging Nanotechnologies in Rechargeable Energy Storage Systems*; Elsevier: Amsterdam, The Netherlands, 2017; pp. 83–129. [CrossRef]

238. Leskelä, M.; Niinistö, J.; Ritala, M. Atomic Layer Deposition. *Compr. Mater. Process.* **2014**, *4*, 101–123. [CrossRef]

239. Xie, L.; Abliz, D.; Li, D. Thin Film Coating for Polymeric Micro Parts. *Compr. Mater. Process.* **2014**, *7*, 157–170. [CrossRef]

240. George, S.M. Atomic Layer Deposition: An Overview. *Chem. Rev.* **2010**, *110*, 111–131. [CrossRef]

241. Kanarik, K.J.; Lill, T.; Hudson, E.A. Overview of Atomic Layer Etching in the Semiconductor Industry. *J. Vac. Sci. Technol. A* **2015**, *33*, 020802. [CrossRef]

242. Zhang, Y.; Wang, Z.; Feng, J.; Ming, S.; Qu, F.; Xia, Y.; He, M.; Hu, Z.; Wang, J. Synthesis and Electromagnetic Transport of Large-Area 2D WTe$_2$ Thin Film. *J. Semicond.* **2022**, *43*, 102002. [CrossRef]

243. Martella, C.; Quadrelli, A.; Tummala, P.P.; Lenardi, C.; Mantovan, R.; Lamperti, A.; Molle, A. Tailoring the Phase in Nanoscale MoTe$_2$ Grown by Barrier-Assisted Chemical Vapor Deposition. *Cryst. Growth Des.* **2021**, *21*, 2970–2976. [CrossRef]

244. Xu, X.; Li, X.; Liu, K.; Li, J.; Feng, Q.; Zhou, L.; Cui, F.; Liang, X.; Lei, Z.; Liu, Z.; et al. Thermodynamics and Kinetics Synergetic Phase-Engineering of Chemical Vapor Deposition Grown Single Crystal MoTe$_2$ Nanosheets. *Cryst. Growth Des.* **2018**, *18*, 2844–2850. [CrossRef]

245. Pinto, F.M.; Suzuki, V.Y.; Silva, R.C.; La Porta, F.A. Oxygen Defects and Surface Chemistry of Reducible Oxides. *Front. Mater.* **2019**, *6*, 260. [CrossRef]

246. Zou, X.; Liu, Y.; Yakobson, B.I. Predicting Dislocations and Grain Boundaries in Two-Dimensional Metal-Disulfides from the First Principles. *Nano Lett.* **2013**, *13*, 253–258. [CrossRef] [PubMed]

247. Pantelides, S.T. The Electronic Structure of Impurities and Other Point Defects in Semiconductors. *Rev. Mod. Phys.* **1978**, *50*, 797. [CrossRef]

248. Zarbin, A.J.G. Liquid–Liquid Interfaces: A Unique and Advantageous Environment to Prepare and Process Thin Films of Complex Materials. *Mater. Horiz.* **2021**, *8*, 1409–1432. [CrossRef]

249. Cheng, J.; Wang, C.; Zou, X.; Liao, L. Recent Advances in Optoelectronic Devices Based on 2D Materials and Their Heterostructures. *Adv. Opt. Mater.* **2019**, *7*, 1800441. [CrossRef]

250. Zhang, X.; Xue, M.; Yang, X.; Luo, G.; Yang, F. Hydrothermal Synthesis and Tribological Properties of MoSe$_2$ Nanoflowers. *Micro Nano Lett.* **2015**, *10*, 339–342. [CrossRef]

251. Vattikuti, S.V.P.; Byon, C.; Chitturi, V. Selective Hydrothermally Synthesis of Hexagonal WS$_2$ Platelets and Their Photocatalytic Performance under Visible Light Irradiation. *Superlattices Microstruct.* **2016**, *94*, 39–50. [CrossRef]

252. Wen, R.; Wei, A.; Tao, L.; Luo, D.; Liu, J.; Yang, Y.; Xiao, Z.; Liu, Z.; Zhao, Y. Hydrothermal Synthesis of WSe$_2$ Films and Their Application in High-Performance Photodetectors. *Appl. Phys. A Mater. Sci. Process* **2018**, *124*, 634. [CrossRef]

253. Chakravarty, D.; Late, D.J. Microwave and Hydrothermal Syntheses of WSe$_2$ Micro/Nanorods and Their Application in Supercapacitors. *RSC Adv.* **2015**, *5*, 21700–21709. [CrossRef]

254. Wang, X.; Chen, Y.; Zheng, B.; Qi, F.; He, J.; Li, Q.; Li, P.; Zhang, W. Graphene-like WSe$_2$ Nanosheets for Efficient and Stable Hydrogen Evolution. *J. Alloys Compd.* **2017**, *691*, 698–704. [CrossRef]

255. Yuvasravan, R.; Apsana, G.; George, P.P.; Genish, I.; Maklouf, S.B.D.; Koltypin, Y.; Gedanken, A. Synthesis of WS$_2$ and WSe$_2$ Nanowires on Stainless Steel Coupon by Reaction under Autogenic Pressure at Elevated Temperature Method. *Appl. Nanosci.* **2016**, *6*, 855–862. [CrossRef]

256. Zou, H.Y.; Fang, L.; Yu, G.; Wang, D. Nanocrystalline WSe$_2$ Excels at High-Performance Anode for Na Storage via a Facile One-Pot Hydrothermal Method. *Tungsten* **2022**, *6*, 248–258. [CrossRef]

257. Chauhan, I.; Kaur, M.; Singh, K.; Kumar, A. Two-Dimensional Tungsten Ditelluride (WTe$_2$) via Low-Temperature Single Step Thermo-Chemical Approach. *Appl. Phys. A Mater. Sci. Process* **2020**, *126*, 747. [CrossRef]

258. Xu, H.; Sun, L.; Li, W.; Gao, M.; Zhou, Q.; Li, P.; Yang, S.; Lin, J. Facile Synthesis of Hierarchical G-C$_3$N$_4$@WS Composite as Lithium-Ion Battery Anode. *Chem. Eng. J.* **2022**, *435*, 135129. [CrossRef]

259. Wu, M.; Xiao, Y.; Zeng, Y.; Zhou, Y.; Zeng, X.; Zhang, L.; Liao, W. Synthesis of Two-Dimensional Transition Metal Dichalcogenides for Electronics and Optoelectronics. *InfoMat* **2021**, *3*, 362–396. [CrossRef]

260. Oliveira, M.H.; Schumann, T.; Gargallo-Caballero, R.; Fromm, F.; Seyller, T.; Ramsteiner, M.; Trampert, A.; Geelhaar, L.; Lopes, J.M.J.; Riechert, H. Mono- and Few-Layer Nanocrystalline Graphene Grown on Al$_2$O$_3$ (0 0 0 1) by Molecular Beam Epitaxy. *Carbon* **2013**, *56*, 339–350. [CrossRef]

261. Nakhaie, S.; Wofford, J.M.; Schumann, T.; Jahn, U.; Ramsteiner, M.; Hanke, M.; Lopes, J.M.J.; Riechert, H. Synthesis of Atomically Thin Hexagonal Boron Nitride Films on Nickel Foils by Molecular Beam Epitaxy. *Appl. Phys. Lett.* **2015**, *106*, 213108. [CrossRef]

262. Fu, D.; Zhao, X.; Zhang, Y.Y.; Li, L.; Xu, H.; Jang, A.R.; Yoon, S.I.; Song, P.; Poh, S.M.; Ren, T.; et al. Molecular Beam Epitaxy of Highly Crystalline Monolayer Molybdenum Disulfide on Hexagonal Boron Nitride. *J. Am. Chem. Soc.* **2017**, *139*, 9392–9400. [CrossRef]

263. Diaz, H.C.; Chaghi, R.; Ma, Y.; Batzill, M. Molecular Beam Epitaxy of the van Der Waals Heterostructure MoTe$_2$ on MoS$_2$: Phase, Thermal, and Chemical Stability. *2D Mater.* **2015**, *2*, 044010. [CrossRef]

264. Wofford, J.M.; Nakhaie, S.; Krause, T.; Liu, X.; Ramsteiner, M.; Hanke, M.; Riechert, H.; Lopes, J.M.J. A Hybrid MBE-Based Growth Method for Large-Area Synthesis of Stacked Hexagonal Boron Nitride/Graphene Heterostructures. *Sci. Rep.* **2017**, *7*, 43644. [CrossRef] [PubMed]

265. Novoselov, K.S.; Mishchenko, A.; Carvalho, A.; Castro Neto, A.H. 2D Materials and van Der Waals Heterostructures. *Science* **2016**, *353*, aac9439. [CrossRef]

266. Jadriško, V.; Radatović, B.; Pielić, B.; Gadermaier, C.; Kralj, M.; Vujičić, N. Structural and Optical Characterization of Nanometer Sized MoS$_2$/Graphene Heterostructures for Potential Use in Optoelectronic Devices. *FlatChem* **2022**, *34*, 100397. [CrossRef]

267. Roy, A.; Movva, H.C.P.; Satpati, B.; Kim, K.; Dey, R.; Rai, A.; Pramanik, T.; Guchhait, S.; Tutuc, E.; Banerjee, S.K. Structural and Electrical Properties of MoTe$_2$ and MoSe$_2$ Grown by Molecular Beam Epitaxy. *ACS Appl. Mater. Interfaces* **2016**, *8*, 7396–7402. [CrossRef]

268. Zhang, L.; Yang, T.; He, X.; Zhang, W.; Vinai, G.; Tang, C.S.; Yin, X.; Torelli, P.; Feng, Y.P.; Wong, P.K.J.; et al. Molecular Beam Epitaxy of Two-Dimensional Vanadium-Molybdenum Diselenide Alloys. *ACS Nano* **2020**, *14*, 11140–11149. [CrossRef] [PubMed]
269. Raza, A.; Hassan, J.Z.; Ikram, M.; Ali, S.; Farooq, U.; Khan, Q.; Maqbool, M. Advances in Liquid-Phase and Intercalation Exfoliations of Transition Metal Dichalcogenides to Produce 2D Framework. *Adv. Mater. Interfaces* **2021**, *8*, 2002205. [CrossRef]
270. Witomska, S.; Leydecker, T.; Ciesielski, A.; Samorì, P.; Witomska, S.; Leydecker, T.; Ciesielski, A.; Samorì, P. Production and Patterning of Liquid Phase–Exfoliated 2D Sheets for Applications in Optoelectronics. *Adv. Funct. Mater.* **2019**, *29*, 1901126. [CrossRef]
271. Yi, K.; Liu, D.; Chen, X.; Yang, J.; Wei, D.D.; Liu, Y.; Wei, D.D. Plasma-Enhanced Chemical Vapor Deposition of Two-Dimensional Materials for Applications. *Acc. Chem. Res.* **2021**, *54*, 1011–1022. [CrossRef]
272. Cai, Z.; Liu, B.; Zou, X.; Cheng, H.M. Chemical Vapor Deposition Growth and Applications of Two-Dimensional Materials and Their Heterostructures. *Chem. Rev.* **2018**, *118*, 6091–6133. [CrossRef]
273. Ludwiczak, K.; Dąbrowska, A.K.; Binder, J.; Tokarczyk, M.; Iwański, J.; Kurowska, B.; Turczyński, J.; Kowalski, G.; Bożek, R.; Stępniewski, R.; et al. Heteroepitaxial Growth of High Optical Quality, Wafer-Scale van Der Waals Heterostrucutres. *ACS Appl. Mater. Interfaces* **2021**, *13*, 47904–47911. [CrossRef]
274. Wan, W.; Li, X.; Li, X.; Xu, B.; Zhan, L.; Zhao, Z.; Zhang, P.; Wu, S.Q.; Zhu, Z.Z.; Huang, H.; et al. Interlayer Coupling of a Direct van Der Waals Epitaxial MoS_2/Graphene Heterostructure. *RSC Adv.* **2015**, *6*, 323–330. [CrossRef]
275. Dong, M.; Zhang, H.; Tzounis, L.; Santagiuliana, G.; Bilotti, E.; Papageorgiou, D.G. Multifunctional Epoxy Nanocomposites Reinforced by Two-Dimensional Materials: A Review. *Carbon* **2021**, *185*, 57–81. [CrossRef]
276. Eksik, O.; Gao, J.; Shojaee, S.A.; Thomas, A.; Chow, P.; Bartolucci, S.F.; Lucca, D.A.; Koratkar, N. Epoxy Nanocomposites with Two-Dimensional Transition Metal Dichalcogenide Additives. *ACS Nano* **2014**, *8*, 5282–5289. [CrossRef]
277. Wang, Q.; Chen, J.; Zhang, Y.; Hu, L.; Liu, R.; Cong, C.; Qiu, Z.J. Precise Layer Control of $MoTe_2$ by Ozone Treatment. *Nanomaterials* **2019**, *9*, 756. [CrossRef] [PubMed]
278. Eidsvåg, H.; Vajeeston, P.; Velauthapillai, D. Doped MoS_2 Polymorph for an Improved Hydrogen Evolution Reaction. *ACS Omega* **2023**, *8*, 26263–26275. [CrossRef]
279. Rosenberger, M.R.; Chuang, H.J.; McCreary, K.M.; Li, C.H.; Jonker, B.T. Electrical Characterization of Discrete Defects and Impact of Defect Density on Photoluminescence in Monolayer WS_2. *ACS Nano* **2018**, *12*, 1793–1800. [CrossRef]
280. Zheng, D.; Yu, L.; Liu, W.; Dai, X.; Niu, X.; Fu, W.; Shi, W.; Wu, F.; Cao, X. Structural Advantages and Enhancement Strategies of Heterostructure Water-Splitting Electrocatalysts. *Cell Rep. Phys. Sci.* **2021**, *2*, 100443. [CrossRef]
281. Lin, Z.; Carvalho, B.R.; Kahn, E.; Lv, R.; Rao, R.; Terrones, H.; Pimenta, M.A.; Terrones, M. Defect Engineering of Two-Dimensional Transition Metal Dichalcogenides. *2D Mater.* **2016**, *3*, 022002. [CrossRef]
282. Wang, X.; Lu, Q.; Sun, Y.; Liu, K.; Cui, J.; Lu, C.; Dai, H. Fabrication of Novel P-n-p Heterojunctions Ternary WSe_2/In_2S_3/$ZnIn_2S_4$ to Enhance Visible-Light Photocatalytic Activity. *J. Environ. Chem. Eng.* **2022**, *10*, 108354. [CrossRef]
283. Xu, A.J.; Tu, W.; Shen, S.; Lin, Z.; Gao, N.; Zhong, W. $BiVO_4$@MoS_2 Core-Shell Heterojunction with Improved Photocatalytic Activity for Discoloration of Rhodamine B. *Appl. Surf. Sci.* **2020**, *528*, 146949. [CrossRef]
284. Georgiou, T.; Jalil, R.; Belle, B.D.; Britnell, L.; Gorbachev, R.V.; Morozov, S.V.; Kim, Y.J.; Gholinia, A.; Haigh, S.J.; Makarovsky, O.; et al. Vertical Field-Effect Transistor Based on Graphene-WS_2 Heterostructures for Flexible and Transparent Electronics. *Nat. Nanotechnol.* **2013**, *8*, 100–103. [CrossRef] [PubMed]
285. Selamneni, V.; Sahatiya, P. Mixed Dimensional Transition Metal Dichalcogenides (TMDs) VdW Heterostructure Based Photodetectors: A Review. *Microelectron. Eng.* **2023**, *269*, 111926. [CrossRef]
286. Dong, R.; Kuljanishvili, I. Review Article: Progress in Fabrication of Transition Metal Dichalcogenides Heterostructure Systems. *J. Vac. Sci. Technol. B Nanotechnol. Microelectron. Mater. Process. Meas. Phenom.* **2017**, *35*, 030803. [CrossRef]
287. Kumar, P.; Viswanath, B. Horizontally and Vertically Aligned Growth of Strained MoS_2 Layers with Dissimilar Wetting and Catalytic Behaviors. *CrystEngComm* **2017**, *19*, 5068–5078. [CrossRef]
288. Lin, Y.-C. *Properties of Synthetic Two-Dimensional Materials and Heterostructures*; ProQuest LLC: Ann Arbor, MI, USA, 2018. [CrossRef]
289. Davies, F.H.; Mehlich, K.; Busse, C.; Krasheninnikov, A.V. What Governs the Atomic Structure of the Interface between 2D Transition Metal Dichalcogenides in Lateral Heterostructures? *2D Mater.* **2023**, *11*, 015003. [CrossRef]
290. Sun, M.; Chou, J.-P.; Ren, Q.; Zhao, Y.; Yu, J.; Tang, W. Tunable Schottky Barrier in van Der Waals Heterostructures of Graphene and G-GaN. *Appl. Phys. Lett.* **2017**, *110*, 173105. [CrossRef]
291. Zhang, C.; Gong, C.; Nie, Y.; Min, K.-A.; Liang, C.; Oh, Y.J.; Zhang, H.; Wang, W.; Hong, S.; Colombo, L.; et al. Systematic Study of Electronic Structure and Band Alignment of Monolayer Transition Metal Dichalcogenides in Van Der Waals Heterostructures. *2D Mater.* **2016**, *4*, 015026. [CrossRef]
292. You, B.; Wang, X.; Zheng, Z.; Mi, W. Black Phosphorene/Monolayer Transition-Metal Dichalcogenides as Two Dimensional van Der Waals Heterostructures: A First-Principles Study. *Phys. Chem. Chem. Phys.* **2016**, *18*, 7381–7388. [CrossRef] [PubMed]
293. Sun, M.; Chou, J.-P.; Yu, J.; Tang, W. Effects of Structural Imperfection on the Electronic Properties of Graphene/WSe_2 Heterostructures. *J. Mater. Chem. C* **2017**, *5*, 10383–10390. [CrossRef]
294. Koda, D.S.; Bechstedt, F.; Marques, M.; Teles, L.K. Tuning Electronic Properties and Band Alignments of Phosphorene Combined with $MoSe_2$ and WSe_2. *J. Phys. Chem. C* **2017**, *121*, 3862–3869. [CrossRef]

295. Wang, S.; Tian, H.; Ren, C.; Yu, J.; Sun, M. Electronic and Optical Properties of Heterostructures Based on Transition Metal Dichalcogenides and Graphene-like Zinc Oxide. *Sci. Rep.* **2018**, *8*, 12009. [CrossRef]

296. Özçelik, V.O.; Azadani, J.G.; Yang, C.; Koester, S.J.; Low, T. Band Alignment of Two-Dimensional Semiconductors for Designing Heterostructures with Momentum Space Matching. *Phys. Rev. B* **2016**, *94*, 035125. [CrossRef]

297. Li, X.; Garlisi, C.; Guan, Q.; Anwer, S.; Al-Ali, K.; Palmisano, G.; Zheng, L. A Review of Material Aspects in Developing Direct Z-Scheme Photocatalysts. *Mater. Today* **2021**, *47*, 75–107. [CrossRef]

298. Nakamura, S.; Senoh, M.; Iwasa, N.; Shin-ichi Nagahama, S.N. High-Brightness InGaN Blue, Green and Yellow Light-Emitting Diodes with Quantum Well Structures. *Jpn. J. Appl. Phys.* **1995**, *34*, L797. [CrossRef]

299. Li, M.Y.; Chen, C.H.; Shi, Y.; Li, L.J. Heterostructures Based on Two-Dimensional Layered Materials and Their Potential Applications. *Mater. Today* **2016**, *19*, 322–335. [CrossRef]

300. Azadmanjiri, J.; Srivastava, V.K.; Kumar, P.; Sofer, Z.; Min, J.; Gong, J. Graphene-Supported 2D Transition Metal Dichalcogenide van Der Waals Heterostructures. *Appl. Mater. Today* **2020**, *19*, 100600. [CrossRef]

301. Zhang, K.; Feng, S.; Kang, S.; Wu, Y.; Zhang, M.; Wang, Q.; Tao, Z.; Fan, Y.; Lu, W. Hybrid Structure of PbS QDs and Verticallyfew-Layer MoS_2 nanosheets Array for Broadband Photodetector. *Nanotechnology* **2021**, *32*, 145602. [CrossRef] [PubMed]

302. Kim, Y.; Choi, D.; Woo, W.J.; Lee, J.B.; Ryu, G.H.; Lim, J.H.; Lee, S.; Lee, Z.; Im, S.; Ahn, J.H.; et al. Synthesis of Two-Dimensional MoS_2/Graphene Heterostructure by Atomic Layer Deposition Using MoF_6 Precursor. *Appl. Surf. Sci.* **2019**, *494*, 591–599. [CrossRef]

303. Subramanian, S.; Campbell, Q.T.; Moser, S.K.; Kiemle, J.; Zimmermann, P.; Seifert, P.; Sigger, F.; Sharma, D.; Al-Sadeg, H.; Labella, M.; et al. Photophysics and Electronic Structure of Lateral Graphene/MoS_2 and Metal/MoS_2 Junctions. *ACS Nano* **2020**, *14*, 16663–16671. [CrossRef]

304. Silveira, J.F.R.V.; Besse, R.; Da Silva, J.L.F. Stacking Order Effects on the Electronic and Optical Properties of Graphene/Transition Metal Dichalcogenide Van Der Waals Heterostructures. *ACS Appl. Electron. Mater.* **2021**, *3*, 1671–1680. [CrossRef]

305. Ranjith Kumar, D.; Shanmugam Ranjith, K.; Manoharan, M.; Haldorai, Y.; Han, Y.K.; Hwan Oh, T.; Thangavelu Rajendra Kumar, R. Sulfur Vacancies Promoted Highly Efficient Visible Light Photocatalytic Degradation of Antibiotic and Phenolic Pollutants over WS_2/RGO Heterostructure. *Sep. Purif. Technol.* **2024**, *329*, 125172. [CrossRef]

306. Xu, C.; Yong, H.W.; He, J.; Long, R.; Cadore, A.R.; Paradisanos, I.; Ott, A.K.; Soavi, G.; Tongay, S.; Cerullo, G.; et al. Weak Distance Dependence of Hot-Electron-Transfer Rates at the Interface between Monolayer MoS_2 and Gold. *ACS Nano* **2021**, *15*, 819–828. [CrossRef] [PubMed]

307. Geim, A.K.; Grigorieva, I.V. Van Der Waals Heterostructures. *Nature* **2013**, *499*, 419–425. [CrossRef] [PubMed]

308. Jeong, M.H.; Ra, H.S.; Lee, S.H.; Kwak, D.H.; Ahn, J.; Yun, W.S.; Lee, J.D.; Chae, W.S.; Hwang, D.K.; Lee, J.S. Multilayer WSe_2/MoS_2 Heterojunction Phototransistors through Periodically Arrayed Nanopore Structures for Bandgap Engineering. *Adv. Mater.* **2022**, *34*, 2108412. [CrossRef] [PubMed]

309. Cheng, R.; Li, D.; Zhou, H.; Wang, C.; Yin, A.; Jiang, S.; Liu, Y.; Chen, Y.; Huang, Y.; Duan, X. Electroluminescence and Photocurrent Generation from Atomically Sharp WSe_2/MoS_2 Heterojunction p–n Diodes. *Nano Lett.* **2014**, *14*, 5590–5597. [CrossRef] [PubMed]

310. Lee, C.H.; Lee, G.H.; Van Der Zande, A.M.; Chen, W.; Li, Y.; Han, M.; Cui, X.; Arefe, G.; Nuckolls, C.; Heinz, T.F.; et al. Atomically Thin p–n Junctions with van Der Waals Heterointerfaces. *Nat. Nanotechnol.* **2014**, *9*, 676–681. [CrossRef] [PubMed]

311. Liu, Y.; Weiss, N.O.; Duan, X.; Cheng, H.C.; Huang, Y.; Duan, X. Van Der Waals Heterostructures and Devices. *Nat. Rev. Mater.* **2016**, *1*, 16042. [CrossRef]

312. Liu, Z.; Song, L.; Zhao, S.; Huang, J.; Ma, L.; Zhang, J.; Lou, J.; Ajayan, P.M. Direct Growth of Graphene/Hexagonal Boron Nitride Stacked Layers. *Nano Lett.* **2011**, *11*, 2032–2037. [CrossRef] [PubMed]

313. Yan, Z.; Peng, Z.; Sun, Z.; Yao, J.; Zhu, Y.; Liu, Z.; Ajayan, P.M.; Tour, J.M. Growth of Bilayer Graphene on Insulating Substrates. *ACS Nano* **2011**, *5*, 8187–8192. [CrossRef]

314. Shi, Y.; Zhou, W.; Lu, A.Y.; Fang, W.; Lee, Y.H.; Hsu, A.L.; Kim, S.M.; Kim, K.K.; Yang, H.Y.; Li, L.J.; et al. Van Der Waals Epitaxy of MoS_2 Layers Using Graphene as Growth Templates. *Nano Lett.* **2012**, *12*, 2784–2791. [CrossRef]

315. McGilly, L.J.; Kerelsky, A.; Finney, N.R.; Shapovalov, K.; Shih, E.M.; Ghiotto, A.; Zeng, Y.; Moore, S.L.; Wu, W.; Bai, Y.; et al. Visualization of Moiré Superlattices. *Nat. Nanotechnol.* **2020**, *15*, 580–584. [CrossRef] [PubMed]

316. Hamer, M.J.; Giampietri, A.; Kandyba, V.; Genuzio, F.; Menteş, T.O.; Locatelli, A.; Gorbachev, R.V.; Barinov, A.; Mucha-Kruczyński, M. Moiré Superlattice Effects and Band Structure Evolution in Near-30-Degree Twisted Bilayer Graphene. *ACS Nano* **2022**, *16*, 1954–1962. [CrossRef] [PubMed]

317. Smoleński, T.; Dolgirev, P.E.; Kuhlenkamp, C.; Popert, A.; Shimazaki, Y.; Back, P.; Lu, X.; Kroner, M.; Watanabe, K.; Taniguchi, T.; et al. Signatures of Wigner Crystal of Electrons in a Monolayer Semiconductor. *Nature* **2021**, *595*, 53–57. [CrossRef]

318. Zhou, Y.; Sung, J.; Brutschea, E.; Esterlis, I.; Wang, Y.; Scuri, G.; Gelly, R.J.; Heo, H.; Taniguchi, T.; Watanabe, K.; et al. Bilayer Wigner Crystals in a Transition Metal Dichalcogenide Heterostructure. *Nature* **2021**, *595*, 48–52. [CrossRef] [PubMed]

319. Chu, Z.; Regan, E.C.; Ma, X.; Wang, D.; Xu, Z.; Utama, M.I.B.; Yumigeta, K.; Blei, M.; Watanabe, K.; Taniguchi, T.; et al. Nanoscale Conductivity Imaging of Correlated Electronic States in WSe_2/WS_2 Moiré Superlattices. *Phys. Rev. Lett.* **2020**, *125*, 186803. [CrossRef] [PubMed]

320. Regan, E.C.; Wang, D.; Jin, C.; Bakti Utama, M.I.; Gao, B.; Wei, X.; Zhao, S.; Zhao, W.; Zhang, Z.; Yumigeta, K.; et al. Mott and Generalized Wigner Crystal States in WSe_2/WS_2 Moiré Superlattices. *Nature* **2020**, *579*, 359–363. [CrossRef] [PubMed]

321. Tang, Y.; Li, L.; Li, T.; Xu, Y.; Liu, S.; Barmak, K.; Watanabe, K.; Taniguchi, T.; MacDonald, A.H.; Shan, J.; et al. Simulation of Hubbard Model Physics in WSe$_2$/WS$_2$ Moiré Superlattices. *Nature* **2020**, *579*, 353–358. [CrossRef]

322. Xu, Y.; Liu, S.; Rhodes, D.A.; Watanabe, K.; Taniguchi, T.; Hone, J.; Elser, V.; Mak, K.F.; Shan, J. Correlated Insulating States at Fractional Fillings of Moiré Superlattices. *Nature* **2020**, *587*, 214–218. [CrossRef] [PubMed]

323. Huang, X.; Wang, T.; Miao, S.; Wang, C.; Li, Z.; Lian, Z.; Taniguchi, T.; Watanabe, K.; Okamoto, S.; Xiao, D.; et al. Correlated Insulating States at Fractional Fillings of the WS$_2$/WSe$_2$ Moiré Lattice. *Nat. Phys.* **2021**, *17*, 715–719. [CrossRef]

324. Miao, S.; Wang, T.; Huang, X.; Chen, D.; Lian, Z.; Wang, C.; Blei, M.; Taniguchi, T.; Watanabe, K.; Tongay, S.; et al. Strong Interaction between Interlayer Excitons and Correlated Electrons in WSe$_2$/WS$_2$ Moiré Superlattice. *Nat. Commun.* **2021**, *12*, 3608. [CrossRef]

325. Wang, L.; Shih, E.M.; Ghiotto, A.; Xian, L.; Rhodes, D.A.; Tan, C.; Claassen, M.; Kennes, D.M.; Bai, Y.; Kim, B.; et al. Correlated Electronic Phases in Twisted Bilayer Transition Metal Dichalcogenides. *Nat. Mater.* **2020**, *19*, 861–866. [CrossRef] [PubMed]

326. Chen, D.; Lian, Z.; Huang, X.; Su, Y.; Rashetnia, M.; Yan, L.; Blei, M.; Taniguchi, T.; Watanabe, K.; Tongay, S.; et al. Tuning Moiré Excitons and Correlated Electronic States through Layer Degree of Freedom. *Nat. Commun.* **2022**, *13*, 4810. [CrossRef] [PubMed]

327. Li, R.; Zhou, Y.; Wang, X.; Wang, L.; Ning, P.; Tao, L.; Cai, J. Removal of Elemental Mercury by Photocatalytic Oxidation over La$_2$O$_3$/Bi$_2$O$_3$ Composite. *J. Environ. Sci.* **2021**, *102*, 384–397. [CrossRef] [PubMed]

328. Zhou, Q.; Duan, Y.F.; Hong, Y.G.; Zhu, C.; She, M.; Zhang, J.; Wei, H.Q. Experimental and Kinetic Studies of Gas-Phase Mercury Adsorption by Raw and Bromine Modified Activated Carbon. *Fuel Process. Technol.* **2015**, *134*, 325–332. [CrossRef]

329. Xie, C.; Xu, L.; Ye, X.; Xia, Y.; Gang, R.; Ye, Q. Composites of MoS$_2$ Nanosheets and Graphitic Carbon Nitride Nanosheets for Photocatalytic Mercury Removal. *ACS Appl. Nano Mater.* **2021**, *4*, 11861–11869. [CrossRef]

330. Ruziwa, D.T.; Oluwalana, A.E.; Mupa, M.; Meili, L.; Selvasembian, R.; Nindi, M.M.; Sillanpaa, M.; Gwenzi, W.; Chaukura, N. Pharmaceuticals in Wastewater and Their Photocatalytic Degradation Using Nano-Enabled Photocatalysts. *J. Water Process Eng.* **2023**, *54*, 103880. [CrossRef]

331. Gnanaguru, M.V.L.; Naushad, M.; Tatarchuk, T.; Ghangrekar, M.M.; Chowdhury, S. One-Step Calcination Synthesis of 2D/2D g-C$_3$N$_4$/WS$_2$ van Der Waals Heterojunction for Visible Light-Induced Photocatalytic Degradation of Pharmaceutical Pollutants. *Environ. Sci. Pollut. Res. Int.* **2023**, *30*, 78537–78553. [CrossRef] [PubMed]

332. Ng, N.; McQueen, T.M. Misfit Layered Compounds: Unique, Tunable Heterostructured Materials with Untapped Properties. *APL Mater.* **2022**, *10*, 100901. [CrossRef]

333. Aliev, S.B.; Tenne, R. Quaternary Misfit Compounds—A Concise Review. *Crystals* **2020**, *10*, 468. [CrossRef]

334. Merrill, D.R.; Moore, D.B.; Bauers, S.R.; Falmbigl, M.; Johnson, D.C. Misfit Layer Compounds and Ferecrystals: Model Systems for Thermoelectric Nanocomposites. *Materials* **2015**, *8*, 2000–2029. [CrossRef]

335. Radovsky, G.; Popovitz-Biro, R.; Stroppa, D.G.; Houben, L.; Tenne, R. Nanotubes from Chalcogenide Misfit Compounds: Sn-S and Nb-Pb-S. *Acc. Chem. Res.* **2014**, *47*, 406–416. [CrossRef] [PubMed]

336. Zullo, L.; Marini, G.; Cren, T.; Calandra, M. Misfit Layer Compounds as Ultratunable Field Effect Transistors: From Charge Transfer Control to Emergent Superconductivity. *Nano Lett.* **2023**, *23*, 6658–6663. [CrossRef] [PubMed]

337. Meerschaut, A. Misfit Layer Compounds. *Curr. Opin. Solid. State Mater. Sci.* **1996**, *1*, 250–259. [CrossRef]

338. Li, Y.; Zhang, J.; Chen, Q.; Xia, X.; Chen, M. Emerging of Heterostructure Materials in Energy Storage: A Review. *Adv. Mater.* **2021**, *33*, 2100855. [CrossRef] [PubMed]

339. Mai, S.S.; Yang, Y.C.; Tuan, H.Y. Exfoliated Misfit Layer Compounds Synergize Conversion-Alloying-Intercalation Triple Mechanism for Enhanced Rate Performance in Potassium Ion Storages. *Chem. Eng. J.* **2024**, *483*, 149289. [CrossRef]

340. Wiegers, G.A. Misfit Layer Compounds: Structures and Physical Properties. *Progress. Solid State Chem.* **1996**, *24*, 1–139. [CrossRef]

341. Rouxel, J.; Meerschaut, A.; Wiegers, G.A. Chalcogenide Misfit Layer Compounds. *J. Alloys Compd.* **1995**, *229*, 144–157. [CrossRef]

342. Kolobov, A.V.; Tominaga, J. *Two-Dimensional Transition-Metal Dichalcogenides*; Springer: Berlin/Heidelberg, Germany, 2016; Volume 1, ISBN 3319314505.

343. Wang, Z.M.; Ren, C.; Tian, H.; Yu, J.; Sun, M. *MoS$_2$*; Springer: Berlin/Heidelberg, Germany, 2013; ISBN 3319028502.

344. Lee, Y.H.; Zhang, X.Q.; Zhang, W.; Chang, M.T.; Lin, C.T.; Di Chang, K.; Yu, Y.C.; Wang, J.T.W.; Chang, C.S.; Li, L.J.; et al. Synthesis of Large-Area MoS$_2$ Atomic Layers with Chemical Vapor Deposition. *Adv. Mater.* **2012**, *24*, 2320–2325. [CrossRef]

345. Van Der Zande, A.M.; Huang, P.Y.; Chenet, D.A.; Berkelbach, T.C.; You, Y.; Lee, G.H.; Heinz, T.F.; Reichman, D.R.; Muller, D.A.; Hone, J.C. Grains and Grain Boundaries in Highly Crystalline Monolayer Molybdenum Disulphide. *Nat. Mater.* **2013**, *12*, 554–561. [CrossRef]

346. Najmaei, S.; Liu, Z.; Zhou, W.; Zou, X.; Shi, G.; Lei, S.; Yakobson, B.I.; Idrobo, J.C.; Ajayan, P.M.; Lou, J. Vapour Phase Growth and Grain Boundary Structure of Molybdenum Disulphide Atomic Layers. *Nat. Mater.* **2013**, *12*, 754–759. [CrossRef]

347. Pospischil, A.; Furchi, M.M.; Mueller, T. Solar-Energy Conversion and Light Emission in an Atomic Monolayer p–n Diode. *Nat. Nanotechnol.* **2014**, *9*, 257–261. [CrossRef] [PubMed]

348. Hui, Y.Y.; Liu, X.; Jie, W.; Chan, N.Y.; Hao, J.; Hsu, Y.T.; Li, L.J.; Guo, W.; Lau, S.P. Exceptional Tunability of Band Energy in a Compressively Strained Trilayer MoS$_2$ Sheet. *ACS Nano* **2013**, *7*, 7126–7131. [CrossRef] [PubMed]

349. Ross, J.S.; Klement, P.; Jones, A.M.; Ghimire, N.J.; Yan, J.; Mandrus, D.G.; Taniguchi, T.; Watanabe, K.; Kitamura, K.; Yao, W.; et al. Electrically Tunable Excitonic Light-Emitting Diodes Based on Monolayer WSe$_2$ p–n Junctions. *Nat. Nanotechnol.* **2014**, *9*, 268–272. [CrossRef] [PubMed]

350. Long, M.; Liu, E.; Wang, P.; Gao, A.; Xia, H.; Luo, W.; Wang, B.; Zeng, J.; Fu, Y.; Xu, K.; et al. Broadband Photovoltaic Detectors Based on an Atomically Thin Heterostructure. *Nano Lett.* **2016**, *16*, 2254–2259. [CrossRef]

351. Roy, T.; Tosun, M.; Kang, J.S.; Sachid, A.B.; Desai, S.B.; Hettick, M.; Hu, C.C.; Javey, A. Field-Effect Transistors Built from All Two-Dimensional Material Components. *ACS Nano* **2014**, *8*, 6259–6264. [CrossRef] [PubMed]

352. Nassiri Nazif, K.; Nitta, F.U.; Daus, A.; Saraswat, K.C.; Pop, E. Efficiency Limit of Transition Metal Dichalcogenide Solar Cells. *Commun. Phys.* **2023**, *6*, 367. [CrossRef]

353. Li, H.; Du, M.; Mleczko, M.J.; Koh, A.L.; Nishi, Y.; Pop, E.; Bard, A.J.; Zheng, X. Kinetic Study of Hydrogen Evolution Reaction over Strained MoS_2 with Sulfur Vacancies Using Scanning Electrochemical Microscopy. *J. Am. Chem. Soc.* **2016**, *138*, 5123–5129. [CrossRef]

354. Zhou, Y.; Ye, Q.; Shi, X.; Zhang, Q.; Xie, Z.; Li, D.; Jiang, D. Regulating Photocatalytic CO_2 Reduction Selectivity via Steering Cascade Multi-Step Charge Transfer Pathways in 1 T/2H-WS_2/TiO_2 Heterojuncitons. *Chem. Eng. J.* **2022**, *447*, 137485. [CrossRef]

355. Qin, J.; Zhao, W.; Hu, X.; Li, J.; Ndokoye, P.; Liu, B. Exploring the N_2 Adsorption and Activation Mechanisms over the 2H/1T Mixed-Phase Ultrathin $Mo_{1-X}W_XS_2$ Nanosheets for Boosting N_2 Photosynthesis. *ACS Appl. Mater. Interfaces* **2021**, *13*, 7127–7134. [CrossRef]

356. Huang, C.; Wu, S.; Sanchez, A.M.; Peters, J.J.P.; Beanland, R.; Ross, J.S.; Rivera, P.; Yao, W.; Cobden, D.H.; Xu, X. Lateral Heterojunctions within Monolayer $MoSe_2$–WSe_2 Semiconductors. *Nat. Mater.* **2014**, *13*, 1096–1101. [CrossRef]

357. Yu, L.; Lee, Y.H.; Ling, X.; Santos, E.J.G.; Shin, Y.C.; Lin, Y.; Dubey, M.; Kaxiras, E.; Kong, J.; Wang, H.; et al. Graphene/MoS_2 Hybrid Technology for Large-Scale Two-Dimensional Electronics. *Nano Lett.* **2014**, *14*, 3055–3063. [CrossRef] [PubMed]

358. Shih, C.J.; Wang, Q.H.; Son, Y.; Jin, Z.; Blankschtein, D.; Strano, M.S. Tuning On-off Current Ratio and Field-Effect Mobility in a MoS_2-Graphene Heterostructure via Schottky Barrier Modulation. *ACS Nano* **2014**, *8*, 5790–5798. [CrossRef] [PubMed]

359. Musso, T.; Kumar, P.V.; Foster, A.S.; Grossman, J.C. Graphene Oxide as a Promising Hole Injection Layer for MoS_2-Based Electronic Devices. *ACS Nano* **2014**, *8*, 11432–11439. [CrossRef] [PubMed]

360. Chuang, S.; Battaglia, C.; Azcatl, A.; McDonnell, S.; Kang, J.S.; Yin, X.; Tosun, M.; Kapadia, R.; Fang, H.; Wallace, R.M.; et al. MoS_2 P-Type Transistors and Diodes Enabled by High Work Function MoO_x Contacts. *Nano Lett.* **2014**, *14*, 1337–1342. [CrossRef] [PubMed]

361. Farmanbar, M.; Brocks, G. Controlling the Schottky Barrier at MoS_2/Metal Contacts by Inserting a BN Monolayer. *Phys. Rev. B Condens. Matter Mater. Phys.* **2015**, *91*, 161304. [CrossRef]

362. Lee, Y.T.; Kang, J.H.; Kwak, K.; Ahn, J.; Choi, H.T.; Ju, B.K.; Shokouh, S.H.; Im, S.; Park, M.C.; Hwang, D.K. High-Performance 2D MoS_2 Phototransistor for Photo Logic Gate and Image Sensor. *ACS Photonics* **2018**, *5*, 4745–4750. [CrossRef]

363. Chaves, A.; Azadani, J.G.; Alsalman, H.; da Costa, D.R.; Frisenda, R.; Chaves, A.J.; Song, S.H.; Kim, Y.D.; He, D.; Zhou, J.; et al. Bandgap Engineering of Two-Dimensional Semiconductor Materials. *NPJ 2D Mater. Appl.* **2020**, *4*, 29. [CrossRef]

364. Omkaram, I.; Hong, Y.K.; Kim, S.; Omkaram, I.; Hong, Y.K.; Kim, S. Transition Metal Dichalcogenide Photodetectors. In *Two-Dimensional Materials for Photodetector*; IntechOpen: London, UK, 2017. [CrossRef]

365. Long, M.; Wang, P.; Fang, H.; Hu, W.; Long, M.; Wang, P.; Fang, H.; Hu, W. Progress, Challenges, and Opportunities for 2D Material Based Photodetectors. *Adv. Funct. Mater.* **2019**, *29*, 1803807. [CrossRef]

366. Wei, X.; Yan, F.-G.; Shen, C.; Lv, Q.-S.; Wang, K.-Y. Photodetectors Based on Junctions of Two-Dimensional Transition Metal Dichalcogenides*. *Chin. Phys. B* **2017**, *26*, 038504. [CrossRef]

367. Pulikodan, V.K.; Raees, A.M.; Alexander, A.; Nalledath, A.K.; Namboothiry, M.A.G. Origin of Anomalous Transient Photocurrent in Solution-Processed WS_2 Nanosheet-Based Self-Powered Photodetectors. *ACS Appl. Nano Mater.* **2024**, *7*, 8007–8021. [CrossRef]

368. Li, G.; Song, Y.; Feng, S.; Feng, L.; Liu, Z.; Leng, B.; Fu, Z.; Li, J.; Jiang, X.; Liu, B.; et al. Improved Optoelectronic Performance of MoS_2 Photodetector via Localized Surface Plasmon Resonance Coupling of Double-Layered Au Nanoparticles with Sandwich Structure. *ACS Appl. Electron. Mater.* **2022**, *4*, 1626–1632. [CrossRef]

369. Kim, S.J.; Kang, M.A.; Jeon, I.S.; Ji, S.; Song, W.; Myung, S.; Lee, S.S.; Lim, J.; An, K.S. Fabrication of High-Performance Flexible Photodetectors Based on Zn-Doped MoS_2/Graphene Hybrid Fibers. *J. Mater. Chem. C Mater.* **2017**, *5*, 12354–12359. [CrossRef]

370. Maity, S.; Sarkar, K.; Kumar, P. Layered Heterostructures Based on MoS_2/$MoSe_2$ Nanosheets Deposited on GaN Substrates for Photodetector Applications. *ACS Appl. Nano Mater.* **2023**, *6*, 4224–4235. [CrossRef]

371. Wu, Q.; Wang, C.; Li, L.; Zhang, X.; Jiang, Y.; Cai, Z.; Lin, L.; Ni, Z.; Gu, X.; Ostrikov, K.; et al. Fast and Broadband MoS_2 Photodetectors by Coupling WO_{3-x} Semi-Metal Nanoparticles Underneath. *J. Mater. Sci. Technol.* **2024**, *193*, 217–225. [CrossRef]

372. Shockley, W.; Queisser, H.J. Detailed Balance Limit of Efficiency of P-n Junction Solar Cells. *J. Appl. Phys.* **1961**, *32*, 510–519. [CrossRef]

373. Nassiri Nazif, K.; Daus, A.; Hong, J.; Lee, N.; Vaziri, S.; Kumar, A.; Nitta, F.; Chen, M.E.; Kananian, S.; Islam, R.; et al. High-Specific-Power Flexible Transition Metal Dichalcogenide Solar Cells. *Nat. Commun.* **2021**, *12*, 7034. [CrossRef]

374. Fontana, M.; Deppe, T.; Boyd, A.K.; Rinzan, M.; Liu, A.Y.; Paranjape, M.; Barbara, P. Electron-Hole Transport and Photovoltaic Effect in Gated MoS_2 Schottky Junctions. *Sci. Rep.* **2013**, *3*, 1634. [CrossRef] [PubMed]

375. Hussain, S.; Patil, S.A.; Memon, A.A.; Vikraman, D.; Naqvi, B.A.; Jeong, S.H.; Kim, H.S.; Kim, H.S.; Jung, J. CuS/WS_2 and CuS/MoS_2 Heterostructures for High Performance Counter Electrodes in Dye-Sensitized Solar Cells. *Sol. Energy* **2018**, *171*, 122–129. [CrossRef]

376. Pinto, F.M.; Dey, S.; Duarte, T.M.; Taft, C.A.; La Porta, F.A. Perovskite-Like Quantum Dots Designed for Advanced Optoelectronic Applications. In *Functional Properties of Advanced Engineering Materials and Biomolecules*; Taft, C.A., de La Porta, F.A., Eds.; Springer: Cham, Switzerland, 2021; pp. 83–108.

377. Green, M.A.; Dunlop, E.D.; Hohl-Ebinger, J.; Yoshita, M.; Kopidakis, N.; Bothe, K.; Hinken, D.; Rauer, M.; Hao, X. Solar Cell Efficiency Tables (Version 60). *Prog. Photovolt. Res. Appl.* **2022**, *30*, 687–701. [CrossRef]

378. Lin, J.; Li, H.; Zhang, H.; Chen, W. Plasmonic Enhancement of Photocurrent in MoS_2 Field-Effect-Transistor. *Appl. Phys. Lett.* **2013**, *102*, 203109. [CrossRef]

379. Eda, G.; Maier, S.A. Two-Dimensional Crystals: Managing Light for Optoelectronics. *ACS Nano* **2013**, *7*, 5660–5665. [CrossRef] [PubMed]

380. Britnell, L.; Ribeiro, R.M.; Eckmann, A.; Jalil, R.; Belle, B.D.; Mishchenko, A.; Kim, Y.J.; Gorbachev, R.V.; Georgiou, T.; Morozov, S.V.; et al. Strong Light-Matter Interactions in Heterostructures of Atomically Thin Films. *Science* **2013**, *340*, 1311–1314. [CrossRef] [PubMed]

381. Li, X.; Lin, M.W.; Puretzky, A.A.; Idrobo, J.C.; Ma, C.; Chi, M.; Yoon, M.; Rouleau, C.M.; Kravchenko, I.I.; Geohegan, D.B.; et al. Controlled Vapor Phase Growth of Single Crystalline, Two-Dimensional GaSe Crystals with High Photoresponse. *Sci. Rep.* **2014**, *4*, 5497. [CrossRef]

382. Fang, H.; Chuang, S.; Chang, T.C.; Takei, K.; Takahashi, T.; Javey, A. High-Performance Single Layered WSe_2 p-FETs with Chemically Doped Contacts. *Nano Lett.* **2012**, *12*, 3788–3792. [CrossRef]

383. Zhou, H.; Wang, C.; Shaw, J.C.; Cheng, R.; Chen, Y.; Huang, X.; Liu, Y.; Weiss, N.O.; Lin, Z.; Huang, Y.; et al. Large Area Growth and Electrical Properties of P-Type WSe_2 Atomic Layers. *Nano Lett.* **2015**, *15*, 709–713. [CrossRef] [PubMed]

384. Ngo, G.Q.; Bucher, T.; Staude, I.; Vogl, T.; Eilenberger, F.; Hübner, U.; George, A.; Turchanin, A.; Najafidehaghani, E.; Gan, Z.; et al. 1D p–n Junction Electronic and Optoelectronic Devices from Transition Metal Dichalcogenide Lateral Heterostructures Grown by One-Pot Chemical Vapor Deposition Synthesis. *Adv. Funct. Mater.* **2021**, *31*, 2101086. [CrossRef]

385. Pitthan, E.; Gerling, E.R.F.; Feijó, T.O.; Radtke, C.; Soares, G.V. Annealing Response of Monolayer MoS_2 Grown by Chemical Vapor Deposition. *ECS J. Solid State Sci. Technol.* **2019**, *8*, P267–P270. [CrossRef]

386. Xing, S.; Zhao, G.; Wang, J.; Xu, Y.; Ma, Z.; Li, X.; Yang, W.; Liu, G.; Yang, J. Band Alignment of Two-Dimensional h-BN/MoS_2 van Der Waals Heterojunction Measured by X-Ray Photoelectron Spectroscopy. *J. Alloys Compd.* **2020**, *834*, 155108. [CrossRef]

387. Liu, Z.; Gong, Y.; Zhou, W.; Ma, L.; Yu, J.; Idrobo, J.C.; Jung, J.; Macdonald, A.H.; Vajtai, R.; Lou, J.; et al. Ultrathin High-Temperature Oxidation-Resistant Coatings of Hexagonal Boron Nitride. *Nat. Commun.* **2013**, *4*, 2541. [CrossRef]

388. Liu, G.; Rumyantsev, S.L.; Jiang, C.; Shur, M.S.; Balandin, A.A. Selective Gas Sensing with H-BN Capped MoS_2 Heterostructure Thin-Film Transistors. *IEEE Electron Device Lett.* **2015**, *36*, 1202–1204. [CrossRef]

389. Wang, J.; Yao, Q.; Huang, C.-W.; Zou, X.; Liao, L.; Chen, S.; Fan, Z.; Zhang, K.; Wu, W.; Xiao, X.; et al. High Mobility MoS_2 Transistor with Low Schottky Barrier Contact by Using Atomic Thick H-BN as a Tunneling Layer. *Adv. Mater.* **2016**, *28*, 8302–8308. [CrossRef] [PubMed]

390. Barton, A.T.; Yue, R.; Anwar, S.; Zhu, H.; Peng, X.; McDonnell, S.; Lu, N.; Addou, R.; Colombo, L.; Kim, M.J.; et al. Transition Metal Dichalcogenide and Hexagonal Boron Nitride Heterostructures Grown by Molecular Beam Epitaxy. *Microelectron. Eng.* **2015**, *147*, 306–309. [CrossRef]

391. Daus, A.; Vaziri, S.; Chen, V.; Köroğlu, Ç.; Grady, R.W.; Bailey, C.S.; Lee, H.R.; Schauble, K.; Brenner, K.; Pop, E. High-Performance Flexible Nanoscale Transistors Based on Transition Metal Dichalcogenides. *Nat. Electron.* **2021**, *4*, 495–501. [CrossRef]

392. Habisreutinger, S.N.; Schmidt-Mende, L.; Stolarczyk, J.K.; Schmidt-Mende, L.; Stolarczyk, J.K.; Habisreutinger, S.N. Photocatalytic Reduction of CO_2 on TiO_2 and Other Semiconductors. *Angew. Chem. Int. Ed.* **2013**, *52*, 7372–7408. [CrossRef] [PubMed]

393. Swetha, S.; Janani, B.; Khan, S.S. A Critical Review on the Development of Metal-Organic Frameworks for Boosting Photocatalysis in the Fields of Energy and Environment. *J. Clean. Prod.* **2022**, *333*, 130164. [CrossRef]

394. Adabala, S.; Dutta, D.P. A Review on Recent Advances in Metal Chalcogenide-Based Photocatalysts for CO_2 Reduction. *J. Environ. Chem. Eng.* **2022**, *10*, 107763. [CrossRef]

395. Singh, S.; Modak, A.; Pant, K.K.; Sinhamahapatra, A.; Biswas, P. MoS_2-Nanosheets-Based Catalysts for Photocatalytic CO_2 Reduction: A Review. *ACS Appl. Nano Mater.* **2021**, *4*, 8644–8667. [CrossRef]

396. Padma, T.; Gara, D.K.; Reddy, A.N.; Vattikuti, S.V.P.; Julien, C.M. $MoSe_2$-WS_2 Nanostructure for an Efficient Hydrogen Generation under White Light LED Irradiation. *Nanomaterials* **2022**, *12*, 1160. [CrossRef]

397. Meier, A.J.; Garg, A.; Sutter, B.; Kuhn, J.N.; Bhethanabotla, V.R. MoS_2 Nanoflowers as a Gateway for Solar-Driven CO_2 Photoreduction. *ACS Sustain. Chem. Eng.* **2019**, *7*, 265–275. [CrossRef]

398. Pratibha; Kapoor, A.; Rajput, J.K. Nanostructured Materials for the Visible-Light Driven Hydrogen Evolution by Water Splitting: A Review. *Int. J. Hydrog. Energy* **2022**, *47*, 17544–17582. [CrossRef]

399. Sarmah, M.K.; Singh, T.P.; Kalita, P.; Dewan, A. Sustainable Hydrogen Generation and Storage—A Review. *RSC Adv.* **2023**, *13*, 25253–25275. [CrossRef]

400. Ganin, A.Y.; Symes, M.D. Towards the Application of 2D Metal Dichalcogenides as Hydrogen Evolution Electrocatalysts in Proton Exchange Membrane Electrolyzers. *Curr. Opin. Electrochem.* **2022**, *34*, 101001. [CrossRef]

401. Rosman, N.N.; Mohamad Yunus, R.; Jeffery Minggu, L.; Arifin, K.; Salehmin, M.N.I.; Mohamed, M.A.; Kassim, M.B. Photocatalytic Properties of Two-Dimensional Graphene and Layered Transition-Metal Dichalcogenides Based Photocatalyst for Photoelectrochemical Hydrogen Generation: An Overview. *Int. J. Hydrog. Energy* **2018**, *43*, 18925–18945. [CrossRef]

402. Tsai, C.; Chan, K.; Nørskov, J.K.; Abild-Pedersen, F. Theoretical Insights into the Hydrogen Evolution Activity of Layered Transition Metal Dichalcogenides. *Surf. Sci.* **2015**, *640*, 133–140. [CrossRef]

403. Sim, Y.; Chae, Y.; Kwon, S.Y. Recent Advances in Metallic Transition Metal Dichalcogenides as Electrocatalysts for Hydrogen Evolution Reaction. *iScience* **2022**, *25*, 105098. [CrossRef]

404. Vikraman, D.; Hussain, S.; Akbar, K.; Truong, L.; Kathalingam, A.; Chun, S.H.; Jung, J.; Park, H.J.; Kim, H.S. Improved Hydrogen Evolution Reaction Performance Using MoS_2-WS_2 Heterostructures by Physicochemical Process. *ACS Sustain. Chem. Eng.* **2018**, *6*, 8400–8409. [CrossRef]

405. Lin, B.; Chen, H.; Zhou, Y.; Luo, X.; Tian, D.; Yan, X.; Duan, R.; Di, J.; Kang, L.; Zhou, A.; et al. 2D/2D Atomic Double-Layer WS_2/Nb_2O_5 Shell/Core Nanosheets with Ultrafast Interfacial Charge Transfer for Boosting Photocatalytic H2 Evolution. *Chin. Chem. Lett.* **2021**, *32*, 3128–3132. [CrossRef]

406. Huang, J.; Mei, J.; Han, J.; Liang, H.; Wang, W.; Dong, B.; Cao, L. Vertical 1T/2H-WS_2 Nanoflakes Grown on 2D-C_3N_4: Multiple Charge Transfer Channels Designed for Enhanced Photocatalytic Activity. *J. Colloid. Interface Sci.* **2019**, *556*, 224–231. [CrossRef]

407. Geng, S.; Tian, F.; Li, M.; Liu, Y.; Sheng, J.; Yang, W.; Yu, Y.; Hou, Y. Activating Interfacial S Sites of MoS_2 Boosts Hydrogen Evolution Electrocatalysis. *Nano Res.* **2022**, *15*, 1809–1816. [CrossRef]

408. Lu, X.W.; Li, Z.; Yang, C.K.; Mou, W.; Jiao, L. Synthesis of Uniform Two-Dimensional MoS_2 Films via Thermal Evaporation. *Nano Res.* **2024**, *17*, 3217–3223. [CrossRef]

409. Pang, Y.; Su, C.; Jia, G.; Xu, L.; Shao, Z. Emerging Two-Dimensional Nanomaterials for Electrochemical Nitrogen Reduction. *Chem. Soc. Rev.* **2021**, *50*, 12744–12787. [CrossRef]

410. Dong, W.; Chen, X.; Peng, J.; Liu, W.; Jin, X.; Ni, G.; Liu, Z. Recent Progress on 2D Transition Metal Compounds-Based Electrocatalysts for Efficient Nitrogen Reduction. *Chem. Res. Chin. Univ.* **2020**, *36*, 648–661. [CrossRef]

411. Xue, Z.; Zhang, X.; Qin, J.; Liu, R. High-Throughput Identification of High Activity and Selectivity Transition Metal Single-Atom Catalysts for Nitrogen Reduction. *Nano Energy* **2021**, *80*, 105527. [CrossRef]

412. Howalt, J.G.; Bligaard, T.; Rossmeisl, J.; Vegge, T. DFT Based Study of Transition Metal Nano-Clusters for Electrochemical NH_3 Production. *Phys. Chem. Chem. Phys.* **2013**, *15*, 7785–7795. [CrossRef]

413. Shi, J.L.; Xiang, S.Q.; Zhang, W.; Zhao, L. Bin A Thermodynamic and Kinetic Study of the Catalytic Performance of Fe, Mo, Rh and Ru for the Electrochemical Nitrogen Reduction Reaction. *Phys. Chem. Chem. Phys.* **2020**, *22*, 25973–25981. [CrossRef]

414. Li, X.; Li, T.; Ma, Y.; Wei, Q.; Qiu, W.; Guo, H.; Shi, X.; Zhang, P.; Asiri, A.M.; Chen, L.; et al. Boosted Electrocatalytic N_2 Reduction to NH_3 by Defect-Rich MoS_2 Nanoflower. *Adv. Energy Mater.* **2018**, *8*, 1801357. [CrossRef]

415. Abghoui, Y.; Sigtryggsson, S.B.; Skúlason, E. Biomimetic Nitrogen Fixation Catalyzed by Transition Metal Sulfide Surfaces in an Electrolytic Cell. *ChemSusChem* **2019**, *12*, 4265–4273. [CrossRef]

416. Matanovic, I.; Leung, K.; Percival, S.J.; Park, J.E.; Lu, P.; Atanassov, P.; Chou, S.S. Towards Defect Engineering in Hexagonal MoS_2 Nanosheets for Tuning Hydrogen Evolution and Nitrogen Reduction Reactions. *Appl. Mater. Today* **2020**, *21*, 100812. [CrossRef]

417. Zhang, L.; Ji, X.; Ren, X.; Ma, Y.; Shi, X.; Tian, Z.; Asiri, A.M.; Chen, L.; Tang, B.; Sun, X.; et al. Electrochemical Ammonia Synthesis via Nitrogen Reduction Reaction on a MoS_2 Catalyst: Theoretical and Experimental Studies. *Adv. Mater.* **2018**, *30*, 1800191. [CrossRef]

418. Ma, C.; Zhai, N.; Liu, B.; Yan, S. Defected MoS_2: An Efficient Electrochemical Nitrogen Reduction Catalyst under Mild Conditions. *Electrochim. Acta* **2021**, *370*, 137695. [CrossRef]

419. Abulizi, A.; Maimaitizi, H.; Talifu, D.; Tursun, Y. In Situ Synthesis of Hierarchical Nitrogen-Doped MoS_2 Microsphere with an Excellent Visible Light-Driven Photocatalytic Nitrogen Fixation Ability. *Funct. Mater. Lett.* **2020**, *13*, 2051031. [CrossRef]

420. Lv, R.; Robinson, J.A.; Schaak, R.E.; Sun, D.; Sun, Y.; Mallouk, T.E.; Terrones, M. Transition Metal Dichalcogenides and Beyond: Synthesis, Properties, and Applications of Single- and Few-Layer Nanosheets. *Acc. Chem. Res.* **2015**, *48*, 56–64. [CrossRef] [PubMed]

421. Chu, K.; Liu, Y.P.; Li, Y.B.; Guo, Y.L.; Tian, Y. Two-Dimensional (2D)/2D Interface Engineering of a MoS_2/C_3N_4 Heterostructure for Promoted Electrocatalytic Nitrogen Fixation. *ACS Appl. Mater. Interfaces* **2020**, *12*, 7081–7090. [CrossRef] [PubMed]

422. Mushtaq, M.A.; Arif, M.; Fang, X.; Yasin, G.; Ye, W.; Basharat, M.; Zhou, B.; Yang, S.; Ji, S.; Yan, D. Photoelectrochemical Reduction of N_2 to NH_3 under Ambient Conditions through Hierarchical $MoSe_2$@g-C_3N_4 Heterojunctions. *J. Mater. Chem. A Mater.* **2021**, *9*, 2742–2753. [CrossRef]

423. Swain, G.; Sultana, S.; Parida, K. Constructing a Novel Surfactant-Free MoS_2 Nanosheet Modified $MgIn_2S_4$ Marigold Microflower: An Efficient Visible-Light Driven 2D-2D p-n Heterojunction Photocatalyst toward HER and PH Regulated NRR. *ACS Sustain. Chem. Eng.* **2020**, *8*, 4848–4862. [CrossRef]

424. Xue, Y.; Ji, Y.; Wang, X.; Wang, H.; Chen, X.; Zhang, X.; Tian, J. Heterostructuring Noble-Metal-Free 1T' Phase MoS_2 with g-C3N4 Hollow Nanocages to Improve the Photocatalytic H_2 Evolution Activity. *Green Energy Environ.* **2021**, *8*, 864–873. [CrossRef]

425. Tong, X.; Zhan, X.; Rawach, D.; Chen, Z.; Zhang, G.; Sun, S. Low-Dimensional Catalysts for Oxygen Reduction Reaction. *Prog. Nat. Sci. Mater. Int.* **2020**, *30*, 787–795. [CrossRef]

426. Lee, W.; Kim, J.; Kim, H.; Back, S. Catalytic Activity Trends of Pyrite Transition Metal Dichalcogenides for Oxygen Reduction and Evolution. *Phys. Chem. Chem. Phys.* **2022**, *24*, 19911–19918. [CrossRef] [PubMed]

427. Liu, C.; Dong, H.; Ji, Y.; Hou, T.; Li, Y. Origin of the Catalytic Activity of Phosphorus Doped MoS_2 for Oxygen Reduction Reaction (ORR) in Alkaline Solution: A Theoretical Study. *Sci. Rep.* **2018**, *8*, 13292. [CrossRef]

428. Zhao, S.; Wang, K.; Zou, X.; Gan, L.; Du, H.; Xu, C.; Kang, F.; Duan, W.; Li, J. Group VB Transition Metal Dichalcogenides for Oxygen Reduction Reaction and Strain-Enhanced Activity Governed by p-Orbital Electrons of Chalcogen. *Nano Res.* **2019**, *12*, 925–930. [CrossRef]

429. Kim, D.Y.; Ha, M.; Kim, K.S. A Universal Screening Strategy for the Accelerated Design of Superior Oxygen Evolution/Reduction Electrocatalysts. *J. Mater. Chem. A Mater.* **2021**, *9*, 3511–3519. [CrossRef]

430. Singh, H.; Liyanage, W.P.R.; Nath, M. Carbon Nanotube Encapsulated Metal Selenide Nanostructures for Efficient Electrocatalytic Oxygen Evolution Reaction. *Chem. Commun.* **2022**, *58*, 8360–8363. [CrossRef] [PubMed]

431. Ge, L.; Yuan, H.; Min, Y.; Li, L.; Chen, S.; Xu, L.; Goddard, W.A. Predicted Optimal Bifunctional Electrocatalysts for the Hydrogen Evolution Reaction and the Oxygen Evolution Reaction Using Chalcogenide Heterostructures Based on Machine Learning Analysis of in Silico Quantum Mechanics Based High Throughput Screening. *J. Phys. Chem. Lett.* **2020**, *11*, 869–876. [CrossRef] [PubMed]

432. Dong Zhu, D.; Long Liu, J.; Zhang Qiao, S.; Zhu, D.D.; Liu, J.L.; Qiao, S.Z. Recent Advances in Inorganic Heterogeneous Electrocatalysts for Reduction of Carbon Dioxide. *Adv. Mater.* **2016**, *28*, 3423–3452. [CrossRef] [PubMed]

433. Abbasi, P.; Asadi, M.; Liu, C.; Sharifi-Asl, S.; Sayahpour, B.; Behranginia, A.; Zapol, P.; Shahbazian-Yassar, R.; Curtiss, L.A.; Salehi-Khojin, A. Tailoring the Edge Structure of Molybdenum Disulfide toward Electrocatalytic Reduction of Carbon Dioxide. *ACS Nano* **2017**, *11*, 453–460. [CrossRef]

434. Dharman, R.K.; Im, H.; Kabiraz, M.K.; Kim, J.; Shejale, K.P.; Choi, S.I.; Han, J.W.; Kim, S.Y. Stable 1T-MoS$_2$ by Facile Phase Transition Synthesis for Efficient Electrocatalytic Oxygen Evolution Reaction. *Small Methods* **2024**, 2301251. [CrossRef] [PubMed]

435. Jehng, J.M.; Turek, A.M.; Wachs, I.E. Surface Modified Niobium Oxide Catalyst: Synthesis, Characterization, and Catalysis. *Appl. Catal. A Gen.* **1992**, *83*, 179–200. [CrossRef]

436. Huang, B.X.; Wang, K.; Church, J.S.; Li, Y.S. Characterization of Oxides on Niobium by Raman and Infrared Spectroscopy. *Electrochim. Acta* **1999**, *44*, 2571–2577. [CrossRef]

437. Özer, N.; Barreto, T.; Büyüklimanli, T.; Lampert, C.M. Characterization of Sol-Gel Deposited Niobium Pentoxide Films for Electrochromic Devices. *Sol. Energy Mater. Sol. Cells* **1995**, *36*, 433–443. [CrossRef]

438. Chiang, C.-L.; Lin, Y.-G. Development of Green Energy Materials: Role of Synchrotron X-ray Spectroscopy. *Vid. Proc. Adv. Mater* **2022**, *3*, 2208307. [CrossRef]

439. Li, W.; Yang, Y.; Li, H.; Zhang, X.; Wang, Y.W.; Tian, W. TEM Characterization and Reaction Mechanism of Composite Coating Fabricated by Plasma Spraying Nb–SiC Composite Powder. *Ceram. Int.* **2023**, *49*, 15055–15064. [CrossRef]

440. Gaddam, S.; Nartu, M.S.K.K.Y.; Chesetti, A.; Mantri, S.A.; Mishra, R.S.; Dahotre, N.B.; Banerjee, R. Hierarchical Phase Evolution during Direct Laser Deposition of an In-Situ Ni-NbC Composite. *Scr. Mater.* **2023**, *226*, 115225. [CrossRef]

441. De Oliveira, T.F.; de Souza, C.P.; Lopes-Moriyama, A.L.; Pereira da Silva, M.L. In Situ Modification of MCM-41 Using Niobium and Tantalum Mixed Oxide from Columbite Processing for Methylene Blue Adsorption: Characterization, Kinetic, Isotherm, Thermodynamic and Mechanism Study. *Mater. Chem. Phys.* **2023**, *294*, 127011. [CrossRef]

442. Lewandków, R.; Mazur, P.; Grodzicki, M. Niobium Oxides Films on GaN: Photoelectron Spectroscopy Study. *Thin Solid. Films* **2022**, *763*, 139573. [CrossRef]

443. Frater, T.; Maurer, J.A. In-Situ Characterization of Electroreduced Tantalum and Niobium in Deep Eutectic Solvents. *ECS Meet. Abstr.* **2022**, *MA2022-02*, 2070. [CrossRef]

444. Lai, J.; Jiang, C.; Zou, Z. Oxygen-Deficient Nb$_2$O$_{5-x}$ Decorated MCMB Anode with Much Enhanced Rate and Cycle Performances for Li-Ion Batteries. *Appl. Surf. Sci.* **2022**, *604*, 154564. [CrossRef]

445. Ahmad, M.W.; Choudhury, A.; Dey, B.; Anand, S.; Al Saidi, A.K.A.; Lee, G.H.; Yang, D.J. Three-Dimensional Core-Shell Niobium-Metal Organic Framework@carbon Nanofiber Mat as a Binder-Free Positive Electrode for Asymmetric Supercapacitor. *J. Energy Storage* **2022**, *55*, 105484. [CrossRef]

446. Mitterhuber, L.; Veerapandiyan, V.; Deluca, M.; Misture, S.; Schaeperkoetter, J.; Tkadletz, M.; Mitterer, C.; Spitaler, J. Anomalous Thermal Conductivity in Amorphous Niobium Pentoxide Thin Films: A Correlation Study between Structure and Thermal Properties. *Materialia* **2022**, *26*, 101601. [CrossRef]

447. Garbarino, G.; Pampararo, G.; Finocchio, E.; Busca, G.; Gervasini, A.; Campisi, S.; Silvestri, B.; Imparato, C.; Aronne, A. Surface Acid Properties of Nb$_2$O$_5$–P$_2$O$_5$–SiO$_2$ Gel-Derived Catalysts. *Microporous Mesoporous Mater.* **2022**, *343*, 112190. [CrossRef]

448. Szostak, R.; de Souza Gonçalves, A.; de Freitas, J.N.; Marchezi, P.E.; de Araújo, F.L.; Tolentino, H.C.N.; Toney, M.F.; das Chagas Marques, F.; Nogueira, A.F. In Situ and Operando Characterizations of Metal Halide Perovskite and Solar Cells: Insights from Lab-Sized Devices to Upscaling Processes. *Chem. Rev.* **2023**, *123*, 3160–3236. [CrossRef]

449. Nico, C.; Monteiro, T.; Graça, M.P.F. Niobium Oxides and Niobates Physical Properties: Review and Prospects. *Prog. Mater. Sci.* **2016**, *80*, 1–37. [CrossRef]

450. DeArdo, A.J. Niobium in Modern Steels. *Int. Mater. Rev.* **2013**, *48*, 371–402. [CrossRef]

451. Tanabe, K.; Okazaki, S. Various Reactions Catalyzed by Niobium Compounds and Materials. *Appl. Catal. A Gen.* **1995**, *133*, 191–218. [CrossRef]